



The Ohio State University

**A STUDY OF A COLLISION AVOIDANCE SYSTEM
MOUNTED ON A CURVED GROUND PLANE**

**Philip H. Law
W. D. Burnside
R. G. Rojas**

**The Ohio State University
ElectroScience Laboratory**

**Department of Electrical Engineering
Columbus, Ohio 43212**

**Semi-Annual Report 716199-8
Contract NSG 1498
March 1986**

**National Aeronautics and Space Administration
Langley Research Center
Hampton, VA 23665**

1077

N/86-24677

NOTICES

When Government drawings, specifications, or other data are used for any purpose other than in connection with a definitely related Government procurement operation, the United States Government thereby incurs no responsibility nor any obligation whatsoever, and the fact that the Government may have formulated, furnished, or in any way supplied the said drawings, specifications, or other data, is not to be regarded by implication or otherwise as in any manner licensing the holder or any other person or corporation, or conveying any rights or permission to manufacture, use, or sell any patented invention that may in any way be related thereto.

REPORT DOCUMENTATION PAGE		1. REPORT NO. 716199-8	2.	3. Recipient's Accession No
4. Title and Subtitle A Study of a Collision Avoidance System Mounted on a Curved Ground Plane			5. Report Date March 1986	
7. Author(s) Philip Law, W.D. Burnside, R. Rojas			8. Performing Organization Rept No 716199-8	
9. Performing Organization Name and Address The ElectroScience Laboratory The Ohio State University 1320 Kinnear Road Columbus, Ohio 43212			10. Project/Task/Work Unit No	
			11. Contract(C) or Grant(G) No (C) NSG 1498 (G)	
12. Sponsoring Organization Name and Address National Aeronautics and Space Administration Langley Research Center Hampton, VA 23665			13. Type of Report & Period Covered Semi-Annual	
15. Supplementary Notes			14	
16. Abstract (Limit 200 words) The research reported in this report involves the evaluation of a traffic advisory and collision avoidance system (TCAS II) mounted on a curved ground plane. It is found that a curved finite ground plane can be used as a good simulation model for the fuselage of an aircraft but may not be good enough to model a whole aircraft due to the shadowing of the vertical stabilizer, wings, and etc. The surface curvature of this curved disc significantly affects the monopulse characteristics in the azimuth plane but not as much in the elevation plane. These variations of the monopulse characteristics verify the need of a lookup table for the 64 azimuth beam positions. The best location of a TCAS II array on a Boeing 737 is to move it as far from the vertical stabilizer as possible.				
17. Document Analysis a. Descriptors b. Identifiers/Open-Ended Terms c. COSATI Field/Group				
18. Availability Statement APPROVED FOR PUBLIC RELEASE: DISTRIBUTION IS UNLIMITED.		19. Security Class (This Report) UNCLASSIFIED		21. No of Pages 112
		20. Security Class (This Page) unclassified		22. Price

TABLE OF CONTENTS

LIST OF TABLES	iv
LIST OF FIGURES	v
CHAPTER	
I INTRODUCTION	1
II TCAS II CIRCULAR ARRAY ANALYSIS	2
A. INTRODUCTION	2
B. PRINCIPLES OF A CIRCULAR ARRAY	2
C. THE MODE BIAS CALCULATION	7
D. COMPUTATION OF THE TSCHEBYSCHIEFF WEIGHTS	13
E. SUM AND DIFFERENCE PATTERNS	15
F. SIMULATED RESULTS	16
III MONOPOLE RADIATION FROM A CURVED AND FLAT GROUND PLANE	23
A. INTRODUCTION	23
B. SHADOW REGION	24
C. LIT REGION	27
D. PATTERN FACTOR	30
E. SOLUTIONS OF A CURVED GROUND PLANE	31
F. EDGE DIFFRACTION FROM A CURVED GROUND PLANE	34
G. SOLUTIONS OF A FLAT GROUND PLANE	39
IV TCAS II SYSTEM	42
A. INTRODUCTION	42
B. THE TCAS II SYSTEM	42
C. COMPUTER MODEL OF THE TCAS II SYSTEM	45
V ANALYSIS OF TCAS II SYSTEMS ON A CURVED SURFACE	52
A. INTRODUCTION	52
B. PATTERN FROM A CURVED GROUND PLANE	53
C. PATTERNS OF A BOEING 737 MODEL	55
D. LIMITATIONS OF THE SIMULATION	56
VI CONCLUSIONS	101
LIST OF REFERENCES	103

LIST OF TABLES

Table 2.1	Table for Generating Sum and Difference Modes	18
Table 3.1	Parameters for Shadow Region	25
Table 3.2	Parameters for Lit Region	29
Table 4.1	Mode Inputs and Element Excitations for Σ and Δ Beams at Zero Degree Azimuth	46
Table 5.1	Input Data for TCAS II Aircraft Code: Ellipsoid Version	58
Table 5.2	Input Data for a Long Ellipsoid	67

LIST OF FIGURES

Figure 2.1.	A thin current ring perpendicular to the x-y plane.	3
Figure 2.2.	A N-element array.	5
Figure 2.3.	An element pattern from a circular array.	10
Figure 2.4.	The shape of an element pattern.	11
Figure 2.5.	Comparison of 2 monopulse waves.	20
Figure 2.6.	Sum and difference beams when side lobe level is 30 and 50 dB.	21
Figure 2.7.	Sum and difference beams with a rotation of 45° to the right.	22
Figure 3.1.	Perspective view of a surface diffracted ray tube.	25
Figure 3.2.	Ray path in the shadow region.	26
Figure 3.3.	Ray path in the lit region.	28
Figure 3.4.	The curved ground plane is part of the surface of a circular cylinder.	32
Figure 3.5.	Ray geometry in lit region.	32
Figure 3.6.	Ray geometry in shadow region.	34
Figure 3.7.	A cone of diffracted rays from a curved ground plane.	35
Figure 3.8.	Transition function.	40
Figure 3.9.	Geometry of a monopole radiating from a flat ground plane.	40

Figure 4.1.	A TCAS system displays a commercial plane (center) and two encroaching planes. The transponder on one of the latter planes has an altitude-reporting feature (-12 indicates it is 1200 feet below the TCAS plane); the second plane's transponder lacks this feature, as indicated by the question marks [1].	43
Figure 4.2.	Beam forming network which uses a Butler matrix to determine the element excitations.	42
Figure 4.3.	Sum and difference beams pointed in the nose direction. The aircraft is modeled by a fuselage only.	48
Figure 4.4.	Ideal TCAS II monopulse curve and its expanded version.	49
Figure 4.5.	Geometry of the computer model that was used to simulate the circular array.	50
Figure 5.1.	TCAS II mounted on a curved and a flat ground plane.	59
Figure 5.2.	Boeing 737 aircraft.	60
Figure 5.3.	Computer-simulated model of the Boeing 737.	61
Figure 5.4.	Coordinate system for azimuth conical pattern cuts.	62
Figure 5.5.	Comparison of an element pattern and a monopulse curve between a curved and a flat ground plane.	63
Figure 5.6.	Comparison of an element pattern and a monopulse curve between a curved and a flat ground plane.	64
Figure 5.7.	The sum and difference patterns corresponding to Figure 5.6.	65
Figure 5.8.	The sum and difference patterns corresponding to Figure 5.6.	65
Figure 5.9.	Same monopulse curves when beam positions are 0° , 90° , 180° , and 270° for a flat ground plane.	66

Figure 5.10.	The simulated structure of a long ellipsoid. The source field of this structure should be close to the source field of a curved disc with a curvature of 72".	66
Figure 5.11.	Comparison of sum and difference patterns.	68
Figure 5.12.	Comparison of monopulse curves referring to the three different cases in the last figure.	69
Figure 5.13.	Element patterns of a curved disc and the fuselage of a Boeing 737.	70
Figure 5.14.	Sum and difference patterns of a curved disc and the fuselage of a Boeing 737 when beam position is 0°.	71
Figure 5.15.	The monopulse curve corresponding to Figure 5.14.	72
Figure 5.16.	Sum and difference patterns of a curved disc and the fuselage of a Boeing 737 when beam position is 45°.	73
Figure 5.17.	The monopulse curve corresponding to Figure 5.16.	74
Figure 5.18.	Sum and difference patterns of a curved disc and the fuselage of a Boeing 737 when beam position is 90°.	75
Figure 5.19.	The monopulse curve corresponding to Figure 5.18.	76
Figure 5.20.	Sum and difference patterns of a curved disc and the fuselage of a Boeing 737 when beam position is 135°.	77
Figure 5.21.	The monopulse curve corresponding to Figure 5.20.	78
Figure 5.22.	Sum and difference patterns of a curved disc and the fuselage of a Boeing 737 when beam position is 180°.	79
Figure 5.23.	The monopulse curve corresponding to Figure 5.22.	80

Figure 5.24.	Sum patterns of a Boeing 737, a curved ground plane and the fuselage of a Boeing 737.	81
Figure 5.25.	Difference patterns of a Boeing 737, a curved ground plane and the fuselage of a Boeing 737.	82
Figure 5.26.	The corresponding monopulse curves.	83
Figure 5.27.	Sum patterns of a Boeing 737, a curved ground plane and the fuselage of a Boeing 737.	84
Figure 5.28.	Difference patterns of a Boeing 737, a curved ground plane and the fuselage of a Boeing 737.	85
Figure 5.29.	The corresponding monopulse curves.	86
Figure 5.30.	Sum patterns of a Boeing 737, a curved ground plane and the fuselage of a Boeing 737.	87
Figure 5.31.	Difference patterns of a Boeing 737, a curved ground plane and the fuselage of a Boeing 737.	88
Figure 5.32.	The corresponding monopulse curves.	89
Figure 5.33.	Sum patterns of a Boeing 737, a curved ground plane and the fuselage of a Boeing 737.	90
Figure 5.34.	Difference patterns of a Boeing 737, a curved ground plane and the fuselage of a Boeing 737.	91
Figure 5.35.	The corresponding monopulse curves.	92
Figure 5.36.	Sum patterns of a Boeing 737, a curved ground plane and the fuselage of a Boeing 737.	93
Figure 5.37.	Difference patterns of a Boeing 737, a curved ground plane and the fuselage of a Boeing 737.	94
Figure 5.38.	The corresponding monopulse curves.	95

Figure 5.39.	All the monopulse curves of a flat ground plane when elevation angle varies from 20° to 40° and the beam position changes.	96
Figure 5.40.	The monopulse curves of a curved ground plane with a curvature of 6-feet when the beam position is 90° and the elevation angle varies from 20° to 40° .	97
Figure 5.41.	The monopulse curves of a curved ground plane with a curvature of 6-feet when the beam position is 0° and the elevation angle varies from 20° to 40° .	98
Figure 5.42.	The monopulse curves of a curved ground plane with a curvature of 6-feet when the elevation angle varies from 20° to 40° and the beam position changes.	99
Figure 5.43.	The monopulse curves of a curved ground plane with a curvature of 6-feet when the elevation angle is 30° and the beam position changes.	100

CHAPTER I

INTRODUCTION

The TCAS II is a midair threat-alert/collision avoidance system. Once every second, the TCAS II system makes a complete survey of other aircraft within a range of about 15 miles, measuring their altitudes, distance separations, closing rates, and approximate bearings [1].

The azimuth bearing of the nearby aircraft is determined by the sum and difference patterns of the TCAS II mounted on top of the aircraft. Angle calibrations are done by a lookup table in the TCAS II processor. This lookup table was created by measurements taken with the array mounted on a circular curved ground plane. How well this curved ground plane can be used to model the fuselage of an aircraft is crucial to the system performance. This report is meant to answer this question.

As far as the report structure is concerned, it is divided into three sections. The first section is used to analyze a circular array and to study the scattering properties of a curved and flat ground plane. The second section introduces the TCAS II system and the corresponding computer model. The last section compares and examines the monopulse curves of a TCAS II system mounted on a flat ground plane, a curved ground plane and a Boeing 737. Conclusions are made at the end of the report.

CHAPTER II

TCAS II CIRCULAR ARRAY ANALYSIS

A. INTRODUCTION

Due to the symmetry of a circular array, a beam can be scanned through 360° with little change of beamwidth and sidelobe level. The ability of a circular array in generating a directional pattern which remains constant in shape over a broad bandwidth makes the circular array practical for a number of applications. Such applications include Direction Finding and Electronic Support Measurement System which is a more sophisticated tracking system [2] than the TCAS II studied in detail here.

B. PRINCIPLES OF A CIRCULAR ARRAY

The far-field patterns of a $2N$ -element circular array and a $2N$ -element linear array are similar; they both have a $\frac{\sin(N\phi)}{\sin(\phi/2)}$ pattern. This similarity in far-field patterns means that all the pattern synthesis techniques that can be applied to a linear array can also be applied to a circular array. The next few sections will discuss and make use of this concept. Note that this discussion is based on the work of Sinsky, et al. [3] and as such follows his approach to the problem. This information is presented here for the convenience of the reader.

Consider a current ring perpendicular to the X-Y plane as illustrated in Figure 2.1. This current ring can be seen as a circular array made up of an infinite number of infinitesimal elements. The pattern of each of these elements is $F(\theta)$, and the element spatial phase is $\gamma(\alpha)$. The field strength at a point (r, θ, ϕ) in the far-field is proportional to the following integral:

$$E(\phi, \theta) = F(\theta) a \int_0^{2\pi} I(\alpha) e^{j\gamma(\alpha)} d\alpha \quad (2.1)$$

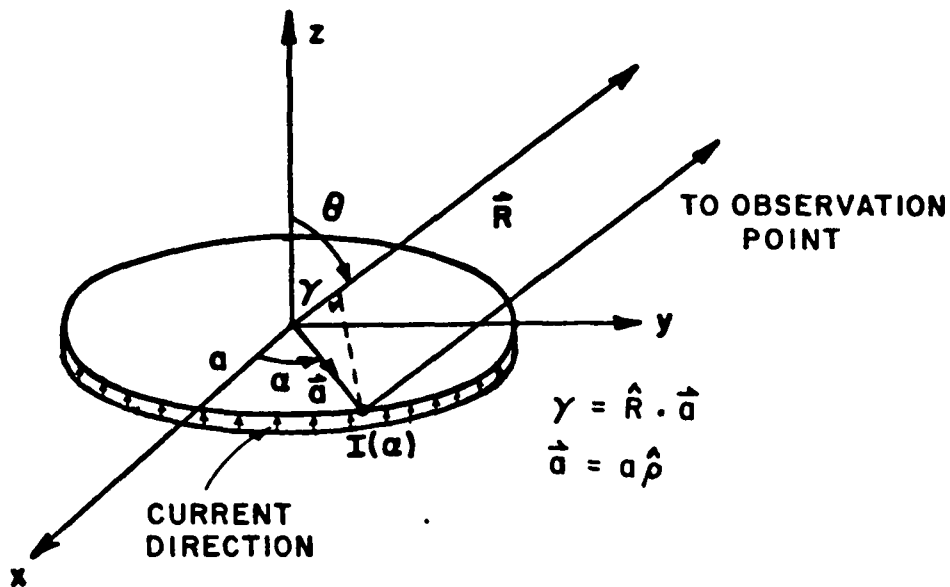


Figure 2.1. A thin current ring perpendicular to the x - y plane.

where

$$\gamma(\alpha) = \hat{k} \hat{p} \hat{a} \cdot \hat{R} = ka(\cos\alpha \hat{x} + \sin\alpha \hat{y}) \cdot \hat{R}$$

$$\text{or } \gamma(\alpha) = \frac{2\pi a}{\lambda} \sin\theta \cos(\alpha - \phi) \quad . \quad (2.2)$$

Because multiplying constants are unimportant, the factors e^{-jkR} and $\frac{1}{R}$ are not included. Also, since the excitation function $I(\alpha)$ for this continuous circular array is a periodic function with a period of 2π radians, $I(\alpha)$ can be expressed by a Fourier Series such that [4]:

$$I(\alpha) = \sum_{m=-N}^N C_m \exp(jm\alpha) \quad ; \quad N \rightarrow \infty \quad . \quad (2.3)$$

Substituting Equation (2.3) into (2.1), one finds that

$$E(\phi, \theta) = F(\theta) a \int_0^{2\pi} \sum_{m=-N}^N C_m e^{j(m\alpha + k a \sin\theta \cos(\alpha - \phi))} d\alpha; \quad N \rightarrow \infty \quad . \quad (2.4)$$

By the following identity [2]:

$$j^m J_m(\beta) = \frac{1}{2\pi} \int_0^{2\pi} e^{j(m\phi + \beta \cos\phi)} d\phi \quad (2.5)$$

one obtains that

$$E(\phi, \theta) = F(\theta) 2\pi a \sum_{m=-N}^N C_m j^m J_m(k a \sin\theta) e^{jm\phi}; \quad N \rightarrow \infty \quad (2.6)$$

Note that J_m is the Bessel function of 1st kind, order m .

When the number of elements in this array is finite, the far-field pattern can still be approximated by Equation (2.6). An N -element array is drawn in Figure 2.2. It is found that the number of elements in the

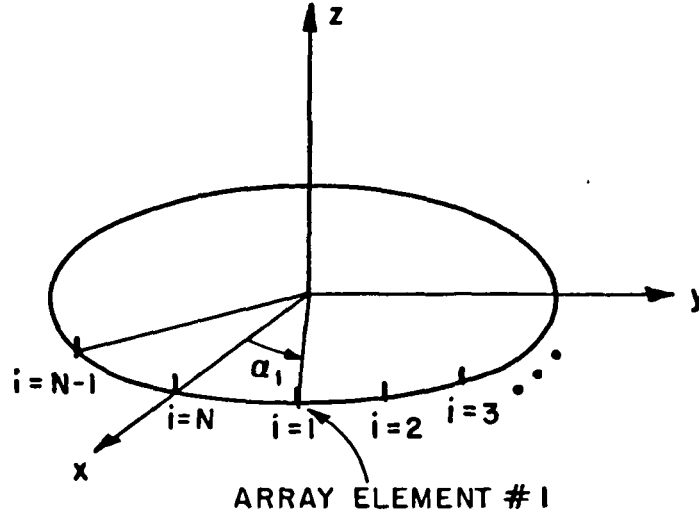


Figure 2.2. A N-element array

array is the same as the number of modes that can be excited [3]. For example, if there are eight elements in the array, the number of modes will also be eight. In other words, if $N=8$, the mode number m will be equal to $-3, -2, -1, 0, 1, 2, 3, 4$, with a total of eight modes. As a result, if N is even, Equation (2.3), evaluated at α_i , can be written as

$$I(\alpha_i) = \sum_{m=-N/2+1}^{N/2} C_m \exp(j \frac{2\pi}{N} i m) \quad (2.7)$$

where $\alpha_i = \frac{2\pi i}{N}$ as in Equation (2.3). The excitation of the i^{th} element can then be written as follows:

$$I_i = \sum_{\ell=-N/2+1}^{N/2} A_{\ell} \exp [j(P_{\ell} + 2\pi i \ell / N)] \quad (2.8)$$

where A_{ℓ} = amplitude of the ℓ^{th} mode input

P_{ℓ} = phase of the ℓ^{th} mode input, and

$A_m \exp(jP_m) = C_m$ in Equation (2.7).

Based on Equation (2.8), it can be seen that the element excitations are determined by the mode inputs. In order to determine the correct mode inputs required to produce a desired antenna pattern, it is first necessary to remove the mode biases [3]. A mode bias is defined as the complex radiation intensity (relative to the array center) resulting from the excitation of the ℓ^{th} mode input. Consider the approximate far-field pattern given by Equation (2.6) such that

$$E(\phi, \theta) = F(\theta) 2\pi a \sum_{m=-N}^N C_m j^m J_m(k a \sin \theta) e^{jm\phi} \quad ; N \text{ is finite} .$$

If $C_m = (2\pi a F(\theta_0) j^m J_m(k a \sin \theta_0))^{-1}$ for a particular θ_0 , then

$$E(\phi) = \sum_{m=-N}^N e^{jm\phi} = \frac{\sin \left(\frac{2N+1}{2} \phi \right)}{\sin \frac{\phi}{2}} \quad (2.9)$$

where

$(C_m)^{-1}$ is the mode bias, and C_m is the mode excitation.

This is nearly identical to the formulation for linear arrays. The radiation pattern of a linear array of $2N+1$ isotropic elements is given by

$$E(u) = \sum_{m=-N}^N A_m e^{jmu} = \frac{\sin(\frac{2N+1}{2}u)}{\sin \frac{u}{2}} \quad (2.10)$$

where

$$u = (2\pi a/\lambda)\sin\phi ,$$

ϕ is the angle off broadside and a is the element spacing of the linear array. Comparing the above two radiation patterns, it can be seen that the mode compensated circular array will produce the same antenna pattern in angle space as that of a linear array in sine angle space. Consequently, the use of the Fourier technique for exciting circular arrays means that all the pattern synthesis techniques for linear arrays may be transferred to circular arrays. In particular, the Tschebyscheff linear array weighting function can be applied to calculate the mode excitations.

In conclusion, once the mode biases are known, the element excitations can be computed by Equation (2.8). Furthermore, for an array with element patterns independent of the angle ϕ , the mode biases are determined by the elevation angle θ_0 of the field point.

C. THE MODE BIAS CALCULATION

To compute the mode biases, one needs to know the element pattern and the far-field pattern of a N -element array. In general, our aircraft code can be used to find the element and far-field patterns of an N -element array. However, for simplicity, the example in Sinsky's paper [3] is followed as an illustration of the mode bias calculation.

Assume the i^{th} element pattern of a circular array is hypothesized by a cosine on a pedestal about an axis which is rotated by β_s from the azimuth angle of the i^{th} element ϕ_i and tipped up from the X-Y plane by α_s [3]. The diagram of this is shown in Figure 2.3. Furthermore, as illustrated in Figure 2.4, the element pattern has a shape given by

$$F_i(\theta, \phi) = 1 + KX_i \quad (2.11)$$

where X_i is the cosine of the angle between the boresight of the i^{th} element (\vec{B}_i) and the direction (\vec{P}). Note that

$$K = (10^{FB/20} - 1) / (10^{FB/20} + 1)$$

with FB defined as the front-to-back ratio. The mathematical expression for X_i is given by a simple expression, namely;

$$\begin{aligned} X_i &= \vec{B}_i \cdot \vec{P} \\ &= \sin\theta \cos\alpha_s [\cos(\phi - \phi_i - \beta_s)] + \cos\theta \sin\alpha_s \end{aligned} \quad (2.12)$$

If each element pattern has the shape such that

$$\alpha_s = 0, \beta_s = 0$$

then

$$X_i = \sin\theta [\cos(\phi - \phi_i)] \quad . \quad (2.13)$$

The far-field pattern from an N-element array is given by

$$E(\theta, \phi) = \sum_{i=1}^N F_i(\theta, \phi) I_i \exp(j\gamma_i) \quad (2.14)$$

where

$F_i(\theta, \phi)$ is the element pattern of the i^{th} element in the radiation direction (θ, ϕ) ,

γ_i is the spatial phase of the i^{th} element relative to the center of the circular array which is given by

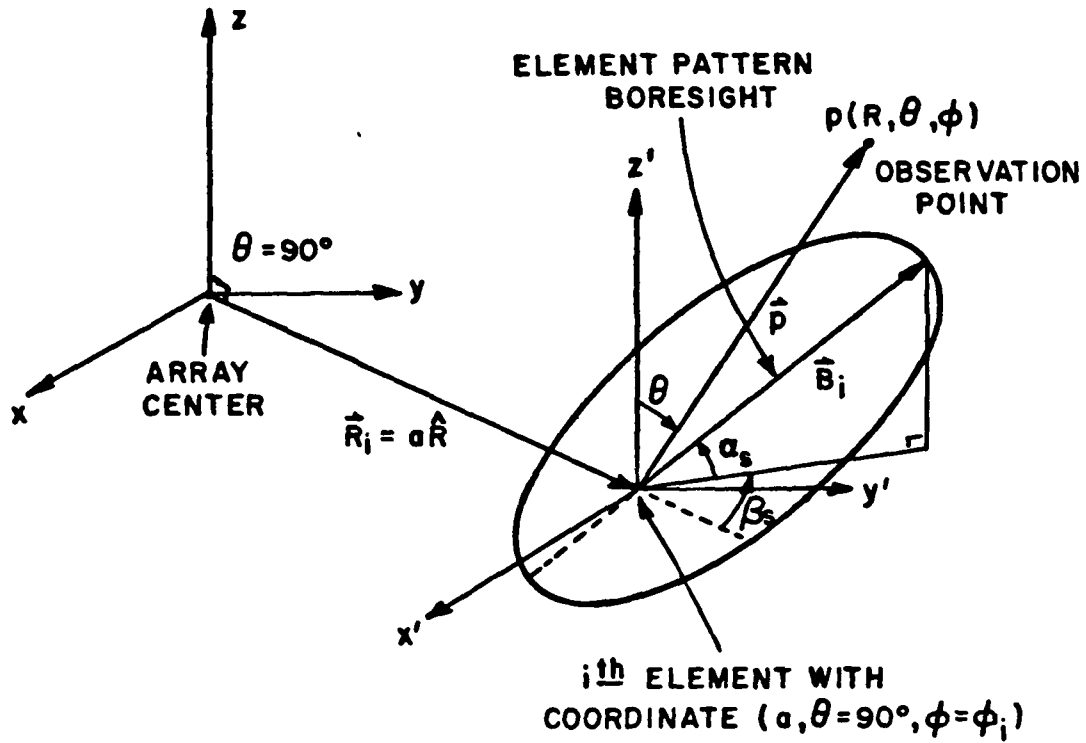
$$\gamma_i = (2\pi a/\lambda) \sin\theta [\cos(\phi - \phi_i)], \text{ and}$$

I_i is the complex element excitation on the i^{th} array element and is defined by Equation (2.8).

After the element pattern and the far-field pattern of an N-element array have been computed, the mode biases can also be found. As indicated before the mode bias is defined as the far-field radiation intensity resulting from excitation of the ℓ^{th} mode input. For convenience, when computing the mode bias, the mode input is defined to have a unit amplitude and zero phase. Combining Equations (2.11), (2.13), and (2.14), the far-field equation for a circular array, when θ is 90° , is given by

$$E(\theta=90^\circ, \phi) = \sum_{i=1}^N \{(1 + K \cos(\phi - \phi_i))\} \exp j(2\pi i \ell / N) \exp[j \frac{2\pi a}{\lambda} \cos(\phi - \phi_i)] \quad (2.15)$$

which is also the mode bias for the ℓ^{th} mode input.



$$\hat{p} = \sin\theta \cos\phi \hat{x} + \sin\theta \sin\phi \hat{y} + \cos\theta \hat{z}$$

$$\hat{B}_i = \cos\alpha_s \cos(\phi_i + \beta_s) \hat{x} + \cos\alpha_s \sin(\phi_i + \beta_s) \hat{y} + \sin\alpha_s \hat{z}$$

Figure 2.3. An element pattern from a circular array.

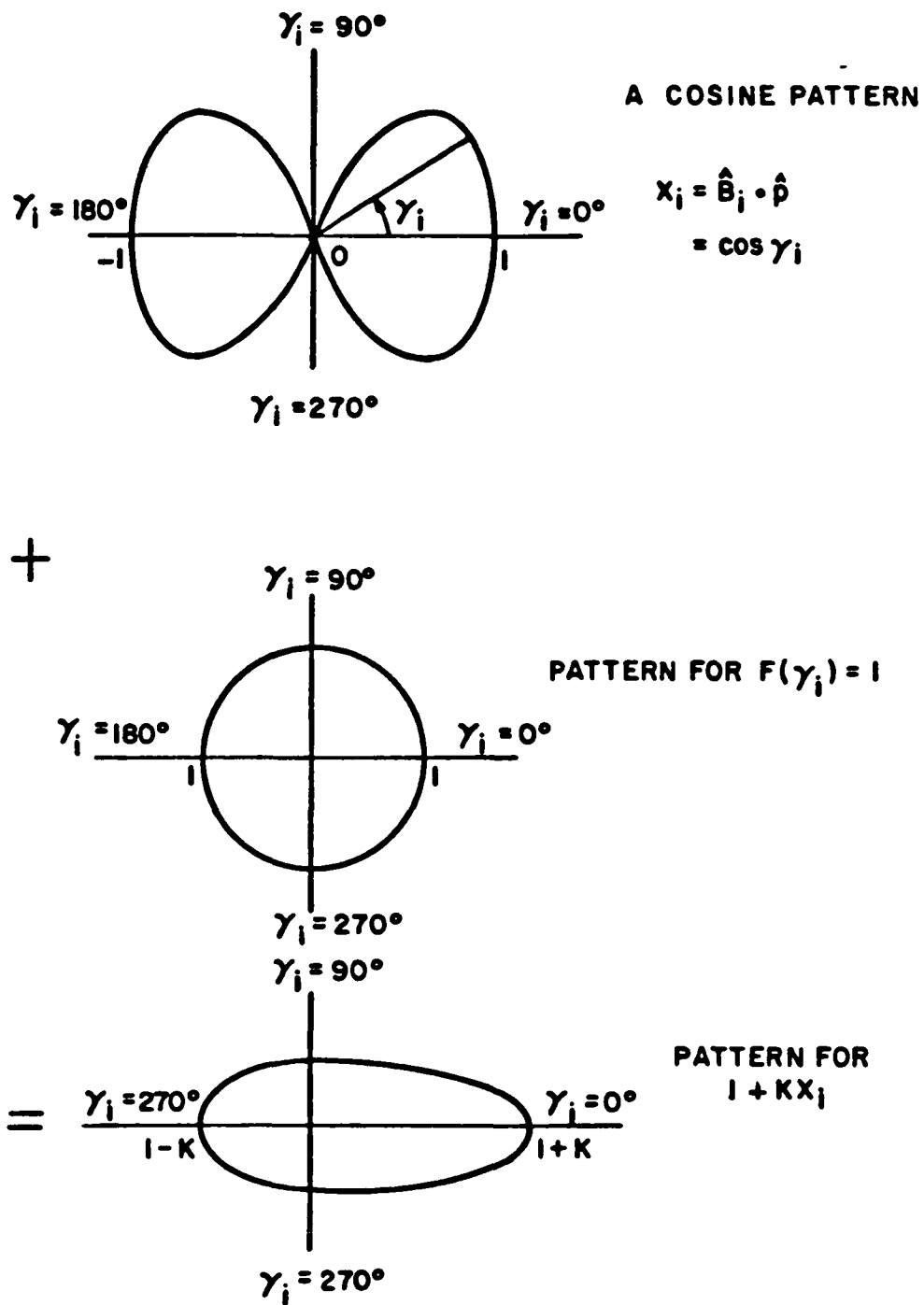


Figure 2.4. The shape of an element pattern.

This far-field pattern may not be realized by any antenna since the element patterns defined in Equation (2.11) are only hypothetical. However, when the angle θ is 90° , this far-field pattern gives a good approximation to the far-field pattern of a TCAS II array as far as the magnitude is concerned. A TCAS II array will be discussed in Chapter IV. Table 2.11(a) shows the mode biases for the array with the hypothetical element patterns, which give an approximation to the true mode biases of a TCAS II array. As has been done in Reference [3], these approximate mode biases will be applied to a TCAS II array so as to illustrate some basic properties of the circular array.

If the mode excitations are set proportional to the reciprocal of these mode biases, then each mode taken one at a time will produce a $e^{jm\phi}$ pattern in the direction (θ_0, ϕ) . The overall pattern can be approximated by

$$E(\phi) = \frac{\sin\left(\frac{2N+1}{2}\phi\right)}{\sin(\phi/2)} \quad \text{for a particular } \theta_0; \quad (2.16)$$

whereas, in our example, θ_0 is chosen to be 90° . If the phase difference between adjacent modes is ϕ_0 radians, the resulting pattern can be expressed as

$$E(\phi) = \frac{\sin\left(\frac{2N+1}{2}(\phi - \phi_0)\right)}{\sin\left(\frac{\phi - \phi_0}{2}\right)} \quad \text{for a particular } \theta_0, \quad (2.17)$$

which is the original pattern rotated by ϕ_0 radians. Note that Equation (2.17) can be obtained from Equation (2.18) or (2.19) by changing the mode excitation C_m in Equation (2.20) or (2.21) to $C_m e^{-jm\phi_0}$.

D. COMPUTATION OF THE TSCHEBYSCHIEFF WEIGHTS

The use of the Fourier technique for exciting a circular array allows the use of all the pattern synthesis techniques for linear arrays. To show this explicitly, let us consider the following approximate far-field pattern of an N-element circular array:

$$E(\phi) = \sum_{m=-N/2+1}^{N/2-1} A_m e^{jm\phi} + A_{N/2} e^{j\frac{N}{2}\phi} \quad \text{when } N \text{ is even} \quad (2.18)$$

or

$$E(\phi) = \sum_{m=-(N-1)/2}^{(N-1)/2} A_m e^{jm\phi} \quad \text{when } N \text{ is odd.} \quad (2.19)$$

The above two equations come from Equation (2.9) with A_m defined as the mode weight, or in this case, the Tschebyscheff weight. When the element number (N) is finite, Equation (2.14) gives a much more accurate representation for the far-field pattern. However, the approximate far-field pattern, expressed by Equations (2.18) and (2.19), is used here to show the relationship between the far-field pattern and the current distribution. The equation for the current distribution is given by

$$I(\alpha_i) = \sum_{m=-N/2+1}^{N/2-1} A_m C_m e^{jm\alpha_i} + A_{N/2} C_{N/2} e^{j\frac{N}{2}\alpha_i} \quad \text{when } N \text{ is even} \quad (2.20)$$

or

$$I(\alpha_i) = \sum_{m=-(N-1)/2}^{(N-1)/2} A_m C_m e^{jm\alpha_i} \quad \text{when } N \text{ is odd} \quad (2.21)$$

where C_m is the mode excitation and A_m is the mode weight.

Both the current distribution and the far-field pattern are a function of the variable (A_m). The manipulation of this variable by pattern synthesis techniques can give the desired far-field pattern. To realize this far-field pattern, the same variable, or the so-called mode weight, needs to be multiplied to the mode excitation to get the correct current excitations. Furthermore, when N is even, to obtain a $\sin N\phi/\sin\phi$ pattern, mode $N/2$ is usually not excited so as to get a symmetry in the modes excited.

If a Tschebyscheff pattern is desired, the mode amplitude distribution must be tapered. Consider the far-field pattern of a circular array given by

$$E(\phi) = \sum_{m=-(N-1)/2}^{(N-1)/2} A_m e^{jm\phi} = A_0 + 2 \sum_{m=1}^{(N-1)/2} A_m \cos(2m\phi/2) \quad (2.22)$$

where $A_m = A_{-m}$ and N is odd. Since the right side of Equation (2.22) can be expressed as a polynomial of order $N-1$ in the variable $\cos(\phi/2)$, it can be matched to the Tschebyscheff polynomial $T_{N-1}(U)$ by letting

$$U = U_0 \cos(\phi/2)$$

in which U_0 is selected so that $T_{N-1}(U_0) = r$, with r being the desired main beam to sidelobe voltage ratio.

Elliot [5] found that the Tschebyscheff coefficients in Equation (2.22) can be approximated by a series such that

$$A_m = a_0 + 2 \sum_{p=1}^{(N-1)/2} a_p \cos(p2\pi m/N) \quad (2.23)$$

where

$$a_p = \frac{1}{N} T_{N-1} \left(U_0 \cos \frac{\pi p}{N} \right)$$

$$a_0 = \frac{1}{N} T_{N-1} (U_0)$$

and T_N is the Tschebyscheff polynomial.

Combining the above two equations, the mode weights can be expressed as

$$A_m = \frac{1}{N} \left\{ T_{N-1} (U_0) + 2 \sum_{p=1}^{(N-1)/2} T_{N-1} \left(U_0 \cos \frac{\pi p}{N} \right) \cos (p2\pi m/N) \right\} \quad (2.24)$$

when N is odd. Similarly, as pointed out in Reference [3], the following equation also holds:

$$A_m = \frac{1}{N} \left\{ T_{N-1} (U_0) + 2 \sum_{p=1}^{N/2-1} T_{N-1} \left(U_0 \cos \frac{\pi p}{N} \right) \cos (p(2m+1)\pi/N) \right\} \quad (2.25)$$

when N is even.

E. SUM AND DIFFERENCE PATTERNS

A circular array of an even number of elements has a radiation pattern given by Equation (2.18). Because of the property of Tschebyscheff weights, the coefficient (A_m) is equal to the coefficient (A_{-m}). Furthermore, since mode $\frac{N}{2}$ is not excited, Equation (2.18) can be rewritten as follows:

$$E(\phi) = A_0 + 2 \sum_{m=1}^{N/2-1} A_m \cos m\phi \quad , \quad (2.26)$$

which gives a sum pattern.

If current is excited such that

$$A_m = -A_{-m}$$

then

$$E(\phi) = A_0 + 2j \sum_{m=1}^{N/2-1} A_m \sin m\phi \quad . \quad (2.27a)$$

To get a difference pattern, A_0 must be set to zero. This implies that

$$E(\phi) = 2j \sum_{m=1}^{N/2-1} A_m \sin m\phi \quad . \quad (2.27b)$$

The monopulse characteristic equation is given as follows [3]:

$$M = 20 \log_{10} \left| \frac{\Sigma + j\Delta}{\Sigma - j\Delta} \right| \quad . \quad (2.28)$$

By the previous two equations; one can find that

$$M = 20 \log_{10} \left| \frac{A_0 + 2 \sum_{m=1}^{N/2-1} A_m (\cos m\phi - \sin m\phi)}{A_0 + 2 \sum_{m=1}^{N/2-1} A_m (\cos m\phi + \sin m\phi)} \right| \quad . \quad (2.29)$$

F. SIMULATED RESULTS

A computer program has been written to find the sum and difference mode excitations. The results are listed in Table (2.1). Substituting these sum and difference mode coefficients into Equation (2.29), a theoretical monopulse curves curve is obtained. This curve compares favorably with the monopulse curve obtained by UTD from finding the far-field pattern of a circular array mounted on a flat ground plane.

These two monopulse curves are shown in Figure 2.5. When the target angle is outside the -25° to 25° range, the two monopulse curves do not agree very well; however, each beam position is only useable by the system for a small angular range which is less than $\pm 25^\circ$.

Figures 2.6(a) and (b) show the sum and difference beams when the side lobe levels are 50 and 30 dB, respectively. Figure 2.7 shows that the sum and difference beams can be rotated without changing the pattern shape.

TABLE 2.1

TABLE FOR GENERATING SUM AND DIFFERENCE MODES

(A) THE MODE BIASES FOR 30 dB SIDE LOBE LEVEL;

i.e. $C_m^{-1} = E(90^\circ, 0^\circ)$ from Equation (2.15)

MODE	VOLTAGE (in volts)	dB	DEGREE
-3	0.7705	-2.2649	-106.3775
-2	1.4050	2.9534	176.7064
-1	1.1957	1.5527	123.7852
0	0.9377	-0.5584	137.7721
1	1.1957	1.5527	123.7848
2	1.4050	2.9534	176.7055
3	0.7705	-2.2650	-106.3784
4	0.8570	-1.3400	- 33.1587

(B) THE MODE WEIGHTS;

i.e. A_m from Equation (2.25)

MODE	dB
0	0.0000
1	-1.1716
2	-4.9089
3	-11.5605

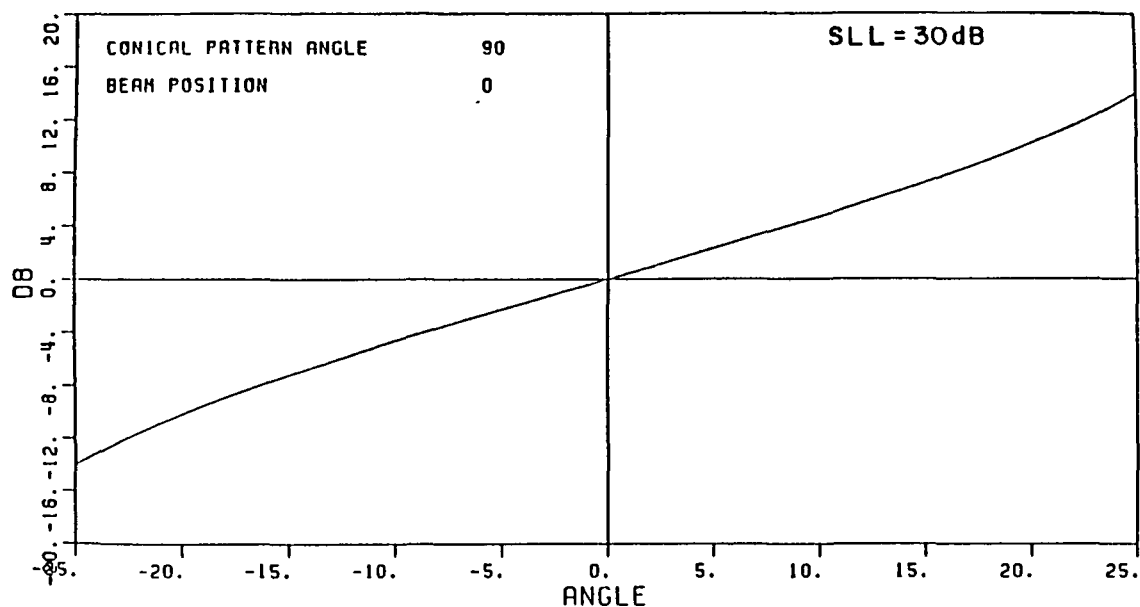
TABLE 2.1 (Continued)

(C) THE SUM MODE EXCITATIONS;
i.e., $A_m C_m$ in Equation (2.20) or (2.21)

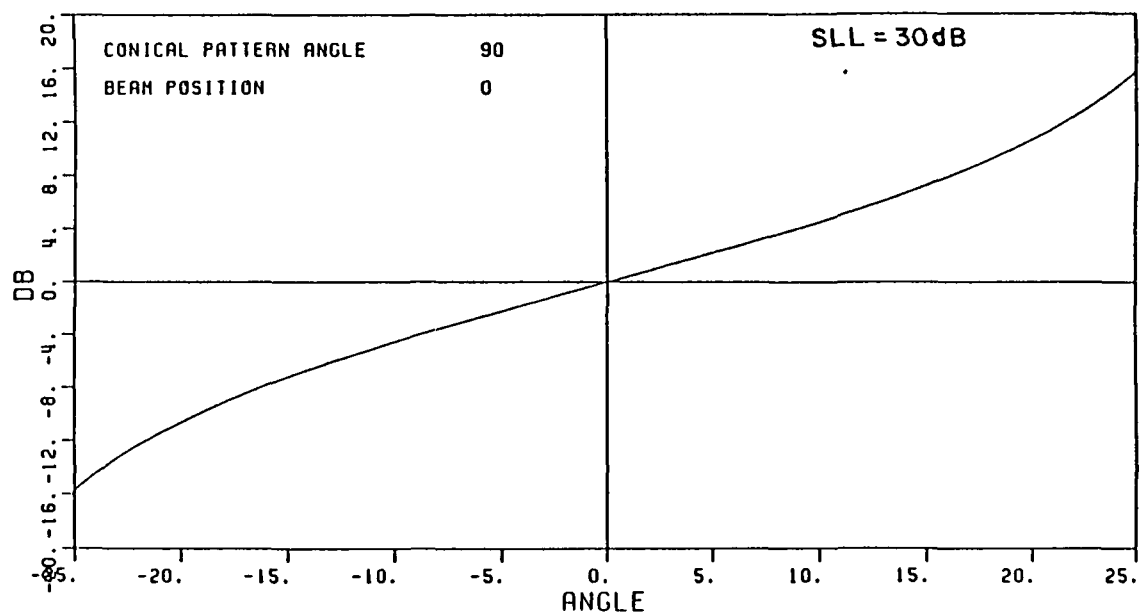
SUM MODE	dB	DEGREE
-3	-9.2956	106.3775
-2	-7.8623	-176.7064
-1	-2.7243	-123.7852
0	0.5584	-137.7721
1	-2.7244	-123.7848
2	-7.8623	-176.7055
3	-9.2955	106.3784
4	-100.0000	33.1587

(D) THE DIFFERENCE MODE EXCITATIONS;
i.e., $A_m C_m$ with A_m defined in Equation (2.27a)

DIFFERENCE MODE	dB	DEGREE
-3	-9.2956	286.3874
-2	-7.8623	3.2945
-1	-2.7243	56.2152
0	-100.0000	-137.7721
1	-2.7244	-123.7848
2	-7.8623	-176.7055
3	-9.2955	106.3784
4	-100.0000	33.1587



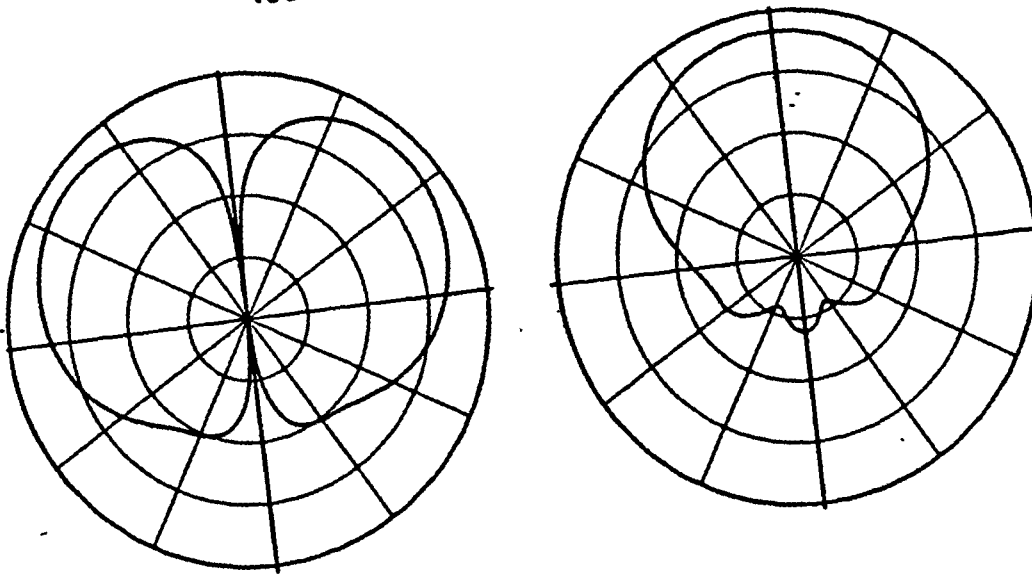
(a) A monopulse curve obtained by UTD from finding the far-field pattern of a circular array mounted on a flat ground plane.



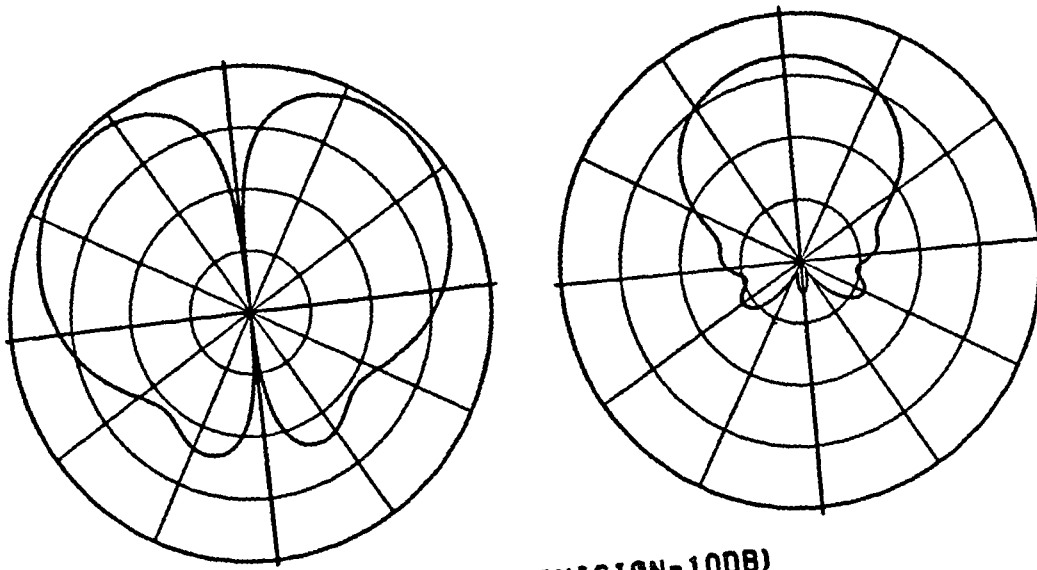
(b) A monopulse curve obtained by Equation (2.29).

Figure 2.5. Comparison of monopulse characteristic results.

(SCALE: EACH DIVISION=10DB)



(a) side lobe level at 50 dB.



(SCALE: EACH DIVISION=10DB)

(b) side lobe level at 30 dB.

Figure 2.6. Sum and difference beams when side lobe level is 30 and 50 dB.

(SCALE: EACH DIVISION=10DB)

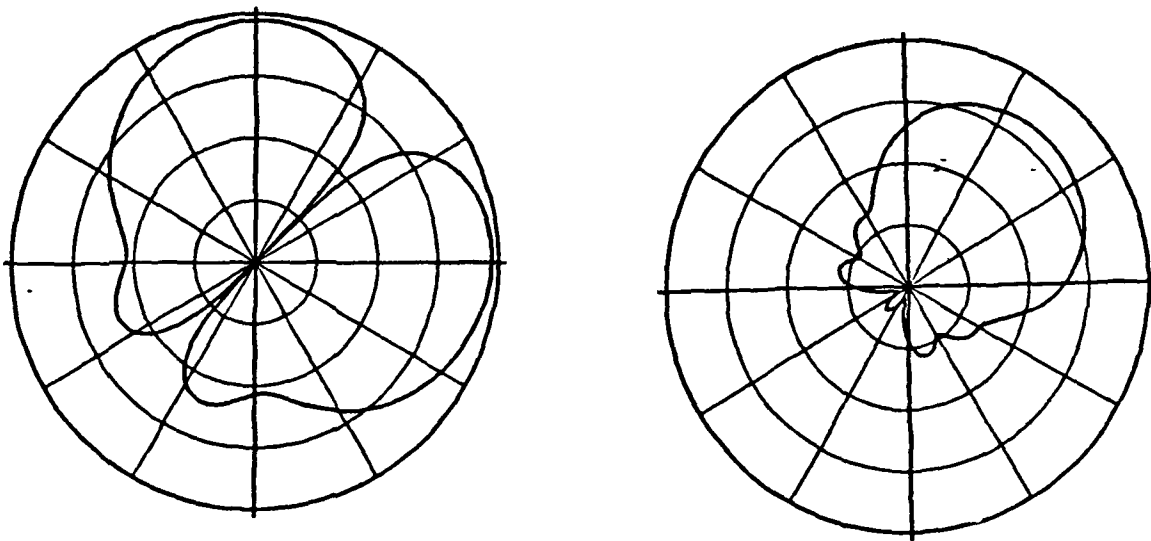


Figure 2.7. Sum and difference beams with a pattern rotation of 45° to the right.

CHAPTER III

MONOPOLE RADIATION FROM A CURVED AND FLAT GROUND PLANE

A. INTRODUCTION

The principal analytical tool used to analyze the radiation of an antenna mounted on a curved or flat ground plane is the Uniform Theory of Diffraction (UTD). Basically, UTD is an extension of Keller's Geometrical Theory of Diffraction (GTD) [6]. However, unlike GTD which fails in the regions adjacent to the incident and reflection shadow boundaries, the UTD solution is valid everywhere. In this chapter, the radiation pattern of a TCAS II system mounted on a curved and flat ground plane will be analyzed using UTD. The patterns will later be compared with those obtained from a TCAS II array mounted on a Boeing 737 aircraft. The corresponding monopulse characteristic curves will also be compared.

As will be shown later, the TCAS II system can be modeled by a circular array of eight pairs of monopoles. According to geometrical optics, each monopole will divide the surrounding space into a lit and a shadow region by a plane tangent to the surface at the source location. Distinct mechanisms are used to calculate the field patterns in these two regions. References [7], [8] and [9] provide a good background for this material.

B. SHADOW REGION

According to the generalized Fermat's principle, a ray emanating from a source, which is located on a curved surface, follows a geodesic path on the surface and continually sheds energy into the shadow region. Such a creeping wave mechanism is illustrated in Figure 3.1. Point Q is the point of diffraction where the ray leaves the surface and propagates toward the observation point. As illustrated in Figure 3.2, \hat{n}' is the unit surface normal vector, \hat{t}' is the unit tangent vector and \hat{b}' is the unit binormal vector given by $\hat{b}' = \hat{t}' \times \hat{n}'$ at the source point Q'. Similar vector convention is used along the geodesic path.

It is found that the field $d\vec{E}_e$ radiated by an infinitesimal electric current moment $d\vec{P}_e$ at point p_s can be expressed as [10]

$$d\vec{E}_e(p_s) = d\vec{P}_e(Q') \cdot [\hat{n}' \hat{n} T_5(Q') H + \hat{n}' \hat{b}' T_6(Q') S] e^{-jkt} e^{-jks} \cdot \left(\frac{-jkZ_0}{4\pi} \right) \sqrt{\frac{\rho_c}{s(\rho_c + s)}} \sqrt{\frac{d\psi_0}{dn(0)}} \left| \frac{\rho_g(Q')}{\rho_g(Q')} \right|^{\frac{1}{6}} \quad (3.1)$$

where T_5 and T_6 are the torsion factors at Q' and are given in Table 3.1. H and S are the uniform Fock functions whose expressions are given below:

$$H = g(\epsilon) \quad (3.2)$$

$$S = \frac{-j}{m(Q')} \tilde{g}(\epsilon) \quad (3.3)$$

with

$$g(\epsilon) = \frac{1}{\sqrt{\pi}} \int_{-\infty \exp(-j2\pi/3)}^{\infty} d\tau \frac{\exp(-j\tau\epsilon)}{w_2'(\tau)} \quad (3.4)$$

and

TABLE 3.1
PARAMETERS FOR SHADOW REGION

TYPE OF CONVEX SURFACE	SLOT OR $d\bar{s}_m$ CASE				MONOPOLE OR $d\bar{s}_0$ CASE		SURFACE RAY TORSION $T_1(Q')$	SURFACE RADIUS OF CURVATURE IN \hat{t} DIRECTION $\rho_0(Q')$	SURFACE DIFFRACTED RAY CAUSTIC DISTANCE ρ_c
	$T_1(Q')$	$T_2(Q')$	$T_3(Q')$	$T_4(Q')$	$T_5(Q')$	$T_6(Q')$			
SPHERE	1	1	0	0	1	0	0	∞	$\infty \tan(\frac{1}{2})$
CIRCULAR CYLINDER	1	1	$\frac{\sin 2\theta'}{2a} \cdot \frac{a}{\sin^2 \theta'}$	0	1	$\frac{\sin 2\theta'}{2a} \cdot \frac{a}{\sin^2 \theta'}$	$\frac{\sin 2\theta'}{2a}$	$\frac{a}{\sin^2 \theta'}$	1
ARBITRARY CONVEX SURFACE	1	1	$T_1(Q') \rho_0(Q')$	0	1	$T_1(Q') \rho_0(Q')$	$\frac{\sin 2\theta'}{2} \left(\frac{1}{\rho_1(Q')} - \frac{1}{\rho_2(Q')} \right)$ WITH $\rho_1(Q') \geq \rho_2(Q')$	$\left(\frac{\cos^2 \theta'}{\rho_1(Q')} \cdot \frac{\sin^2 \theta'}{\rho_2(Q')} \right)^{-1/2}$	$\frac{2\sqrt{E} a}{\partial \theta / \partial t}$

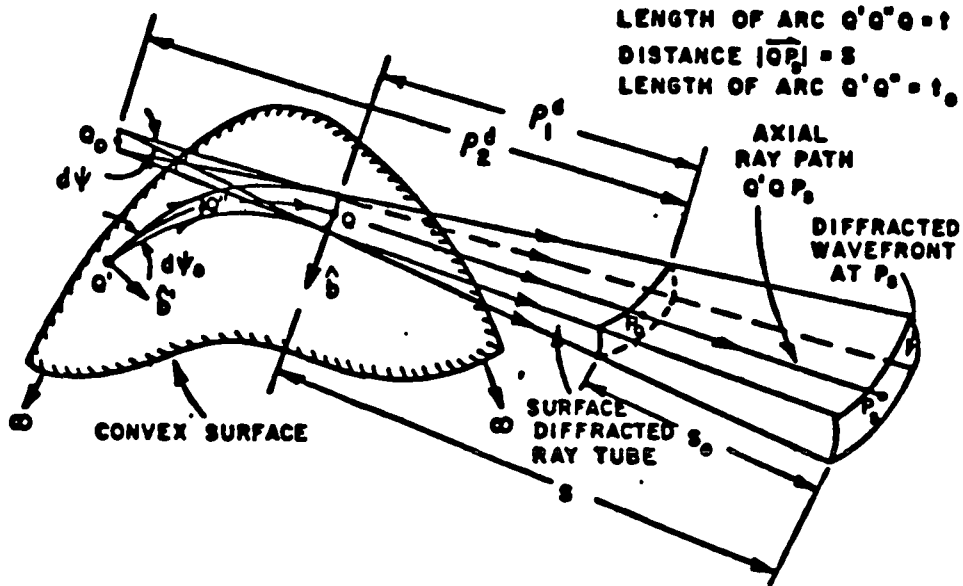


Figure 3.1. Perspective view of a surface diffracted ray tube.

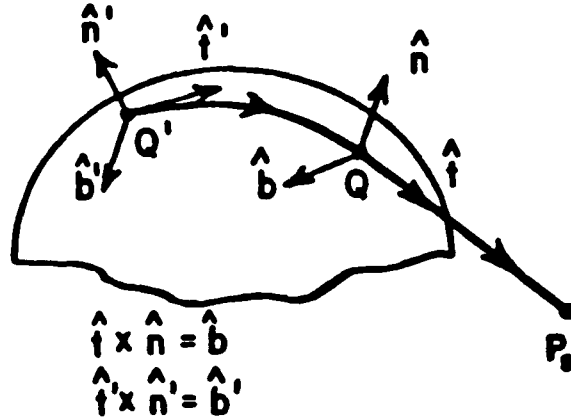


Figure 3.2. Ray path in the shadow region.

$$\tilde{g}(\epsilon) = \frac{1}{\sqrt{\pi}} \int_{-\infty \exp(-j2\pi/3)}^{\infty} d\tau \frac{\exp(-j\tau\epsilon)}{w_2(\tau)} \quad (3.5)$$

which are known as the acoustic hard and soft Fock functions, respectively. The Fock type Airy function is given by

$$w_2(\tau) = \frac{1}{\sqrt{\pi}} \int_{-\infty \exp(j2\pi/3)}^{\infty} dt \cdot \exp(\tau t - t^3/3) \quad (3.6)$$

and $w_2'(\tau)$ is the derivative of $w_2(\tau)$ with respect to τ . The Fock parameter for the shadow region is given by

$$\varepsilon = \int_{Q'}^Q dt' \frac{m(t')}{\rho_g(t')} \quad (3.7)$$

with

$$m(t') = \left[\frac{k \rho_g(t')}{2} \right]^{1/3} \quad (3.8)$$

where $\rho_g(t')$ is the surface radius of curvature along the ray path at t' . The width of the surface ray tube at Q is given by

$$d\eta(Q) = \rho_c d\psi \quad (3.9)$$

where ρ_c is the surface diffracted ray caustic distance; t is the length of the geodesic path.

C. LIT REGION

In the lit region, the radiated energy propagates directly from the source to the observation point along the incident ray of geometrical optics as shown in Figure 3.3. The electric field at P_L in the lit region can be expressed as [10]

$$d\bar{E}_e(P_L) = \frac{-jk}{4\pi} d\bar{P}_e(Q') \cdot \bar{T}_e^L \frac{e^{-jks}}{s} \quad (3.10)$$

where $\frac{e^{-jks}}{s}$ represents the spherical wave factor associated with the point source at Q' and $d\bar{P}_e$ has been defined in section B. The explicit form of the dyadic transfer function is found to be [10]

$$\bar{T}_e^L = Z_0 \sin\theta^i [\hat{n}'\hat{n}_L (H^L + T_0^2 F \cos\theta^i) + \hat{n}'\hat{b} T_0 F] \quad (3.11)$$

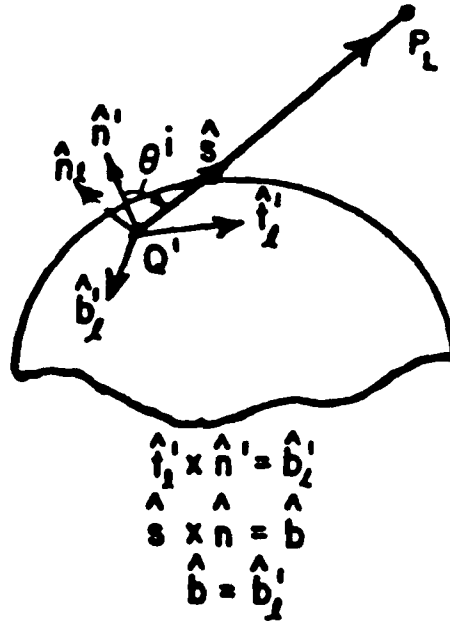


Figure 3.3. Ray path in the lit region.

The Fock functions H^ℓ and S^ℓ for the lit region are defined as follows:

$$H^\ell(\epsilon^\ell) = \frac{e^{-j\epsilon^\ell/3}}{\sqrt{\pi}} \int_{-\infty}^{\infty} \frac{e^{-j\epsilon^\ell \tau}}{e^{-j2\pi/3} W_2'(\tau)} d\tau \quad (3.12)$$

and

$$S^\ell(\epsilon^\ell) = \frac{-j}{m(Q')} \frac{e^{-j\epsilon^\ell/3}}{\sqrt{\pi}} \int_{-\infty}^{\infty} \frac{e^{-j\epsilon^\ell \tau}}{e^{-j2\pi/3} W_2(\tau)} d\tau \quad (3.13)$$

where the functions W_2 and W_2' have been defined previously in Equation (3.6). The Fock parameter ϵ^ℓ for the lit region is given by

$$\epsilon^\ell = -m_\ell(Q') \cos \theta^i = -m(Q') [1 + T_0^2 \cos^2 \theta^i]^{-1/3} \cos \theta^i. \quad (3.14)$$

The angle θ^i is defined by $\hat{s} \cdot \hat{n}^i = \cos \theta^i$ as shown in Figure 3.3. Finally, F is given by

$$F = \frac{S^2 - H^2 \cos^2 \theta^i}{1 + T_0^2 \cos^2 \theta^i} \quad (3.15)$$

as defined in Table 3.2. The other parameters are the same as in the shadow case.

TABLE 3.2
PARAMETERS FOR LIT REGION

SLOT OR $d\vec{p}_0$ CASE				MONOPOLE OR $d\vec{p}_0$ CASE		T_0	T
A	B	C	D	M	N		
$H^2 + T_0^2 T \cos \theta^i$	$S^2 - T_0^2 T \cos^2 \theta^i$	$T_0 T$	$T_0 T \cos \theta^i$	$\sin \theta^i [H^2 + T_0^2 T \cos \theta^i]$	$\sin \theta^i T_0 T$	$T(Q^i) \rho_0(Q^i)$	$\frac{S^2 - H^2 \cos^2 \theta^i}{1 + T_0^2 \cos^2 \theta^i}$

D. PATTERN FACTOR

The general solution for a short monopole mounted on a convex surface has been given in the previous two sections. To get a solution for a linear antenna problem, one needs to integrate the above solution over the source distribution. This gives an accurate solution but is very tedious. A more efficient approach is to modify $d\bar{P}_e(Q')$ as shown in Reference [11] such that

(a) in the lit region

$$\bar{P}_e = \hat{n}' [1 - \cos(KL)] \quad (3.16)$$

(b) in the shadow region

$$\bar{P}_e = \hat{n}' \frac{\cos(KL\hat{n}' \cdot \hat{s}) - \cos(KL)}{1 - (\hat{n}' \cdot \hat{s})^2} \quad (3.17)$$

where L = the length of the monopole. L should not exceed a quarter wavelength for the solution to be valid.

E. SOLUTIONS OF A CURVED GROUND PLANE

The previous three sections gave generalized results to a monopole mounted on a convex surface. As illustrated in Figure 3.4, the curved ground plane being considered here is part of a circular cylinder. Thus, solutions that can be applied to a circular cylinder can also be applied to the curved ground plane. Edge diffraction must be included in the curved ground plane solution which will be discussed in the next section. Combining equations in the previous three sections, Reference [12] gives expressions for near-zone fields due to a monopole radiating from a circular cylinder as follows

(a) Lit Region: (see Figure 3.5)

$$\tilde{E}_{\phi'} = P_{lit} \left\{ -(\hat{e}_1 \cdot \hat{t}) H^{\ell}(\epsilon^{\ell}) \frac{e^{-jks}}{s} \right\} \hat{\phi}' \quad (3.18)$$

$$\tilde{E}_{\theta'} = P_{lit} \left\{ \cos \theta' \cdot \left[m(Q') \left(\frac{2}{k \rho_g(Q') \sin \theta'} \right)^{1/3} \right] \cdot S^{\ell}(\epsilon^{\ell}) \frac{e^{-jks}}{s} \right\} \hat{\theta}' \quad (3.19)$$

with

$$P_{lit} = \frac{-jZ_0}{4\pi} \left[\frac{\cos(kL \hat{n}' \cdot \hat{s}) - \cos(kL)}{[1 - (\hat{n}' \cdot \hat{s})^2] \sin(kL)} \right] \quad (3.20a)$$

and

$$\epsilon^{\ell} = -\left(\frac{k \sin \theta'}{2} \right)^{1/3} (\hat{n}' \cdot \hat{t}) \quad (3.20b)$$

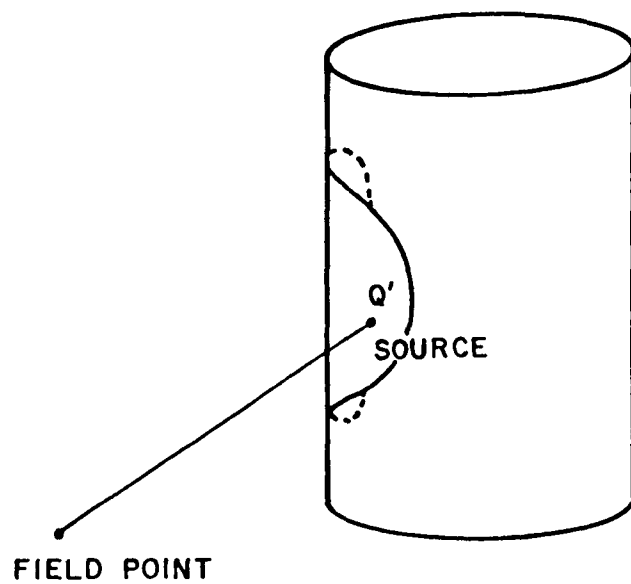


Figure 3.4. The curved ground plane is part of the surface of a circular cylinder.

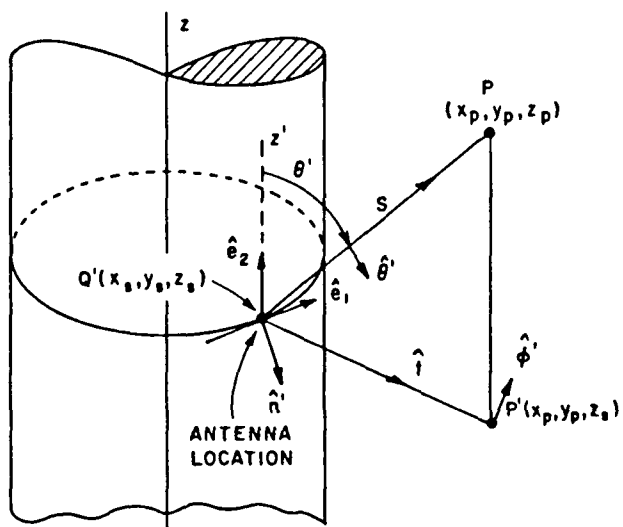


Figure 3.5. Ray geometry in lit region.

(b) Shadow Region: (see Figure 3.6)

$$\bar{E}_n = P_{\text{dark}} \left\{ \sum_{i=1}^2 g(\epsilon_i) \left[\frac{\rho_g(Q_i)}{\rho_g(Q')} \right]^{1/6} \frac{e^{-jk(\ell_i + S_i)}}{\sqrt{S_i(S_i + \ell_i)}} \hat{n}_i \right\} \quad (3.21a)$$

$$\bar{E}_b = P_{\text{dark}} \left\{ \sum_{i=1}^2 (-1)^{i-1} \sin W_i \left[-j \left(\frac{2}{k \rho_g(Q') \cos W_i} \right)^{1/3} \right] \right\} \cdot$$

$$\tilde{g}(\epsilon_i) \left[\frac{\rho_g(Q_i)}{\rho_g(Q')} \right]^{1/6} \frac{e^{-jk(\ell_i + S_i)}}{\sqrt{S_i(S_i + \ell_i)}} \hat{b}_i \quad (3.21b)$$

with

$$P_{\text{dark}} = \frac{-jZ_0}{4\pi} \left\{ \frac{1 - \cos(kL)}{\sin(kL)} \right\} \quad (3.22)$$

Note that the expressions in the lit region are derived by employing Ivanov's result [12]. Thus, these expressions are not the same as those obtained by UTD. However both expressions agree with the measured results as shown by Wang [12].

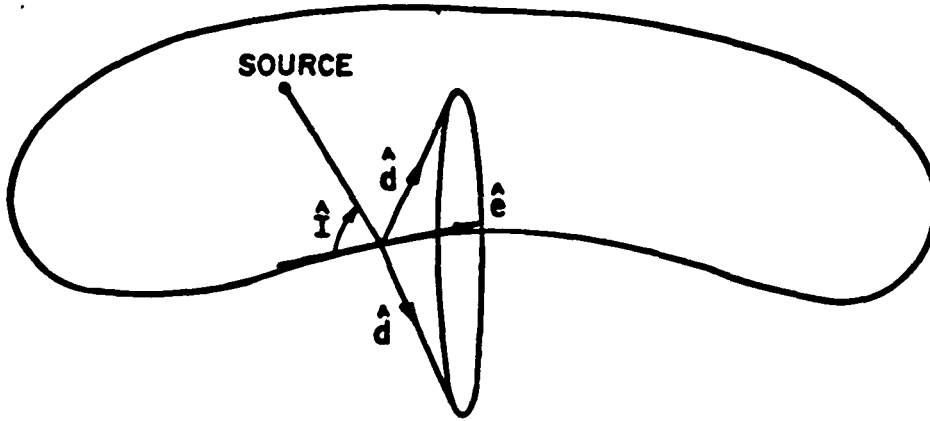


Figure 3.7. A cone of diffracted rays from a curved ground plane.

where \hat{I} is the incident unit vector from the source to the diffraction point,

\hat{d} is the diffraction unit vector, and

\hat{e} is the unit vector parallel to the diffracting edge.

An edge fixed coordinate system is introduced to define the polarizations of the incident and diffracted fields. This coordinate system can be expressed as follows:

$$\begin{aligned}
 \hat{\phi}' &= -\hat{e} \times \hat{I} / |\hat{e} \times \hat{I}| \\
 \hat{\beta}'_0 &= \hat{\phi}' \times \hat{I} \\
 \hat{\phi} &= \hat{e} \times \hat{d} / |\hat{e} \times \hat{d}|, \text{ and} \\
 \hat{\beta}_0 &= \hat{\phi} \times \hat{d}
 \end{aligned} \tag{3.24}$$

As illustrated in Figure 3.2, the surface diffracted field $d\bar{E}_e$ at point p_s in the shadow region can be expressed as follows [14]:

$$d\bar{E}_e(p_s) = \frac{-jkZ_0}{4\pi} d\bar{p}_e(Q') \cdot [\hat{n}'\hat{n}H_0 + \hat{n}'\hat{b}T_0S_0] e^{-jks} \sqrt{\frac{\rho_c}{(\rho_c+s)s}}$$

where

$$H_0 = \sum_p L_p^h(Q') \exp[-jkt - \int_{Q'}^Q \alpha_p^h(t') dt'] \sqrt{\frac{d\psi_0}{dn(Q)}} D_p^h(Q) \quad \text{and}$$

and

$$S_0 = \sum_p L_p^s(Q') \exp[-jkt - \int_{Q'}^Q \alpha_p^s(t') dt'] \sqrt{\frac{d\psi_0}{dn(Q)}} D_p^s(Q) . \quad (3.25)$$

Note that $D_p^{s,h}$ and $\alpha_p^{s,h}$ are the Keller's surface diffraction and attenuation coefficients respectively [6]. They are both related to the Airy function, and $L_p^{s,h}$ are the launching coefficients. Equations (3.1) and (3.25) are two asymptotic representations to the surface diffracted field in the shadow region. In the deep shadow region, Equation (3.25) works better; in the region near the shadow boundary, Equation (3.1) gives a better result. The surface ray field between Q' and Q is not the true field on the surface; it is a boundary layer field [6]. If the surface ray field comes to an edge, the true field of this incident ray can be approximated by Equation (3.25) with the modification of the following parameters [14]:

$$D_p^h(Q) = \frac{1}{2} D_h^{\text{edge}} L_p^h(Q) \quad \text{and} \quad (3.26)$$

$$D_p^s(Q) = \frac{1}{2} \left[\frac{\partial D_s^{\text{edge}}}{\partial \phi'} \right] \bigg|_{\phi'=0} (L_p^s(Q)) \frac{1}{\sin \beta_0} . \quad (3.27)$$

Again, D_p^S and D_p^h are the diffraction coefficients for the soft and hard cases, respectively; whereas, D_s^{edge} and D_h^{edge} are the usual edge diffraction coefficients [15]. Furthermore, L_p^h and L_p^S are the attachment coefficients. By reciprocity, they are the same as the launching coefficients.

The expression for the incident ray can be simplified if the following relationship is utilized [14]:

$$\frac{1}{2} \sum_p L_p^h(Q') e^{-\int_0^Q \alpha_p^h(t') dt'} L_p^h(Q) = \tilde{v}(\epsilon)/\sqrt{t}, \quad \text{and} \quad (3.28)$$

$$\frac{1}{2} \sum_p L_p^S(Q') e^{-\int_0^Q \alpha_p^S(t') dt'} L_p^S(Q) = \left(\frac{-j}{kt}\right) \frac{1}{\sqrt{t}} \tilde{u}(\epsilon) \quad (3.29)$$

where $\tilde{v}(\epsilon)$ and $\tilde{u}(\epsilon)$ are the generalized Fock integrals defined in Reference [15].

The resulting diffracted field can be expressed as follows:

$$-d \frac{Ee(Ps)}{4\pi} = -j \frac{kZo}{4\pi} dPe(Q').$$

$$\begin{aligned} & \left[\begin{array}{l} -\hat{n}'(\hat{n}' \cdot \hat{\phi}') \hat{\phi} D_h^{\text{edge}}(\phi, \phi'=0) \tilde{v}(\epsilon) \\ -\hat{n}'(\hat{b} \cdot \hat{\beta}'_0) \hat{\beta}'_0 T_0 \frac{\partial}{\partial \phi'} D_s^{\text{edge}}(\phi, \phi'=0) \frac{-j\tilde{u}(\epsilon)}{ktsin\beta_0} \end{array} \right] \cdot \\ & \frac{e^{-jkt}}{\sqrt{t}} \sqrt{\frac{d\psi_0}{\rho_c d\psi}} \sqrt{\frac{\rho}{(\rho+s)s}} e^{-jks} \quad (3.30) \end{aligned}$$

Note that ρ is the second caustic location related to the edge diffracted field and is defined in Equation (3.47). All other parameters are the same as those in the shadow region unless they have been specified otherwise in this section.

Expressions for the soft and hard edge diffraction coefficients are given as follows:

$$D_{s,h}(L_\ell, \phi, \phi', \beta) = \frac{-e^{-j\pi/4}}{2n\sqrt{2\pi k} \sin\beta_0} \left[\cot\left(\frac{\pi+\beta^-}{2n}\right) F(KL_\ell a^+(\beta^-)) \right. \\ \left. + \cot\left(\frac{\pi-\beta^-}{2n}\right) F(KL_\ell a^-(\beta^-)) \mp \left\{ \cot\left(\frac{\pi+\beta^+}{2n}\right) F(KL_\ell a^+(\beta^+)) \cdot \right. \right. \\ \left. \left. + \cot\left(\frac{\pi-\beta^+}{2n}\right) F(KL_\ell a^-(\beta^+)) \right\} \right] \quad (3.31)$$

where the minus sign applies for D_s and the plus sign applies for the D_h . The angle parameter β is given by

$$\beta^\mp = \phi \mp \phi'$$

and

$$a^\pm(\beta^\pm) = 2 \cos^2 \left[\frac{2\pi n N^\pm - \beta^\pm}{2} \right] \quad (3.32)$$

The number (N) is desined as the integer which most nearly satisfy the following equations [16]:

$$2\pi n N^+ - \beta^+ = \pi$$

and

$$2\pi n N^- - \beta^- = -\pi \quad .$$

Then, β^- is associated with the incident field and β^+ is associated with the reflected field. The wedge angle number (N) is given by

$$n = 2 - \frac{WA}{\pi} \quad (3.33)$$

and the wedge transition function is expressed as [16]

$$F(x) = 2j \sqrt{x} e^{jx} \int_{\sqrt{x}}^{\infty} e^{-jt^2} dt \quad (3.34)$$

The magnitude and phase of this transition function is shown in Figure 3.8. The distance parameter (L_g) which is equal to $t \sin^2 \beta_0$ for the curved ground plane case. Also other parameters are defined as follows:

$$\phi = \pi - \tan^{-1} \frac{\hat{d} \cdot \hat{n}}{\hat{d} \cdot \hat{t}}$$

$$\phi' = 0$$

$$\beta_0 = \cos^{-1}(\hat{e} \cdot \hat{d})$$

and

$$n \approx 2.$$

6. SOLUTIONS OF A FLAT GROUND PLANE

Figure 3.9 shows the structure of a flat ground plane. The solution for a monopole mounted on the surface is given by:

(a) Incident Field

$$\vec{E}^i = \begin{cases} \hat{\theta} P_{lit} \sin \theta \frac{e^{-jkR}}{R} & 0 < \theta < 90^\circ, \text{ and} \\ 0 & \text{otherwise} \end{cases} \quad (3.35)$$

where P_{lit} is defined in Equation (3.20).

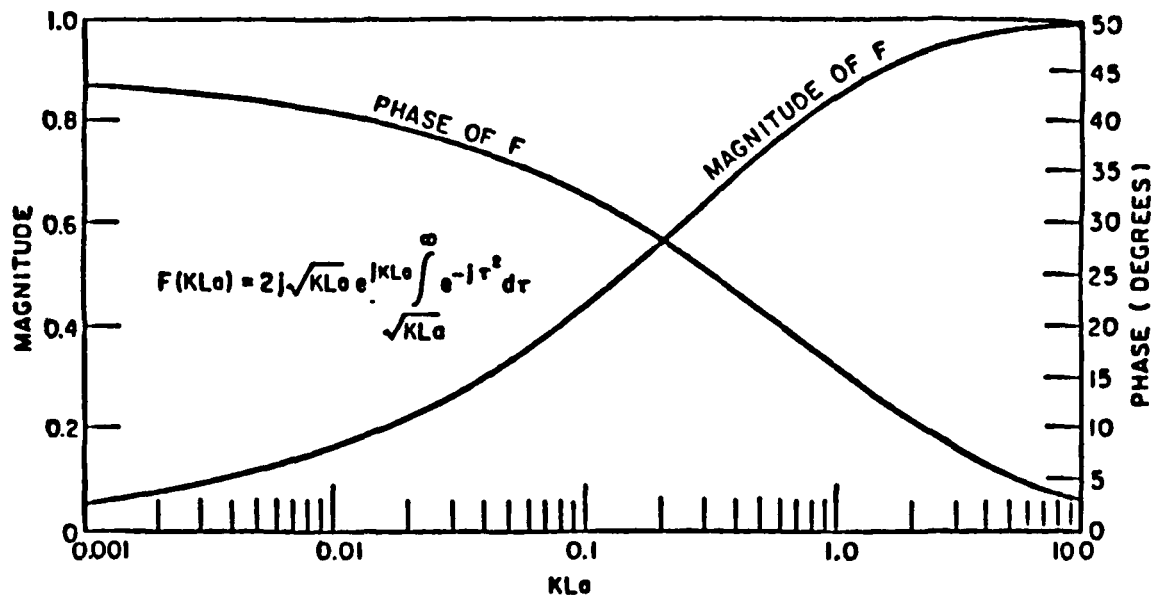


Figure 3.8. Transition function.

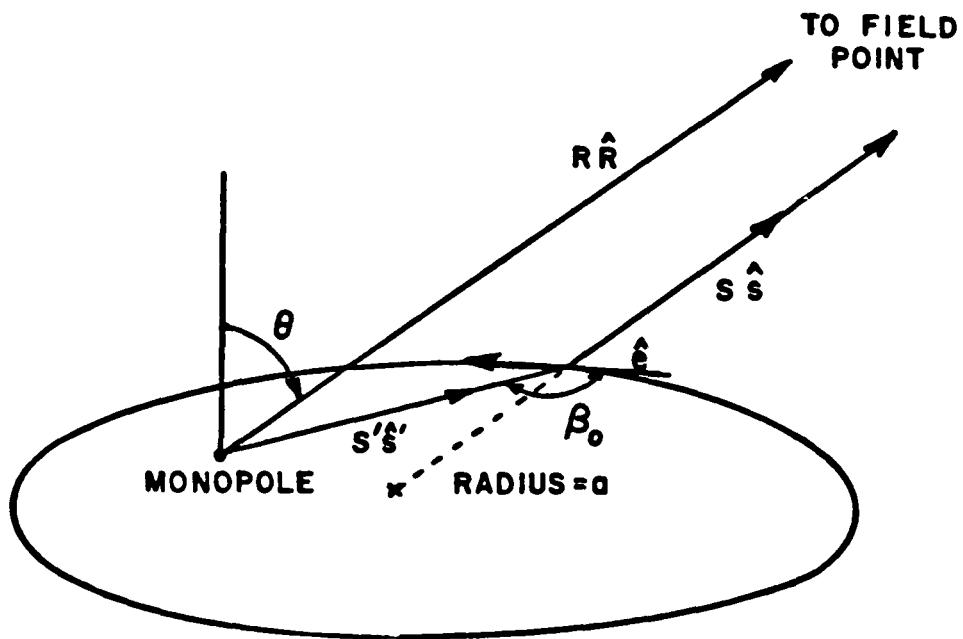


Figure 3.9. Geometry of a monopole radiating from a flat ground plane.

(b) Diffracted field

$$\bar{E}^d = \hat{\phi} \left(-\frac{D_h}{2} \right) \sqrt{\frac{\rho}{s(\rho+s)}} e^{-jks} E_{\phi}^i, \quad (3.36)$$

where

D_h is defined in Equation (3.31) and

$\hat{\phi}$ is defined in Equation (3.24).

The second caustic location (ρ) related to the edge diffracted field and is given by

$$\frac{1}{\rho} = \frac{1}{s'} - \frac{\hat{n}_e \cdot (\hat{s}' - \hat{s})}{a \sin^2 \beta_0} \quad (3.37)$$

where \hat{n}_e is the normal to the edge curvature. The incident field (E_{ϕ}^i) is given by

$$E_{\phi}^i = P_{lit} \frac{e^{-jks'}}{s'} \quad (3.38)$$

Finally, the total field is the sum of the diffracted field and the incident field. Some patterns will be run in Chapter V.

CHAPTER IV

TCAS II SYSTEM

A. INTRODUCTION

The TCAS II system is a midair collision avoidance system which consists of top and bottom mounted, eight-element, electronically scanned arrays. These arrays radiate sum and difference beams at 1030 MHz and are designed to receive replies at 1090 MHz. Transmissions are scanned electronically around 360 degrees in azimuth in 5.625 increments with a total of 64 different beam positions. The receiver can provide target bearing estimates with an accuracy of one degree. The bearing estimates are combined with altitude and slant range information to generate accurate 3-D target position and velocity estimates [17]. Figure 4.1 illustrates a TCAS II system in operation [1].

B. THE TCAS II SYSTEM

The TCAS II system employs a pair of 10.5 inch diameter circular arrays of eight top loaded monopoles. A Butler Matrix is used to generate the sum and difference patterns as shown in Figure 4.2.



Figure 4.1. A TCAS system displays a commercial plane (center) and two encroaching planes. The transponder on one of the latter planes has an altitude-reporting feature (-12 indicates it is 1200 feet below the TCAS plane); the second plane's transponder lacks this feature, as indicated by the question marks [1].

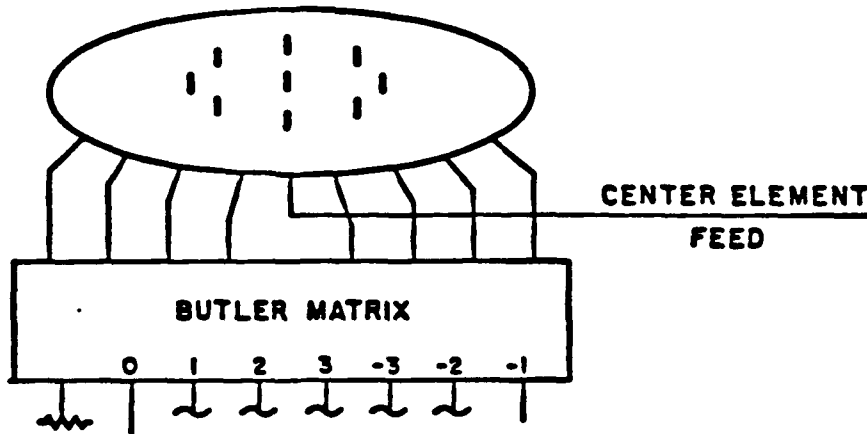


Figure 4.2. Beam forming network which uses a Butler matrix to determine the element excitations.

The Butler Matrix operates in such a manner that given the mode inputs, the normalized element excitations are given by [3]

$$E_i = \frac{1}{\sqrt{N}} \sum_{\ell=-N/2+1}^{N/2} (A_{\ell}) \exp [jP_{\ell} + j2\pi i\ell/N] \quad (4.1)$$

where

E_i = complex excitation of the i^{th} element (volts)

A_{ℓ} = amplitude of the ℓ^{th} mode input (volts)

P_{ℓ} = phase of the ℓ^{th} mode input (radians)

M_{ℓ} = complex excitation of the ℓ^{th} mode (volts), and

N = number of elements (in this case $N=8$).

A circular array is shown in Figure 2.2 in which the elements are numbered counterclockwise. The x-axis in Figure 2.2 points toward the nose of a aircraft when the y-axis points toward the right wing. To steer the beam θ radians in the counterclockwise direction, a negative phase gradient is applied across the mode inputs such that

$$M_{\ell} = A_{\ell} \rho^{j[P_{\ell} - \ell \theta]} \quad (4.2)$$

When the beam is pointing toward the nose of the aircraft, the mode and element excitations are given in Table 4.1. The corresponding sum and difference patterns, if neglecting the effects of the tail and wings of the aircraft, are shown in Figure 4.3. The target reply will be fed into a Squinted Beam Monopulse Processor, the output of which gives a monopulse curve. The monopulse characteristic curve corresponding to the above sum and difference patterns is shown in Figure 4.4. The 64 monopulse curves corresponding to the 64 beam positions are not quite the same curve. To determine the actual azimuth angle of a target, the processor output is compared with a lookup table to compensate for the differences between the 64 monopulse curves.

C. COMPUTER MODEL OF THE TCAS II SYSTEM

The OSU aircraft code is used to simulate the radiation patterns of the TCAS II mounted on the top of a Boeing 737. The circular array is modeled by eight pairs of monopoles as shown in Figure 4.5. Each monopole pair is used to model a top loaded monopole. In order to

TABLE 4.1

MODE INPUTS AND ELEMENT EXCITATIONS FOR Σ AND Δ BEAMS
AT ZERO DEGREE AZIMUTH

(a) ELEMENT EXCITATIONS FOR Σ AND Δ BEAMS
AT ZERO DEGREES AZIMUTH (TOWARD NOSE OF AIRCRAFT)

ELEMENT EXCITATIONS: SUM BEAM

ELEMENT NO.	AMPLITUDE	PHASE (DEGREES)
1	.482	32.3742
2	.109	37.8493
3	.234	-78.1094
4	.232	-48.9456
5	.240	-78.2374
6	.105	35.5149
7	.477	32.0745
8	.592	9.1814

ELEMENT EXCITATIONS: DIFFERENCE BEAM

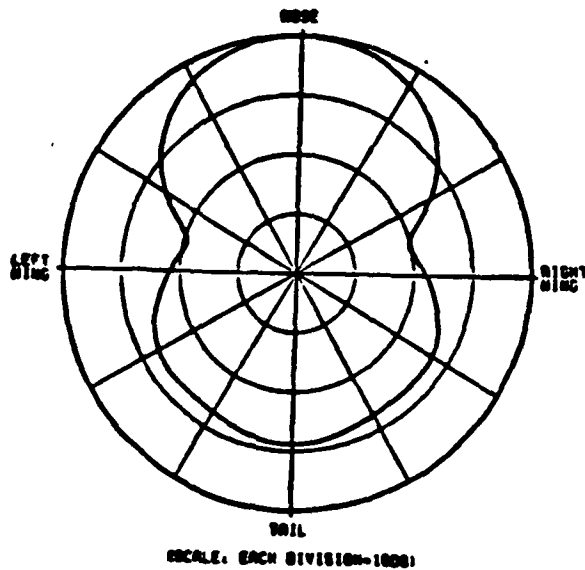
ELEMENT NO.	AMPLITUDE	PHASE (DEGREES)
1	.371	90.9364
2	.537	135.1673
3	.137	150.721
4	.104	4.03708
5	.259	-.270649
6	.543	-42.3221
7	.427	-88.7265
8	.021	-30.3929

TABLE 4.1 (continued)

(b) MODE INPUTS TO BUTLER MATRIX TO PRODUCE THE Σ
AND Δ BEAM ELEMENT EXCITATIONS

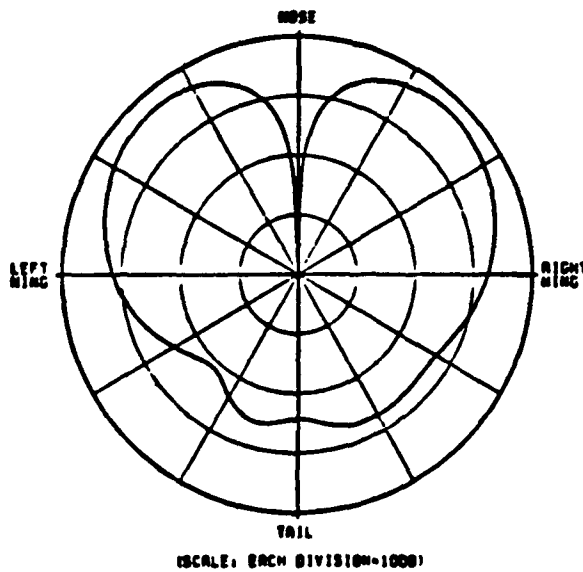
MODE INPUTS: SUM BEAM		
MODE NO.	AMPLITUDE (VOLTS)	PHASE (DEGREES)
-3	.152	-99.9442
-2	.214	-19.8993
-1	.473	46.14
0	.644	3
1	.478	45.163
2	.214	-20.545
3	.152	-99.671
4	.00101	0

MODE INPUTS: DIFFERENCE BEAM		
MODE NO.	AMPLITUDE (VOLTS)	PHASE (DEGREES)
-3	.209	76.0642
-2	.254	151.01
-1	.683	-142.86
0	.102	4
1	.537	39.163
2	.324	-24.545
3	.161	-105.67
4	.00101	0



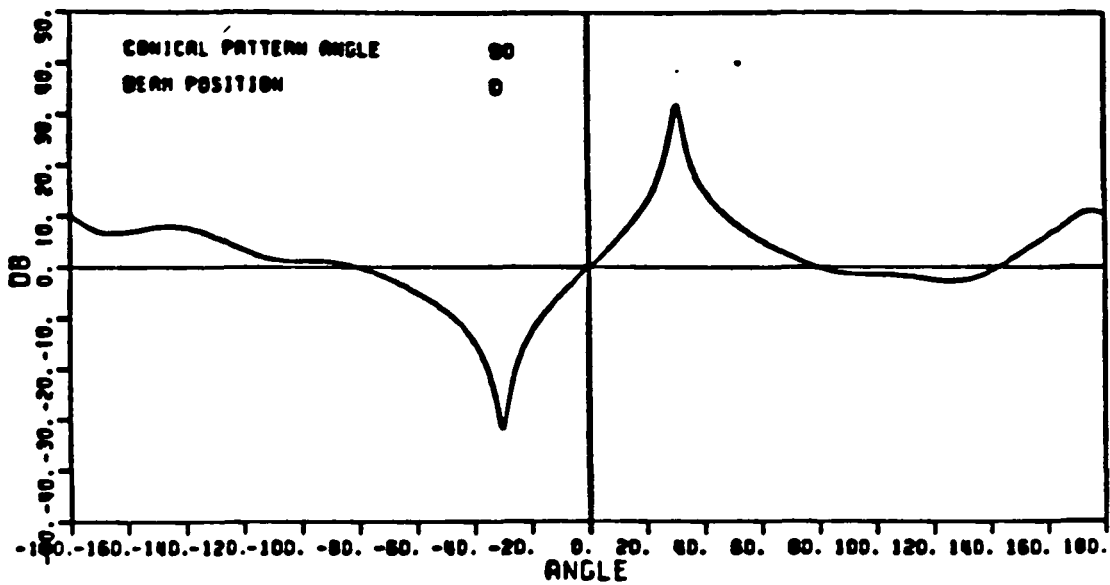
NORMALIZED TO 8.0 dB
 ETH POLARIZATION
 FREQ. = 1.06 GHz
 THC = 90.0
 PHC = 0.0
 THETA = 75.0

(a) Sum beam

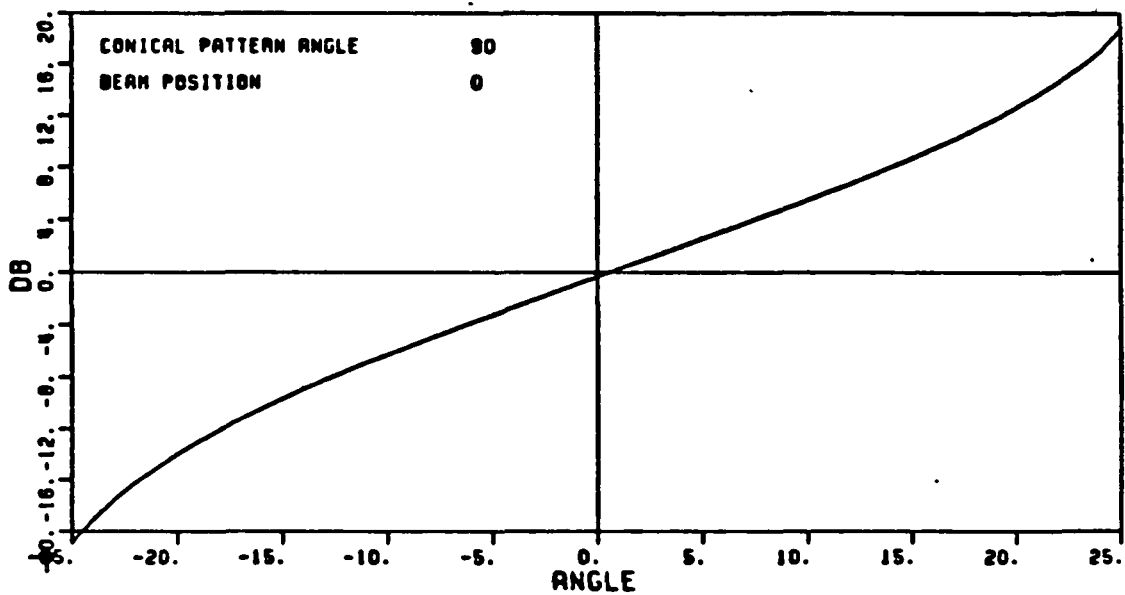


(b) Difference beam

Figure 4.3. Sum and difference beams pointed in the nose direction. The aircraft is modeled by a fuselage only.



(a) Ideal TCAS II monopulse characteristic curve.



(b) Expanded monopulse characteristic curve showing linearity around antenna boresight.

Figure 4.4. Ideal TCAS II monopulse characteristic curve and its expanded version.

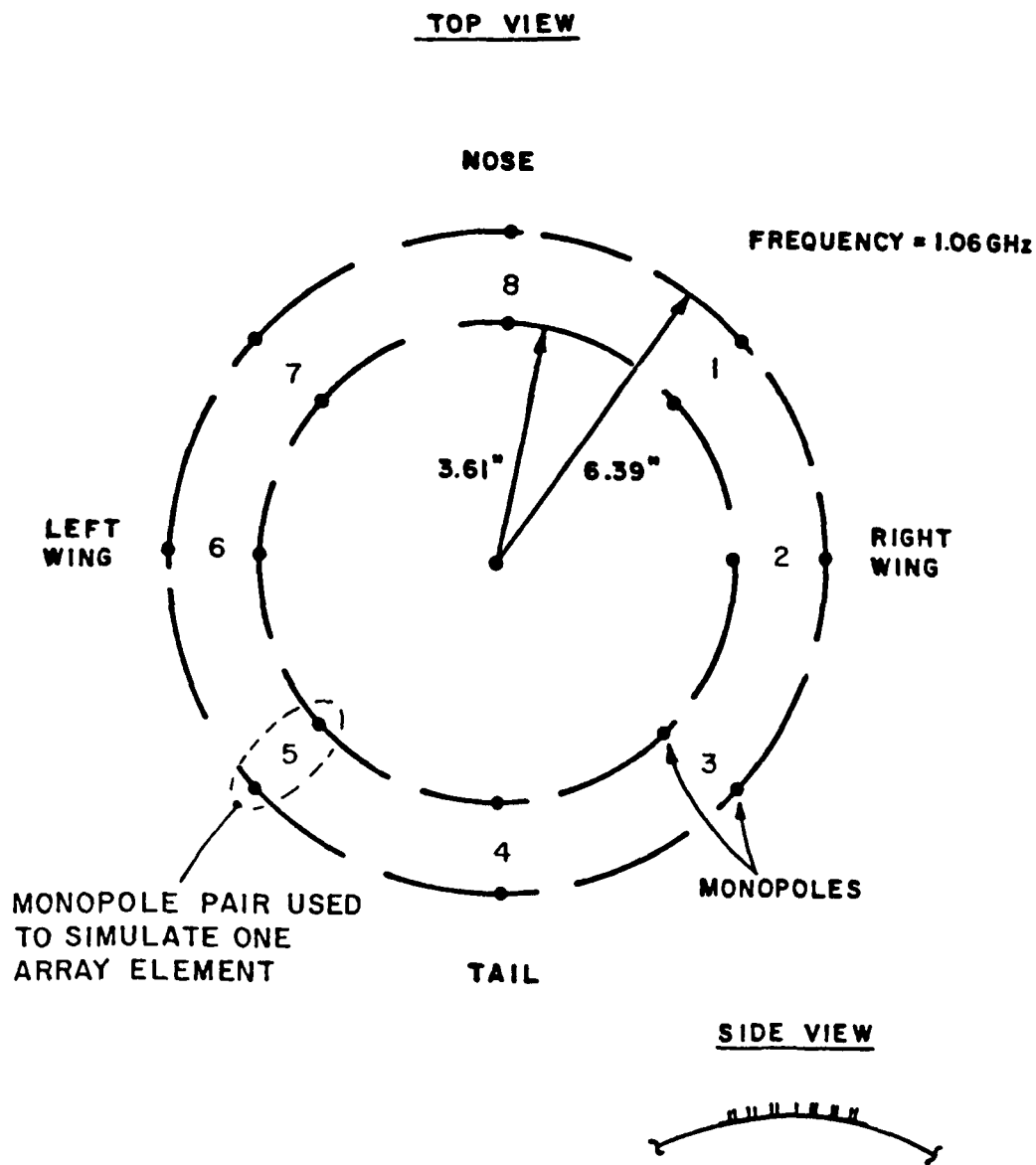


Figure 4.5. Geometry of the computer model that was used to simulate the circular array.

include the coupling effects between the top loaded elements, the model has been designed as follows. First, the two monopoles in every pair are separated by $\lambda/4$ and out of phase by 90° . Second, the radiation pattern from each monopole pair will give a 15 dB front to back ratio. The above requirements can be achieved by exciting the inner monopole of each pair with a signal of amplitude (.698) and phase (45°) and the outer monopole with amplitude (1.0) and phase (-45°), as defined by Sinsky [18].

To generate a pattern cut, the aircraft code is executed eight times. Each execution gives a pattern cut due to one pair of elements. The sum and difference patterns are obtained by first multiplying the corresponding element excitation to each element pattern, then summing the eight weighted patterns to produce a steered Σ or Δ beam.

CHAPTER V

ANALYSIS OF TCAS II SYSTEM ON A CURVED SURFACE

A. INTRODUCTION

The objective of this chapter is to answer the following questions: Can a curved ground plane be used to model the structure of an airplane; or, at least, can it be used to model the fuselage of an aircraft? To answer these questions, two programs have been written. The first program simulates the far-field patterns of a TCAS II mounted on a flat ground plane. The second program models the TCAS II mounted on a curved ground plane. The simulated structures are shown in Figure 5.1.* The simulated results will be compared with those computed by the aircraft code. The aircraft used for this study was the Boeing 737 as shown in Figure 5.2. The computer model of the Boeing 737 and its input data set are shown in Figure 5.3 and Table 5.1, respectively. Furthermore, it is also necessary to define the geometry of the simulated patterns as shown in Figure 5.4. The 737 was chosen because its structure is relatively simple, and the simulated results agree well with the measured data.

*Note: For the convenience of the reader, all figures and tables referred to in Chapter V have been grouped together at the end of the chapter.

B. PATTERNS FROM A CURVED GROUND PLANE

Before making any comparisons, the success of the curved ground plane program must be verified. With an infinite radius of curvature, the curved ground plane results should be the same as those of a flat ground plane. For this purpose, the element patterns and the monopulse characteristic curves for the TCAS II mounted on a curved and flat ground are shown in Figures 5.5 and 5.6. The corresponding sum and difference patterns are shown in Figures 5.7 and 5.8. Comparing these patterns, one should observe that the curved ground plane patterns agree very well with those for the flat one. Note that the flat ground plane results have been verified by comparisons with previously published results.

If the sum and difference beams of a TCAS II on a flat ground plane are rotated clockwise by 90 degrees, the monopulse curve in each case is found to be unchanged as shown in Figure 5.9. Thus, it can be concluded that for the same elevation angle, the Butler Matrix will not affect the monopulse characteristic curves even though the beams are steered in different directions. If the monopulse curves change when the beam direction changes, it must be due to the curvature of the surface.

Next, the curved ground plane program is checked with the aircraft code when the surface radius of curvature is finite. The line-of-sight signal from the TCAS II array mounted on a curved ground plane should be similar to the line-of-sight signal when the TCAS II array is mounted on a long ellipsoid as illustrated in Figure 5.10. The input data for this ellipsoid is shown in Table 5.2. The sum and difference patterns for

each case are illustrated in Figure 5.11 and the corresponding monopulse characteristic curves are shown in Figure 5.12. Comparing the patterns between the two cases, it can be seen that the simulated results agree well with those using the aircraft code. Note that only the aircraft fuselage is present in these results.

There are still more questions that need to be answered. First, if the curvature of a curved ground plane is set equal to the curvature of an aircraft at the TCAS II location, then will the curved ground plane accurately simulate the system mounted on the fuselage? Next, if the diffracted field is also included in the curved ground plane, how well does the curved ground plane model simulate the fuselage in terms of the resulting patterns? To answer the first question, it is necessary to compare the monopulse curves for an aircraft mounted system with that of a curved ground plane with the same curvature. First, only the source term is used to generate the monopulse characteristic curve of the curved ground plane as illustrated in Figure 5.12. It can be seen that they agree very well. The corresponding sum and difference patterns also agree with each other as shown in Figure 5.11. Thus, it can be concluded that if only the source term is considered, a curved ground plane can be used to model the fuselage of an aircraft with the same curvature.

To answer the second question, the total field of a curved ground plane, that is the sum of the incident and edge diffracted fields, needs to be compared with the total field of the fuselage of a Boeing 737, that is the incident and surface diffracted fields. Figure 5.13 shows

the element patterns for the two cases. The sum and difference patterns and also their corresponding monopulse characteristic curves at different beam positions are shown in Figures 5.14 to 5.23. Comparing the curves for the curved ground plane versus the Boeing 737 fuselage, it can be concluded that the edge diffracted field included in the curved ground plane solution causes a slight error in the monopulse curves if the curved ground plane is used to model the fuselage of a Boeing 737. However, this error is small compared to the error introduced by the other structures associated with a Boeing 737 as will be shown next. Before leaving this section, it is important to note that this curved ground plane solution is valid only for a certain range of elevation angles as will be discussed in section D.

C. PATTERNS OF A BOEING 737 MODEL

The OSU aircraft code is used to study the radiation patterns of the TCAS II system. Ideally, the shape of the the sum and difference beams will not change as the array is scanned around in the azimuth plane. However, the fuselage, wings, tail and other structures will distort the antenna patterns; consequently, the performance of the monopulse receiver will be affected. Thus, it is important to study the structural effects of an aircraft on the radiation patterns of a TCAS II. References [19] and [20] give detailed results for this issue.

To examine the structural effects of a Boeing 737, Figures 5.24 to 5.38 show the sum and difference patterns and also the corresponding monopulse characteristic curves for the following cases:

- (a) a complete Boeing 737,
- (b) a 2-ft curved ground plane with a curvature of 6-ft, and
- (c) fuselage only of a Boeing 737.

Comparing the monopulse characteristic curves for the three cases, it is found that (b) and (c) can be used to model (a) moderately well if the beam position is not near the tail section. However, when the beam positions approach the tail section, the aircraft cannot be modeled by a curved ground plane. The most severely affected region is in the direction of the tail. The large distortions in the patterns are caused by shadowing of the vertical stabilizer.

There is one more observation to make. How does a monopulse curve change with elevation angle? For a fixed beam position, the monopulse curves spread to the same extent for a flat or a curved ground plane as shown in Figures 5.39 to 5.41. As shown in Figure 5.42, the monopulse curve changes quite dramatically for all beam positions and elevation angles between 20° and 40° . The change was not due to the elevation angle changing based on the results shown in Figures 5.40 to 5.42. The major variation of the monopulse curve is due to the beam position as verified by the data shown in Figure 5.43. This verifies the need for a curved ground plane and the need for a lookup table associated with each beam position.

D. LIMITATIONS OF THE SIMULATION

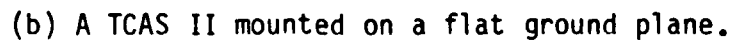
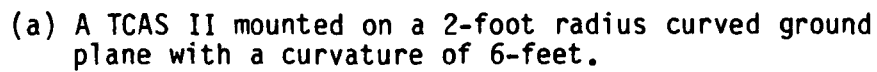
This curved ground plane program only works for a particular range of elevation angles. At the frequency of 1.09 GHz, the program works

only when the elevation angle is between 18° and 75° . Perhaps a combination of UTD and some other techniques need to be used for a complete simulation. When the elevation angle is larger than 75° , there is a sudden increase in the number of diffraction points which causes the diffracted field to be discontinuous; i.e., a caustic. When the elevation angle is lower than 18° , the diffracted field is blocked by the ground plane which once again causes a discontinuous diffracted field. Also, it should be noted that the curved ground plane solution used here is not an exact solution because higher order terms such as double diffraction are not included. To verify these results, measured data should be taken and compared with the present findings.

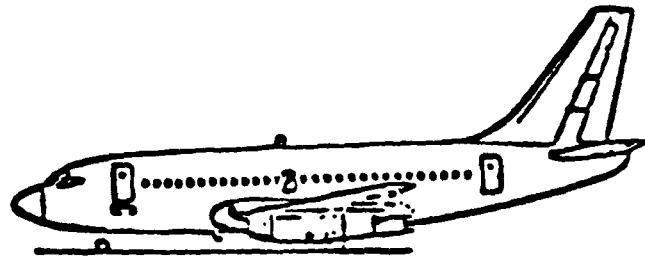
TABLE 5.1

INPUT DATA FOR TCAS II
AIRCRAFT CODE: ELLIPSOID VERSION

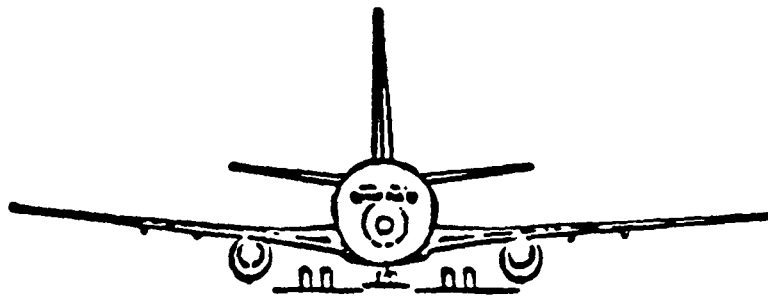
UN: INCHES	BO:	EX:
3	T	SG: ELEMENT 5
FQ: 1.06 GHZ	PP: POLAR FLOT IN DB	-2.64,73.536
1,1.06,1.	F	2
FG: BOEING 737	1,1.5,3	1.39,135.
77.,74.,830.,308.56	PD: AZIMUTH PLANE	0.,0.,0.,2.78,3
T	90.,0.,90.	1.,-45.
0.,0.,70.	0,360,1	1.39,-45.
SG: ELEMENT 1	T,1000000.	0.,0.,0.,2.78,3
2.64,66.464	EX:	.698,45.
2	SG: ELEMENT 2	EX:
1.39,-45.	3.73,70.	SG: ELEMENT 6
0.,0.,0.,2.78,3	2	-3.73,70.
1.,-45.	1.39,0.	2
1.39,135.	0.,0.,0.,2.78,3	1.39,180.
0.,0.,0.,2.78,3	1.,-45.	0.,0.,0.,2.78,3
.698,45.	1.39,180.	1.,-45.
FG: RIGHT WING	0.,0.,0.,2.78,3	1.39,0.
4,T	.698,45.	0.,0.,0.,2.78,3
1.,75.,67.952	EX:	.698,45.
1.,536.93,316.14	SG: ELEMENT 3	EX:
1.,536.93,379.86	2.64,73.536	SG: ELEMENT 7
1.,75.,240.26	2	-2.64,66.464
FG: LEFT WING	1.39,45.	2
4,T	0.,0.,0.,2.78,3	1.39,225.
1.,-75.,240.26	1.,-45.	0.,0.,0.,2.78,3
1.,-536.93,379.86	1.39,225.	1.,-45.
1.,-536.93,316.14	0.,0.,0.,2.78,3	1.39,45.
1.,-75.,67.952	.698,45.	0.,0.,0.,2.78,3
FG: TAIL	EX:	.698,45.
4,T	SG: ELEMENT 4	EX:
77.,8.25,618.55	0.,75.	SG: ELEMENT 8
284.147,8.25,819.056	2	0.,65.
284.147,0.,683.696	1.39,90.	2
77.,0.,483.19	0.,0.,0.,2.78,3	1.39,270.
FG: TAIL	1.,-45.	0.,0.,0.,2.78,3
4,T	1.39,270.	1.,-45.
77.,0.,483.19	0.,0.,0.,2.78,3	1.39,90.
284.147,0.,683.696	.698,45.	0.,0.,0.,2.78,3
284.147,-8.25,819.056		.698,45.
77.,-8.25,618.55		EX:



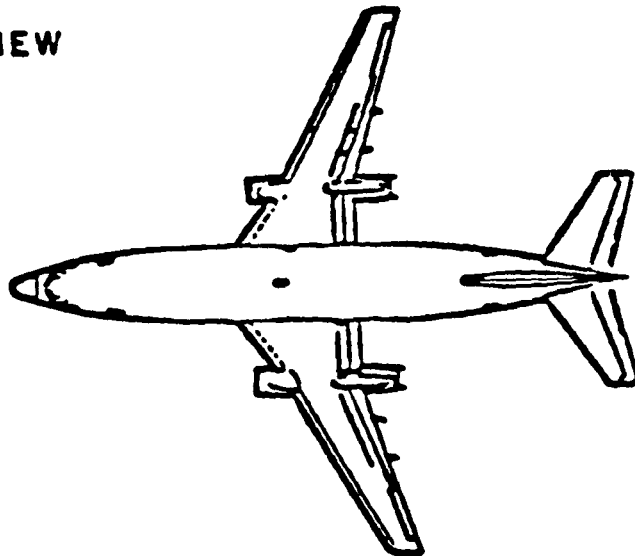
59



(a) SIDE VIEW



(b) FRONT VIEW



(c) TOP VIEW

Figure 5.2. Boeing 737 aircraft.

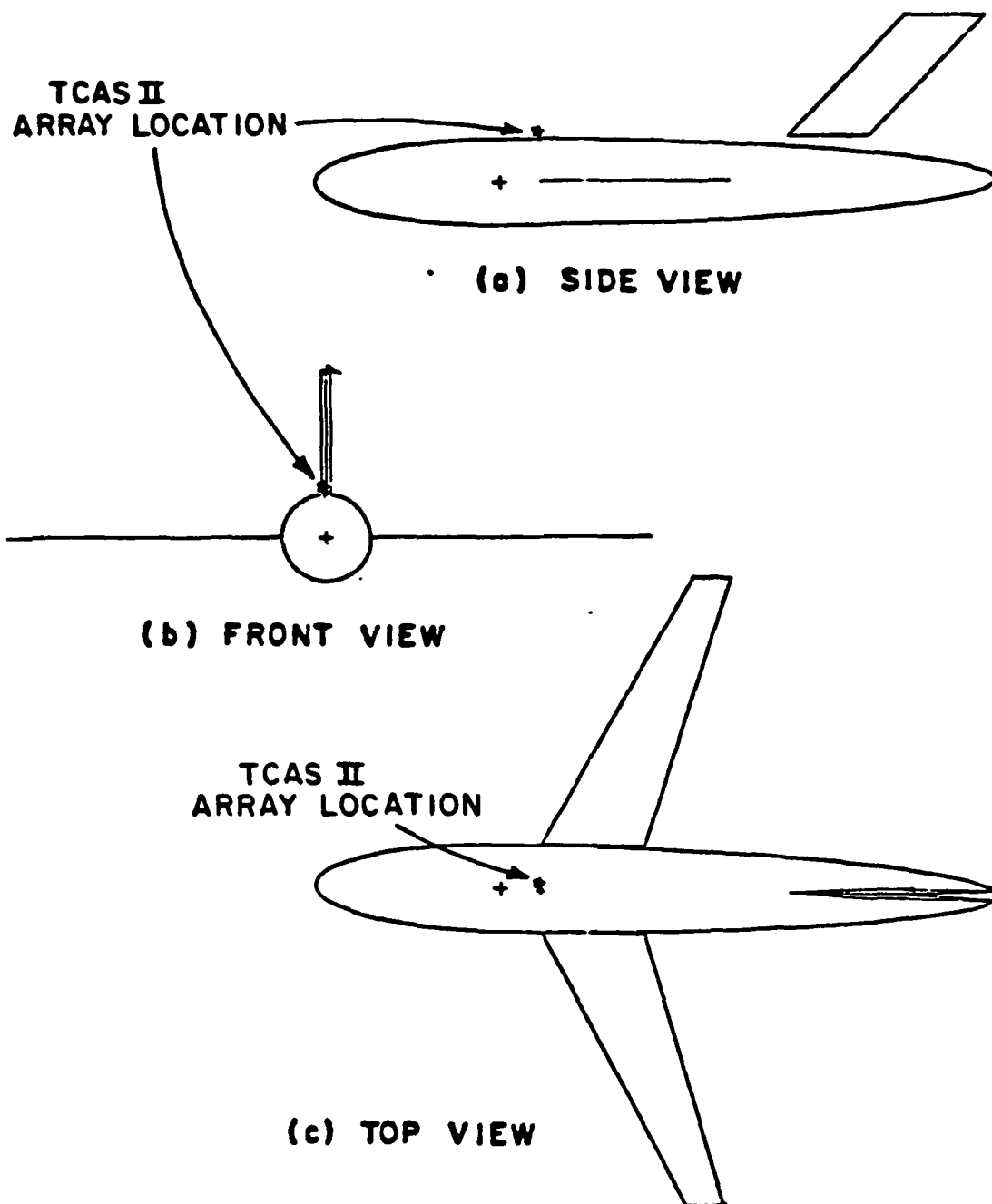
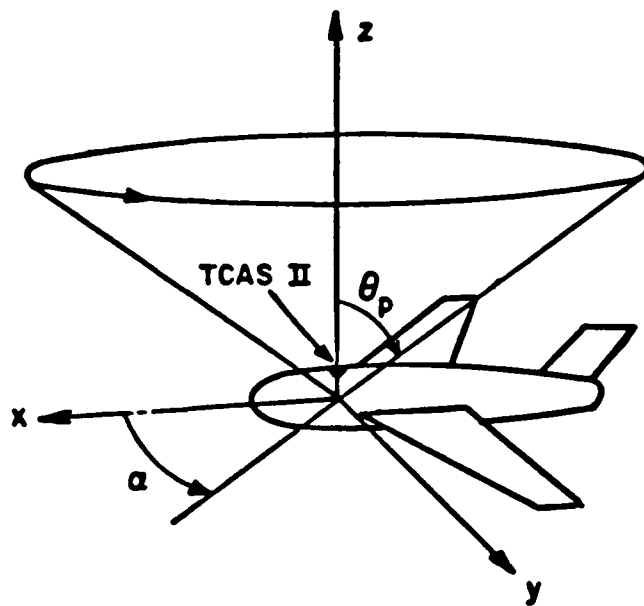


Figure 5.3. Computer-simulated model of the Boeing 737.

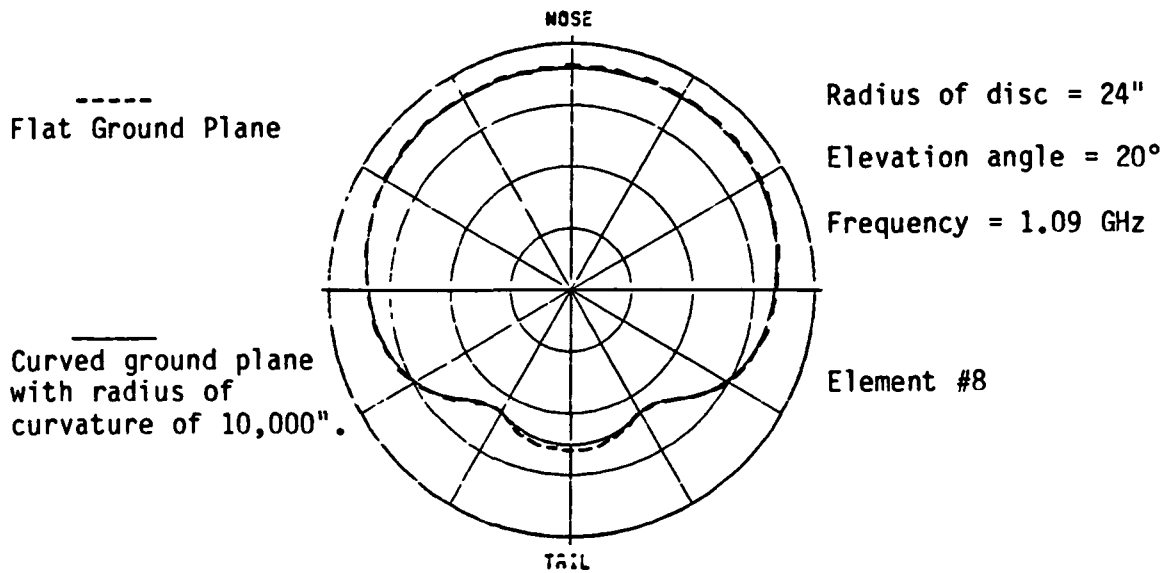


Azimuth Conical Pattern Angle = θ_p

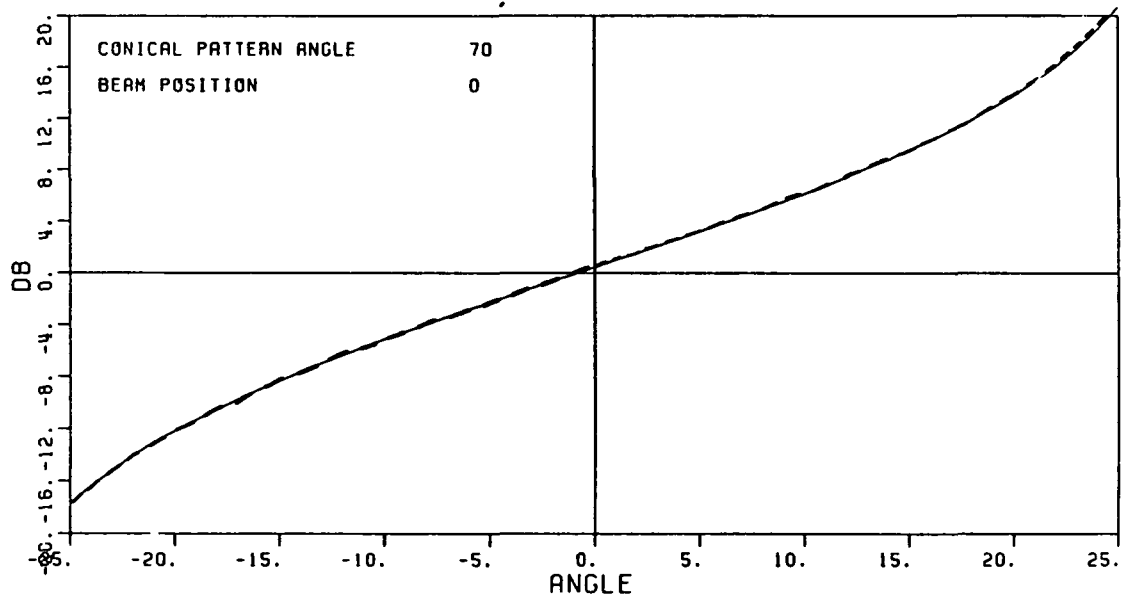
Elevation Angle = $90^\circ - \theta_p$

Beam Position = α

Figure 5.4. Coordinate system for azimuth conical pattern cuts.

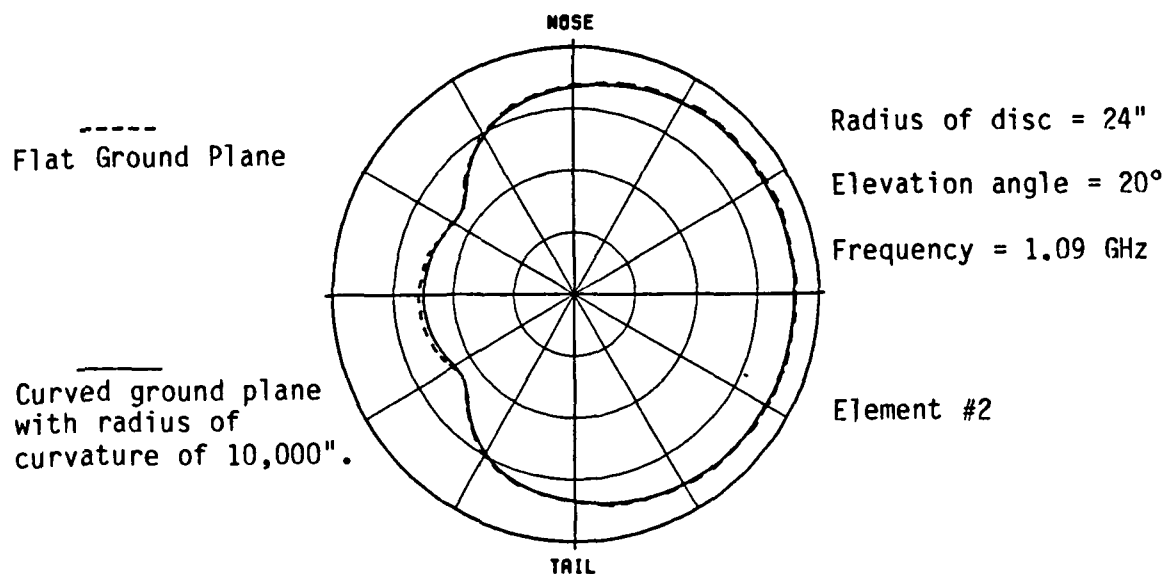


(a) Element patterns.

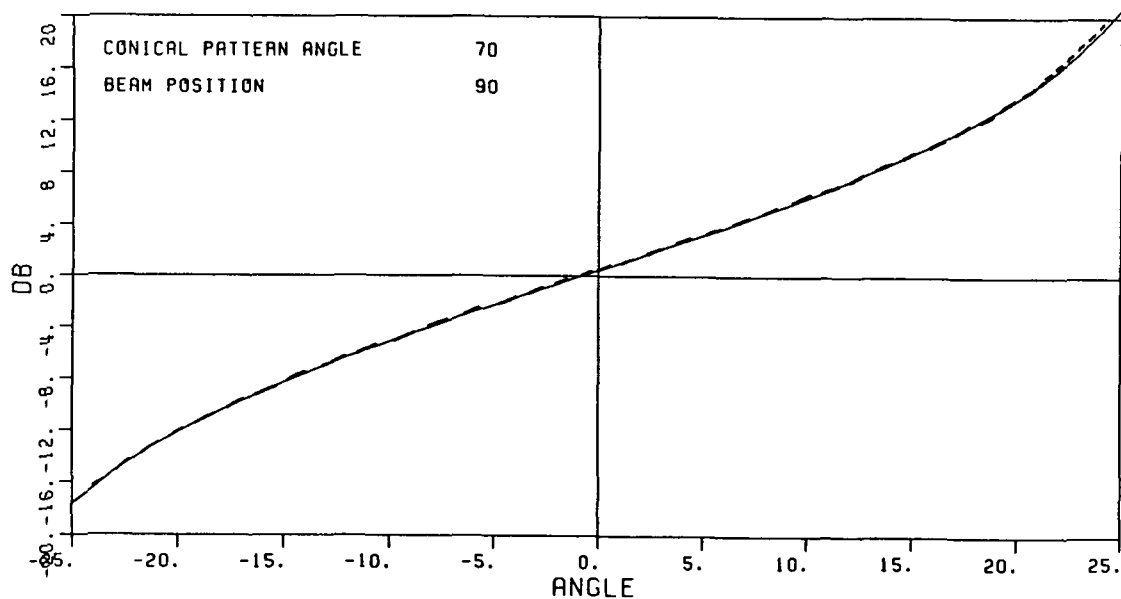


(b) Monopulse characteristics.

Figure 5.5. Comparison of element patterns and monopulse characteristics for a curved and a flat ground plane.



(a) Element patterns.



(b) Monopulse characteristics.

Figure 5.6. Comparison of element patterns and monopulse characteristic for a curved and a flat ground plane.

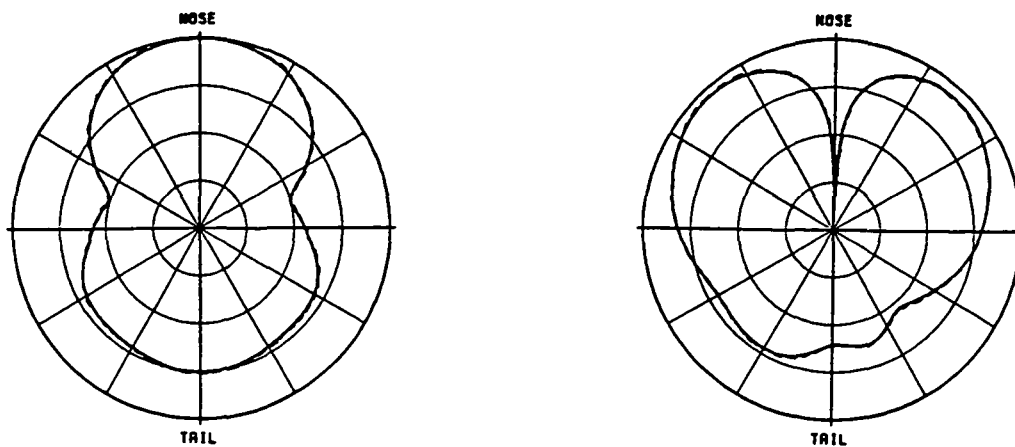


Figure 5.7. The sum and difference patterns corresponding to Figure 5.5.

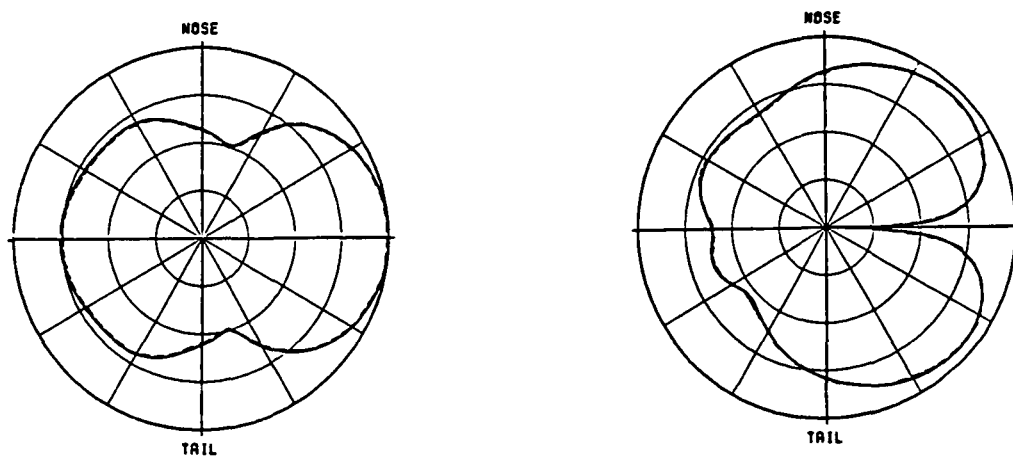


Figure 5.8. The sum and difference patterns corresponding to Figure 5.6.

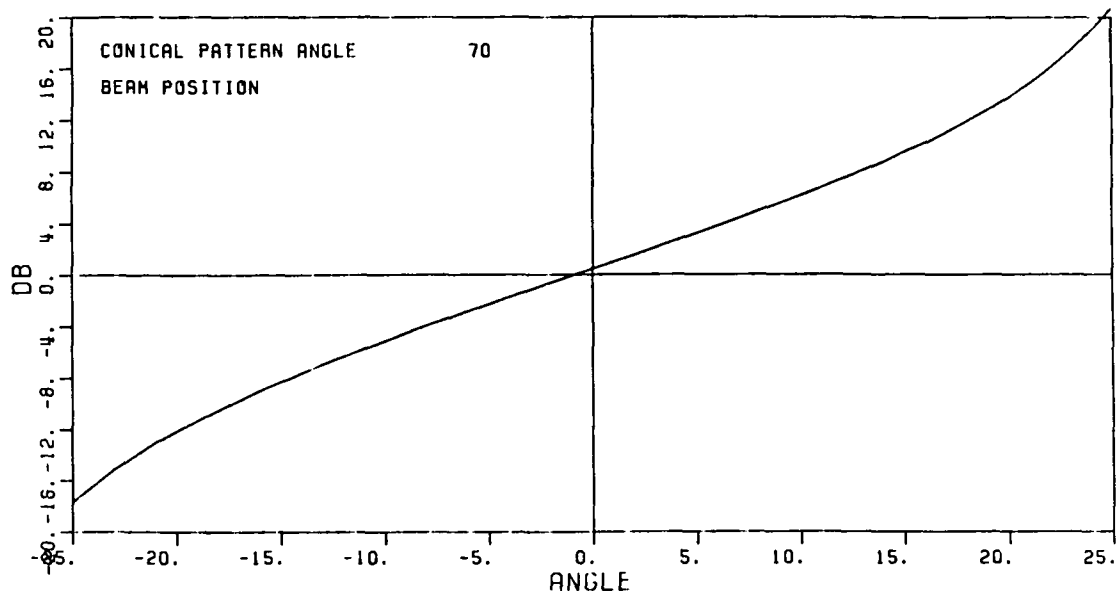


Figure 5.9. Same monopulse characteristic curve when beam positions are 0° , 90° , 180° , and 270° for a flat ground plane.

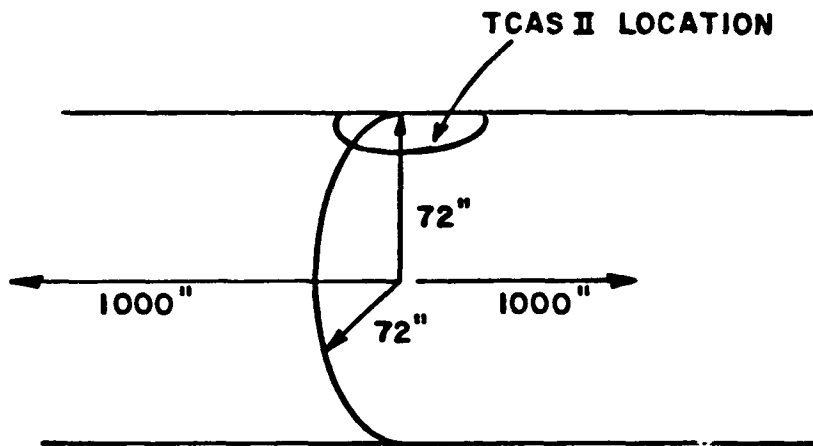
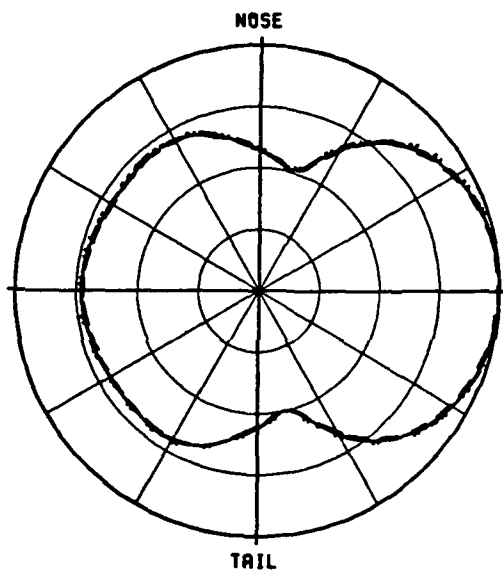


Figure 5.10. The simulated structure of a long ellipsoid. The source field of this structure should be close to the source field of a curved disc with a curvature of $72''$.

TABLE 5.2
INPUT DATA FOR A LONG ELLIPSOID

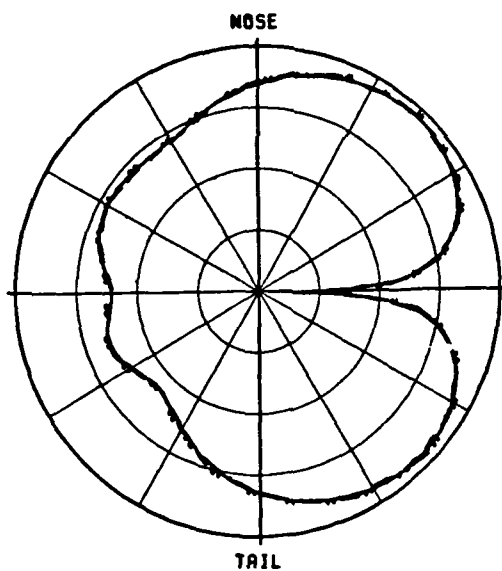
UN: INCHES	SG: ELEMENT 3	SG: ELEMENT 6
3	2.813, 3.536	-3.979, 0.
FQ: 1.09 GHZ	2	2
1, 1.09, 1.	1.39, 45.	1.39, 180.
FG:	0., 0., 0., 2.78, 3	0., 0., 0., 2.78, 3
72., 72., 1000., 1000.	1., -45.	1., -45.
T	1.39, 225.	1.39, 0.
0., 0., 0.	0., 0., 0., 2.78, 3	0., 0., 0., 2.78, 3
BO:	.698, 45.	.698, 45.
T	EX:	EX:
PP: POLAR PLOT IN DB	SG: ELEMENT 4	SG: ELEMENT 7
F	0., 5.	-2.813, -3.536
1, 1.5, 3	2	2
PD: AZIMUTH PLANE	1.39, 90.	1.39, 225.
90., 0., 70.	0., 0., 0., 2.78, 3	0., 0., 0., 2.78, 3
0, 360, 1	1., -45.	1., -45.
T, 1000000.	1.39, 270.	1.39, 45.
SG: ELEMENT 1	0., 0., 0., 2.78, 3	0., 0., 0., 2.78, 3
2.813, -3.536	.698, 45.	.698, 45.
2	EX:	EX:
1.39, -45.	SG: ELEMENT 5	SG: ELEMENT 8
0., 0., 0., 2.78, 3	-2.813, 3.536	0., -5.
1., -45.	2	2
1.39, 135.	1.39, 135.	1.39, 270.
0., 0., 0., 2.78, 3	0., 0., 0., 2.78, 3	0., 0., 0., 2.78, 3
.698, 45.	1., -45.	1., -45.
EX:	1.39, -45.	1.39, 90.
SG: ELEMENT 2	0., 0., 0., 2.78, 3	0., 0., 0., 2.78, 3
3.979, 0.	.698, 45.	.698, 45.
2	EX:	EX:
1.39, 0.		
0., 0., 0., 2.78, 3		
1., -45.		
1.39, 180.		
0., 0., 0., 2.78, 3		
.698, 45.		
EX:		



(a) Sum patterns

Elevation angle = 20°

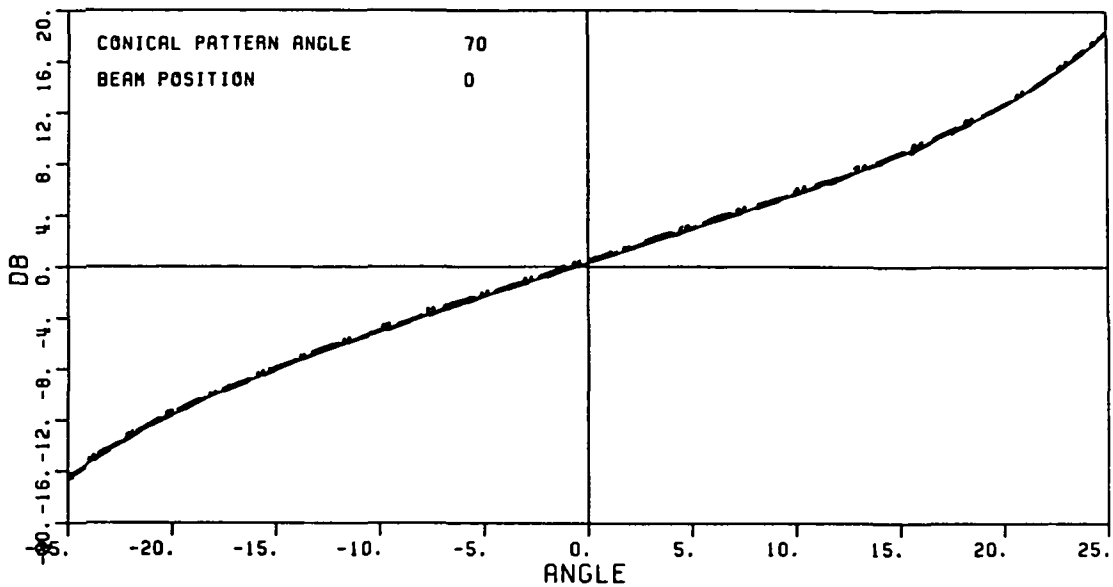
Frequency = 1.09 GHz



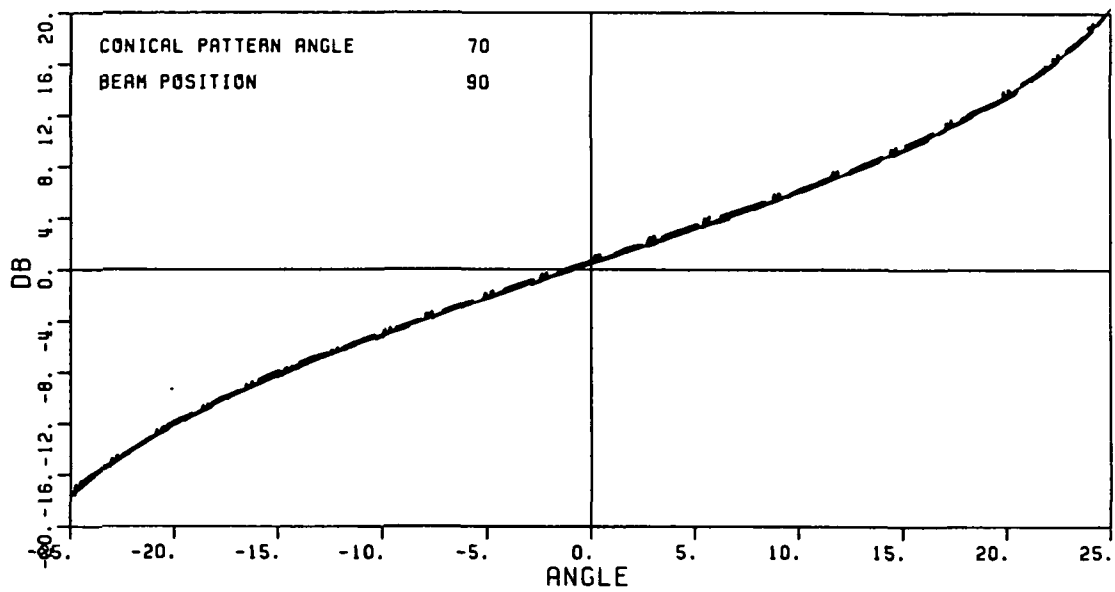
(b) Difference patterns

- Source field from a curved disc with a curvature of 72"
- Source field from a long ellipsoid
- .-.- Source field from the fuselage of a Boeing 737

Figure 5.11. Comparison of sum and difference patterns.

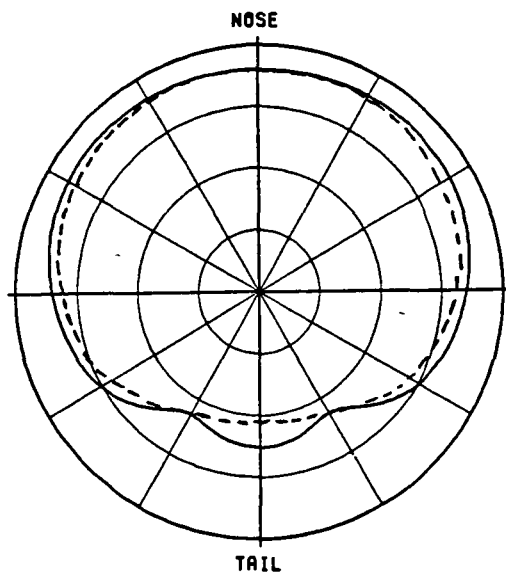


(a) Monopulse characteristic curves when beam position is 0° .

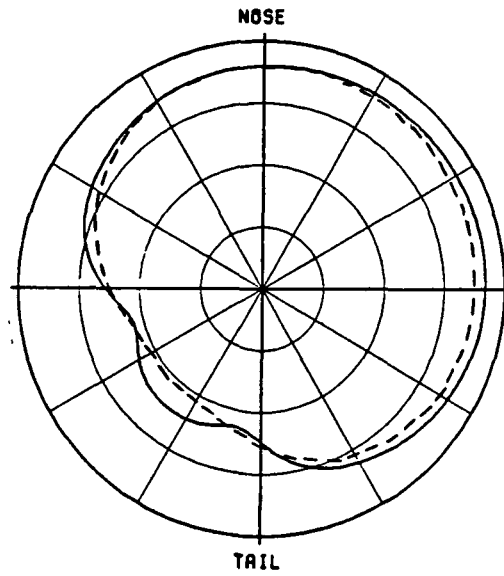


(b) Monopulse characteristic curves when beam position is 90° .

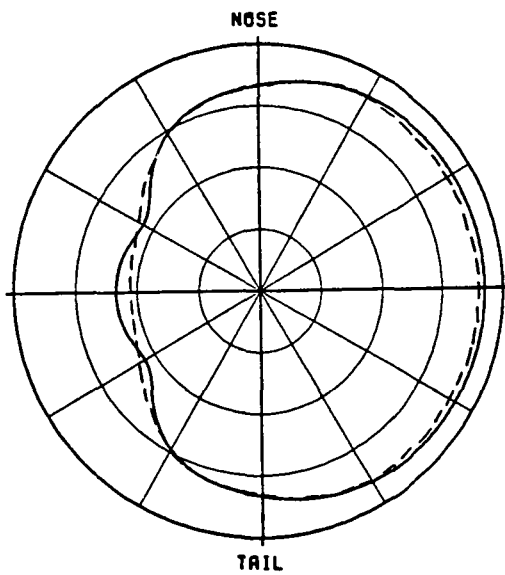
Figure 5.12. Comparison of monopulse characteristic curves referring to the three different cases in the last figure.



(a) Element #8



(b) Element #1



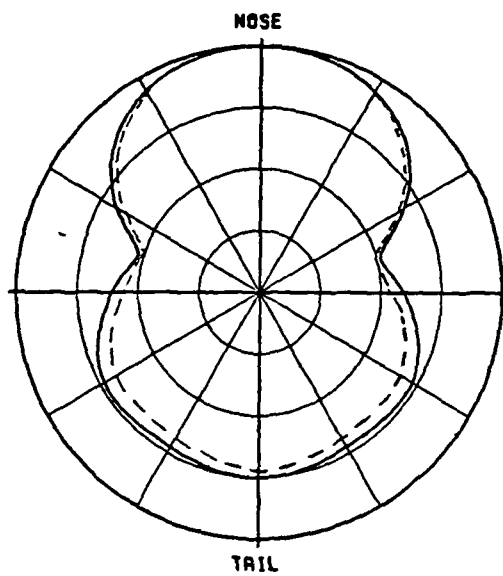
(c) Element #2

— Element pattern of
a curved disc
----- Element pattern of
the fuselage of a
Boeing 737

Frequency = 1.09 GHz

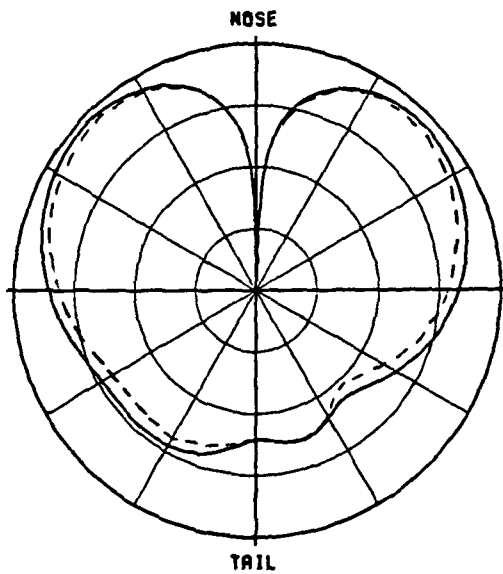
Elevation = 20°

Figure 5.13. Element patterns of a curved disc and the fuselage of a Boeing 737.



(a) Sum patterns

—— Curved disc
 ----- Fuselage of
 a Boeing 737



(b) Difference patterns

Frequency = 1.09 GHz

Elevation = 20°

Figure 5.14. Sum and difference patterns of a curved disc and the fuselage of a Boeing 737 when the beam position is 0°.

Frequency = 1.09 GHz

(a) Fuselage of a Boeing 737

(b) 2-foot radius curved disc
with a curvature of 6-feet

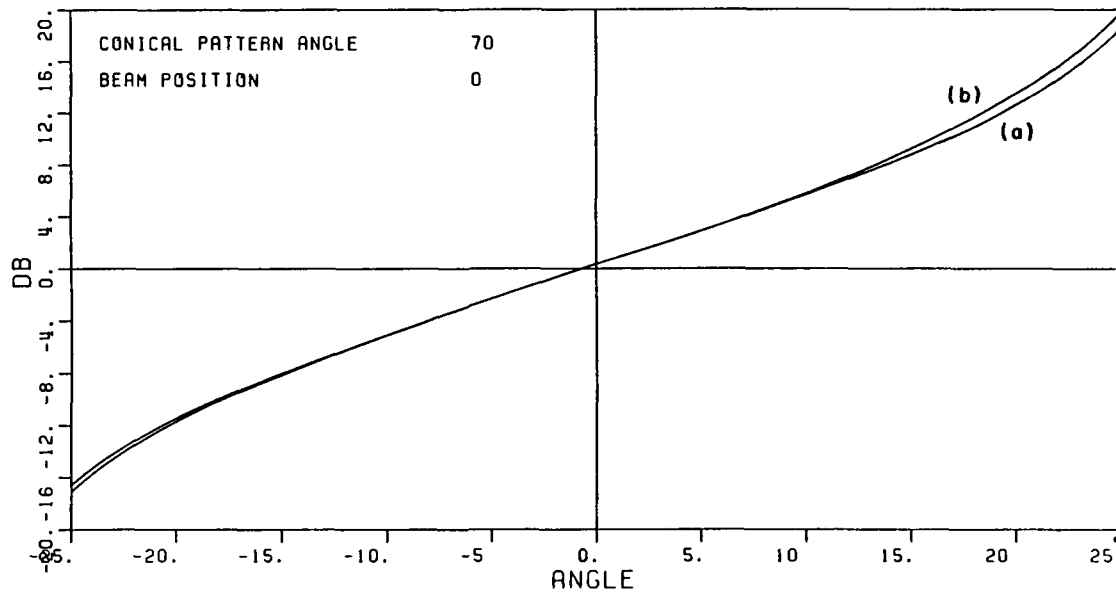
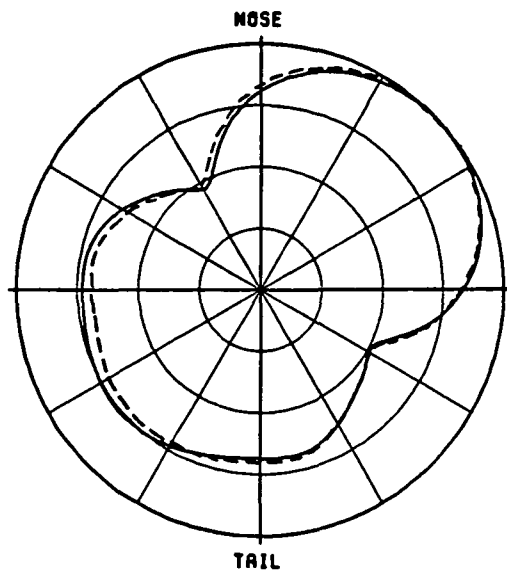
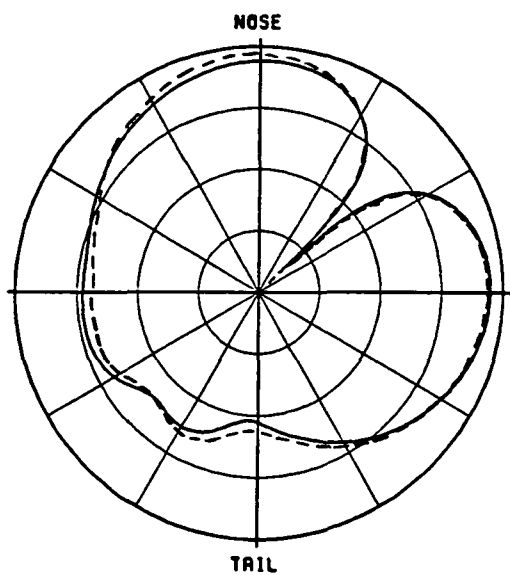


Figure 5.15. The monopulse curve corresponding to Figure 5.14.



(a) Sum patterns

—— Curved disc
 ----- Fuselage of
 a Boeing 737



(b) Difference patterns

Frequency = 1.09 GHz

Elevation = 20°

Figure 5.16. Sum and difference patterns of a curved disc and the fuselage of a Boeing 737 when the beam position is 45°.

Frequency = 1.09 GHz

- (a) Fuselage of a Boeing 737
- (b) 2-foot radius curved disc
with a curvature of 6-feet

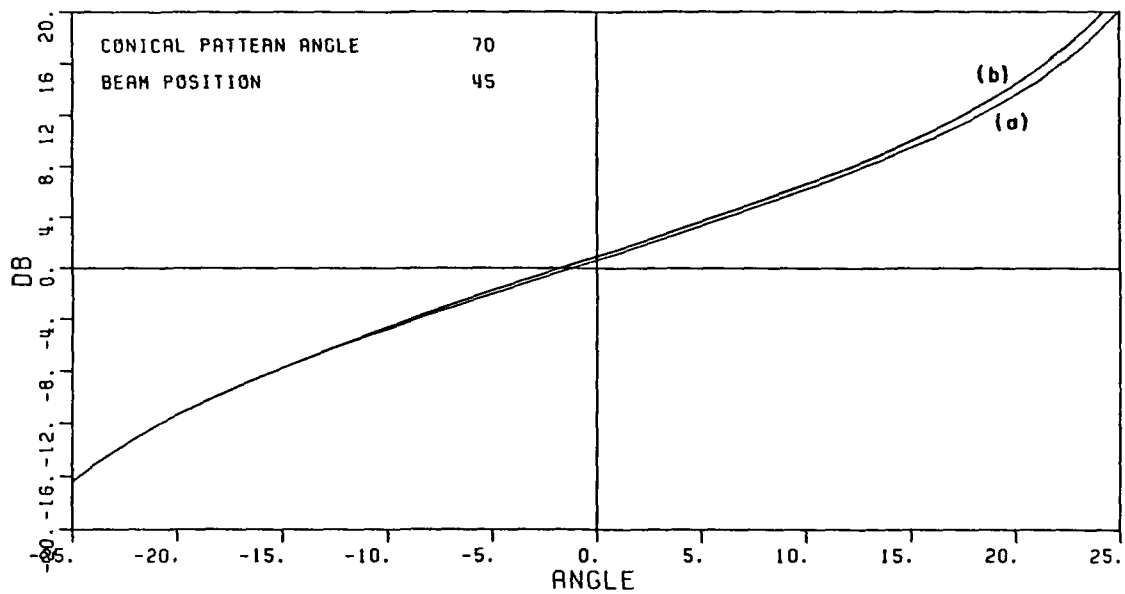
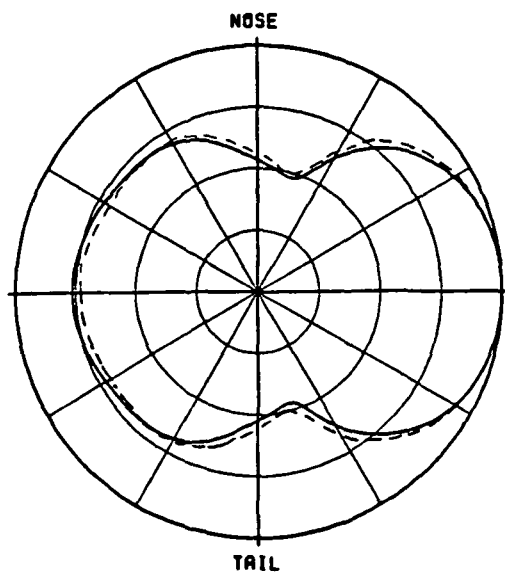
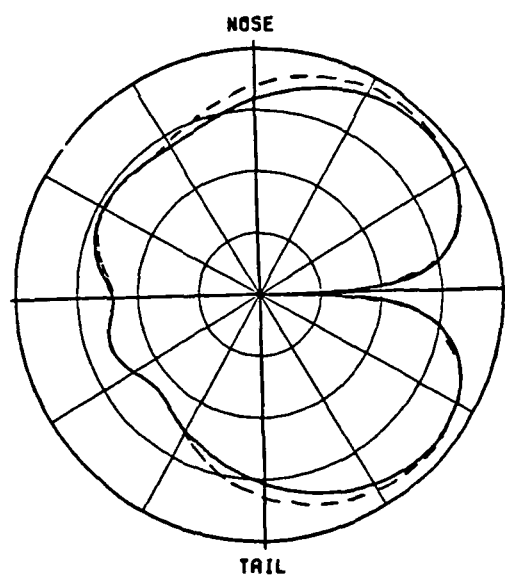


Figure 5.17. The monopulse curve corresponding to Figure 5.16.



(a) Sum patterns

—— Curved disc
 ---- Fuselage of
 a Boeing 737



(b) Difference patterns

Frequency = 1.09 GHz
 Elevation = 20°

Figure 5.18. Sum and difference patterns of a curved disc and the fuselage of a Boeing 737 when the beam position is 90°.

Frequency = 1.09 GHz

(a) Fuselage of a Boeing 737

(b) 2-foot radius curved disc
with a curvature of 6-feet

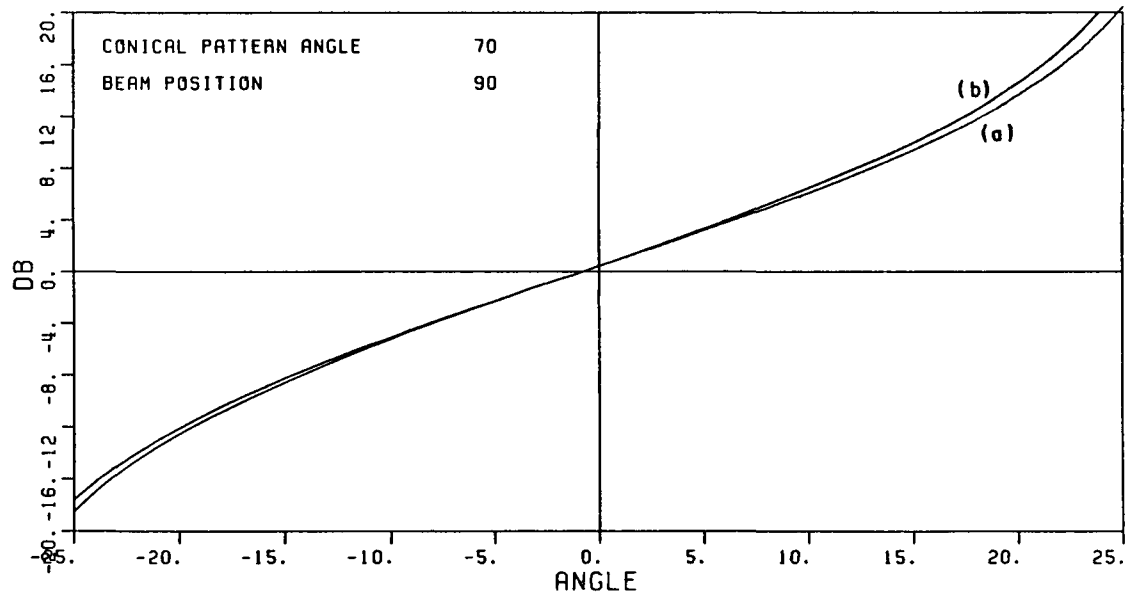
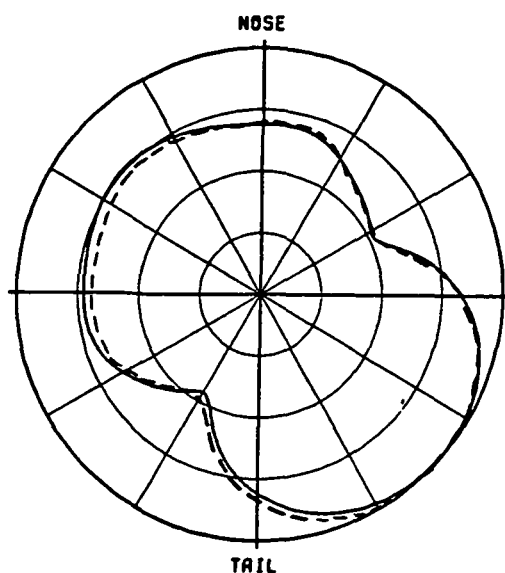
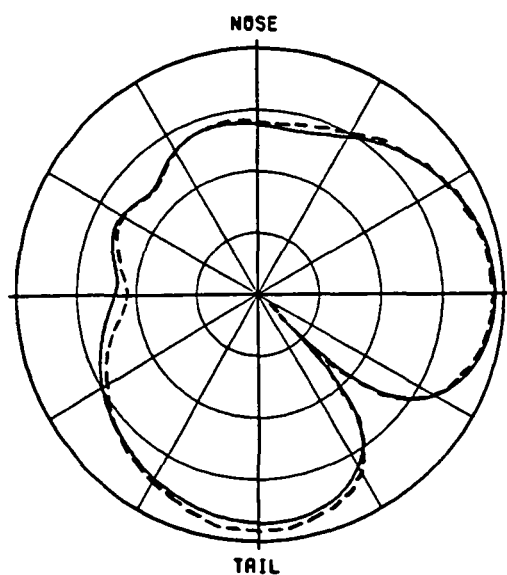


Figure 5.19. The monopulse curve corresponding to Figure 5.18.



(a) Sum patterns

—— Curved disc
 ----- Fuselage of
 a Boeing 737



(b) Difference patterns

Frequency = 1.09 GHz

Elevation = 20°

Figure 5.20. Sum and difference patterns of a curved disc and the fuselage of a Boeing 737 when the beam position is 135°.

Frequency = 1.09 GHz

- (a) Fuselage of a Boeing 737
- (b) 2-foot radius curved disc
with a curvature of 6-feet

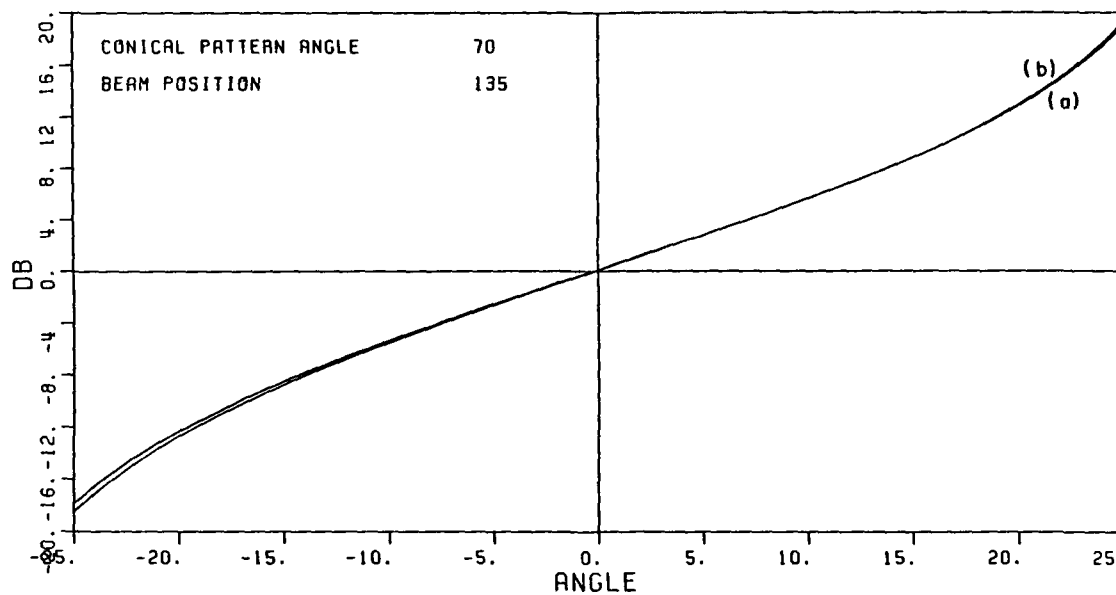
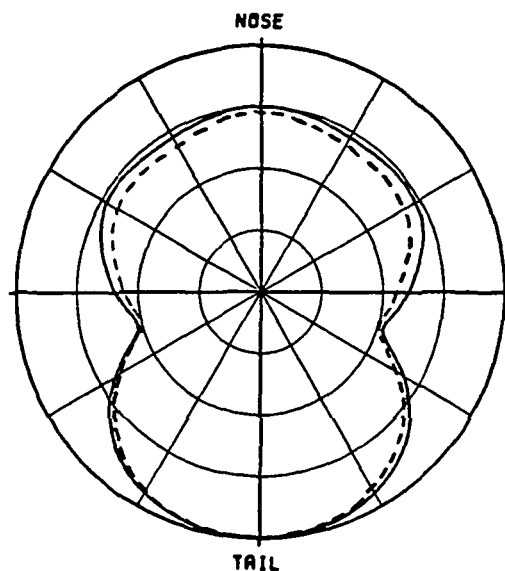
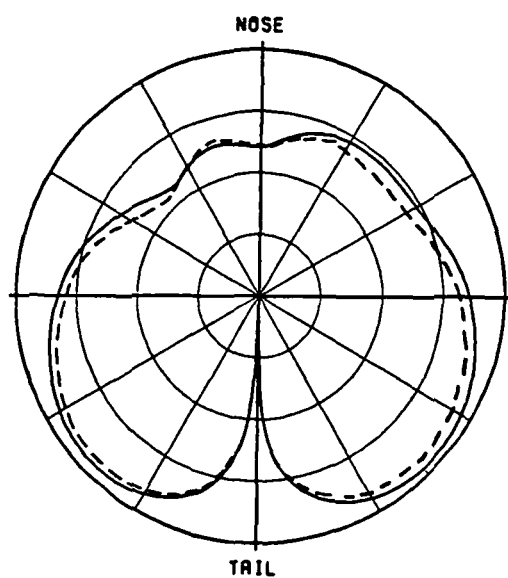


Figure 5.21. The monopulse curve corresponding to Figure 5.20.



(a) Sum patterns

—— Curved disc
 ----- Fuselage of
 a Boeing 737



(b) Difference patterns

Frequency = 1.09 GHz

Elevation = 20°

Figure 5.22. Sum and difference patterns of a curved disc and the fuselage of a Boeing 737 when the beam position is 180°.

Frequency = 1.09 GHz

- (a) Fuselage of a Boeing 737
- (b) 2-foot radius curved disc
with a curvature of 6-feet

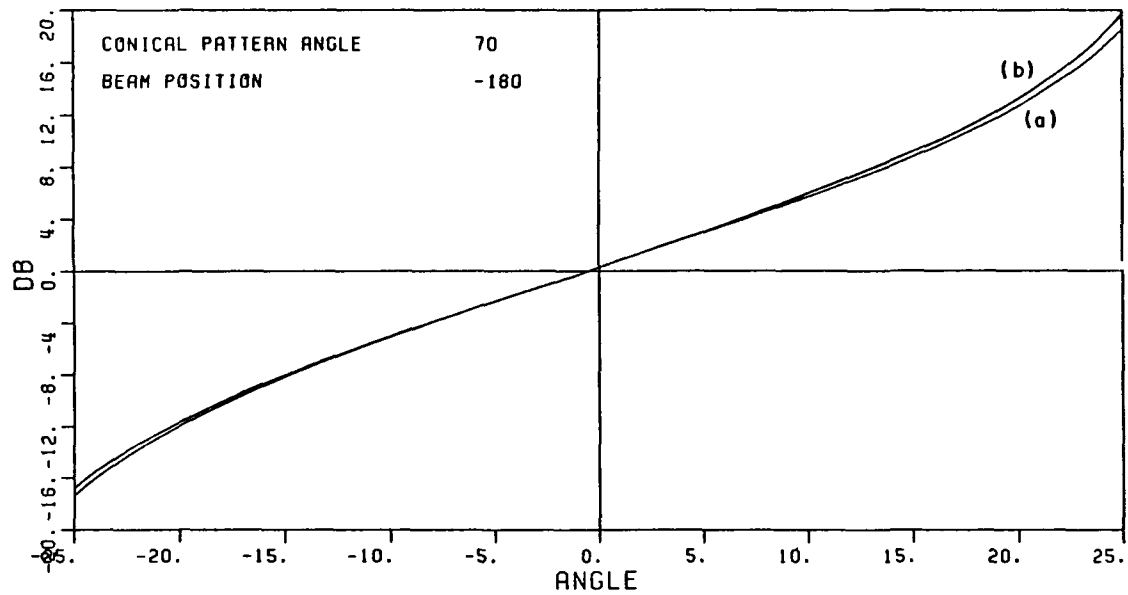
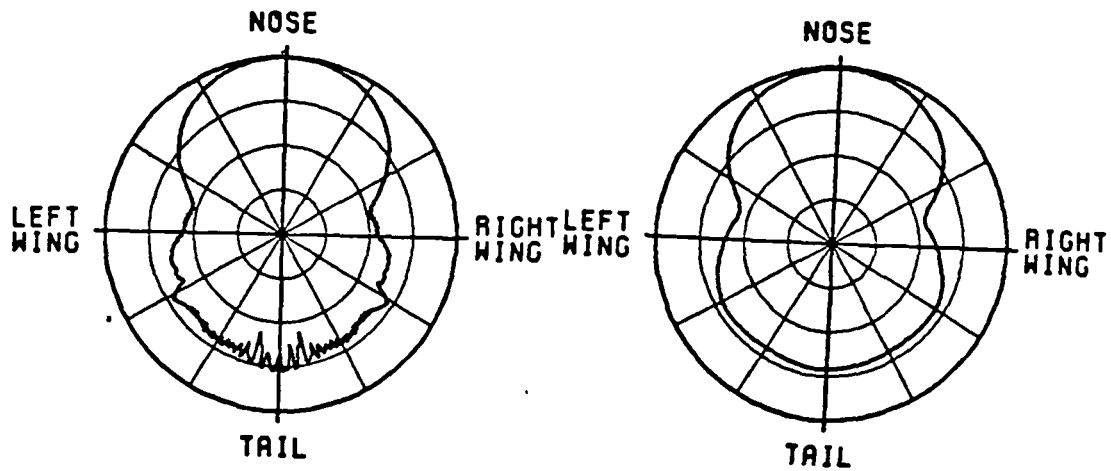


Figure 5.23. The monopulse curve corresponding to Figure 5.22.

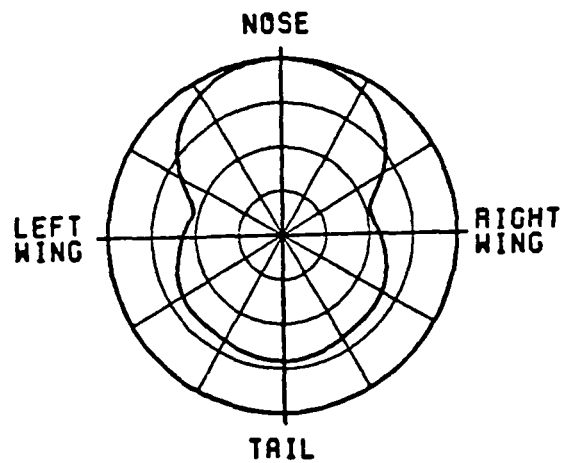
Frequency = 1.06 GHz

(SCALE: EACH DIVISION=1008)



(a) a Boeing 737

(b) a curved ground plane

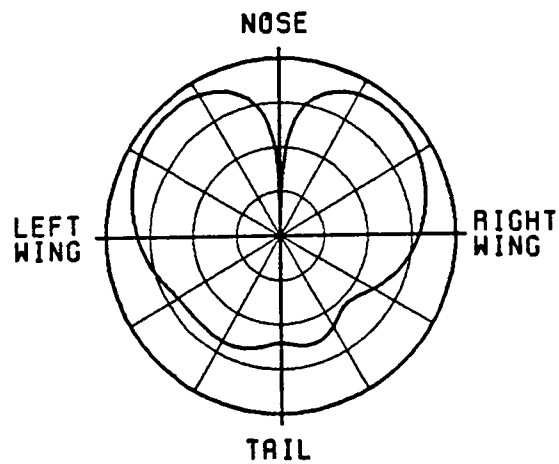
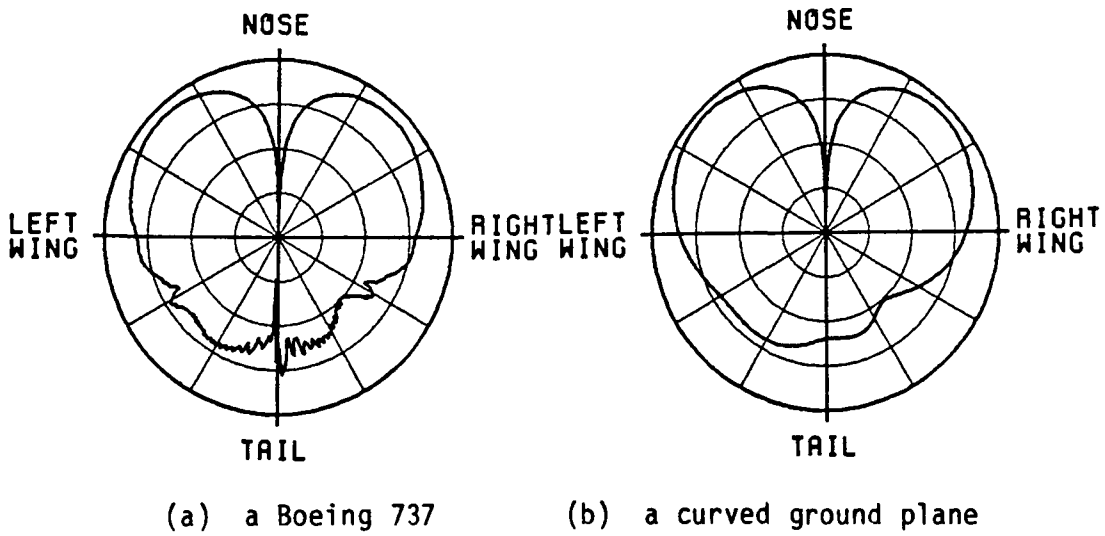


(c) the fuselage of a Boeing 737

Figure 5.24. Sum patterns of a Boeing 737, a curved ground plane and the fuselage of a Boeing 737.

Frequency = 1.06 GHz

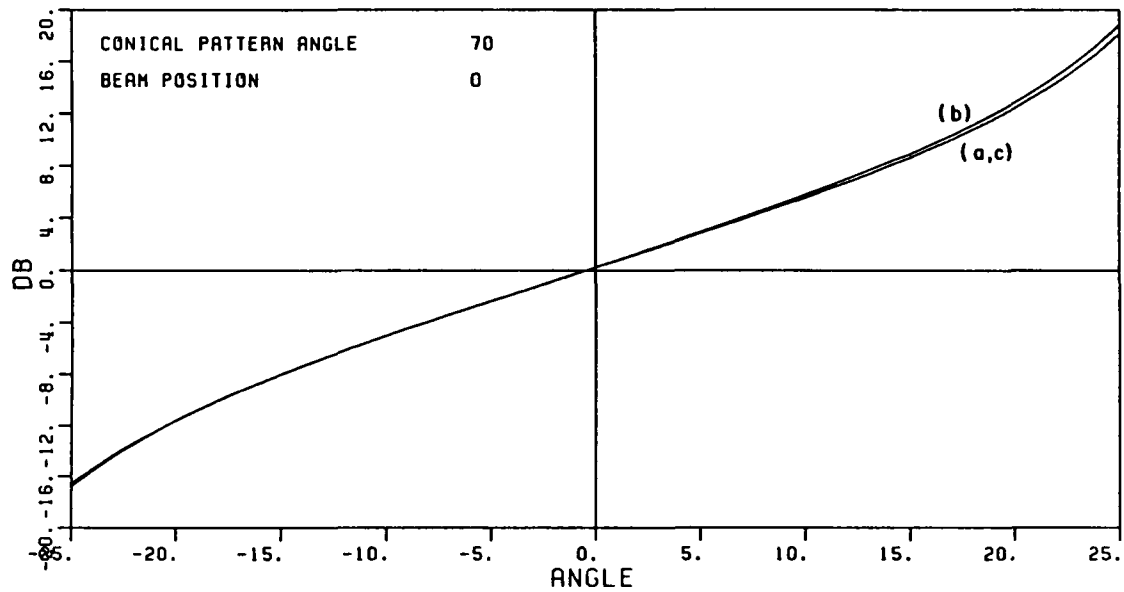
(SCALE: EACH DIVISION=10DB)



(c) the fuselage of a Boeing 737

Figure 5.25. Difference patterns of a Boeing 737, a curved ground plane and the fuselage of a Boeing 737.

Frequency = 1.06 GHz



- (a) Boeing 737
- (b) 2-foot radius curved disc
with a curvature of 6-feet
- (c) Fuselage of a Boeing 737

Figure 5.26. The corresponding monopulse curves.

Frequency = 1.06 GHz
 (SCALE: EACH DIVISION=10DB)

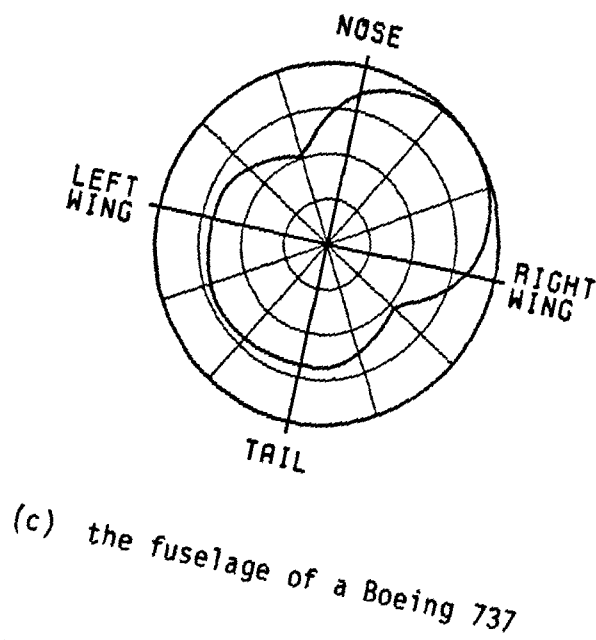
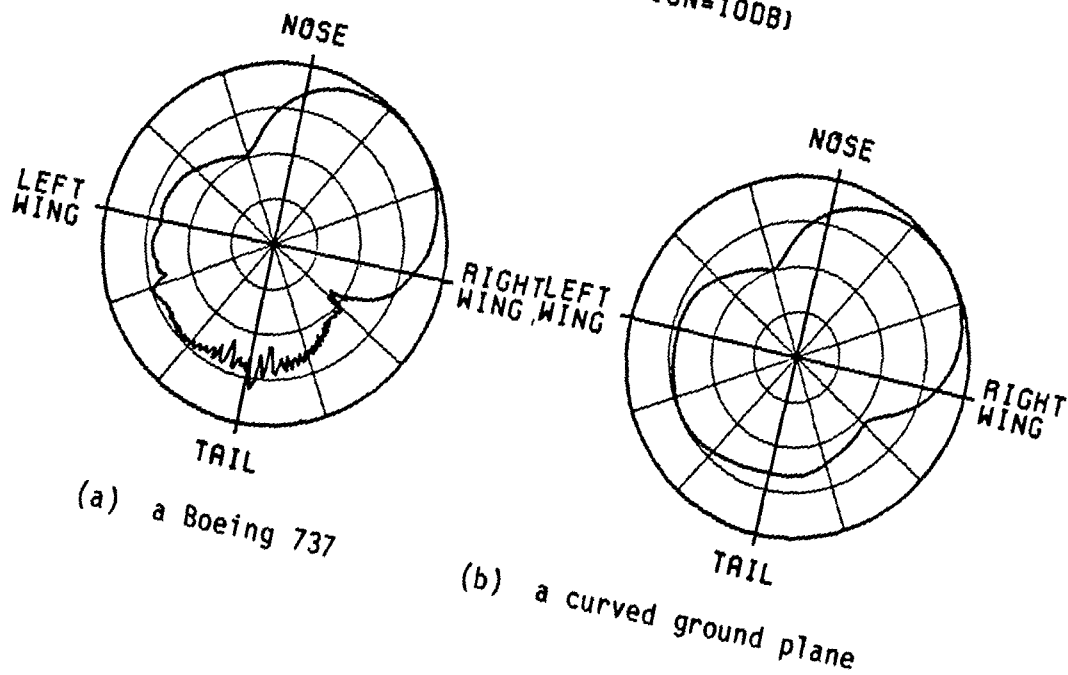


Figure 5.27. Sum patterns of a Boeing 737, a curved ground plane and the fuselage of a Boeing 737.

Frequency = 1.06 GHz

(SCALE: EACH DIVISION=100DB)

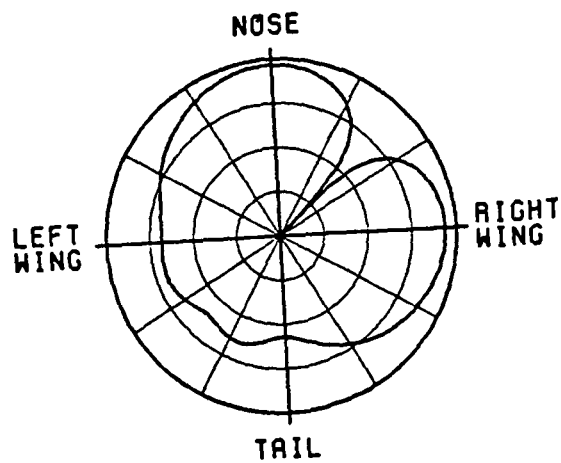
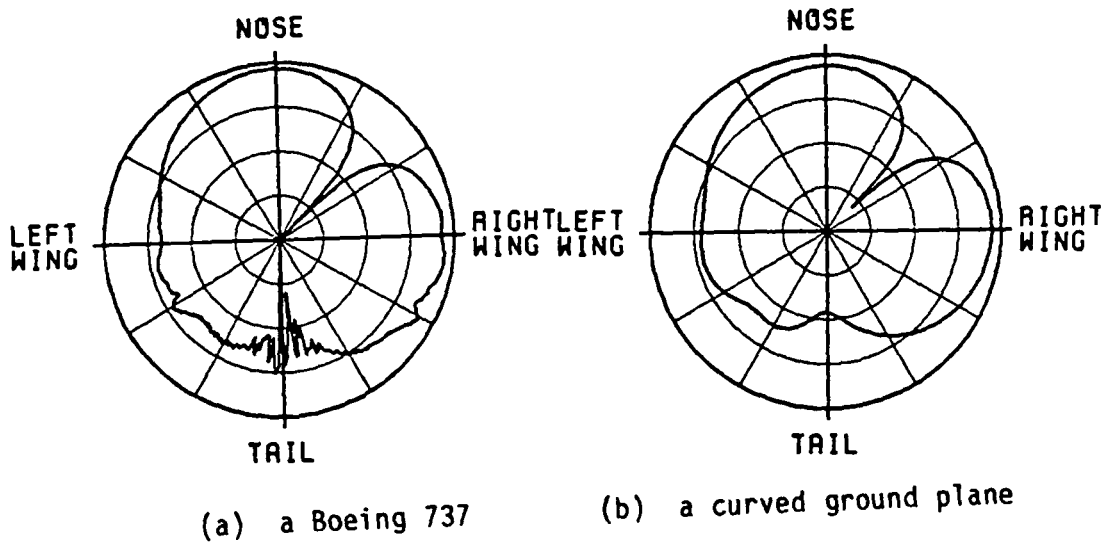
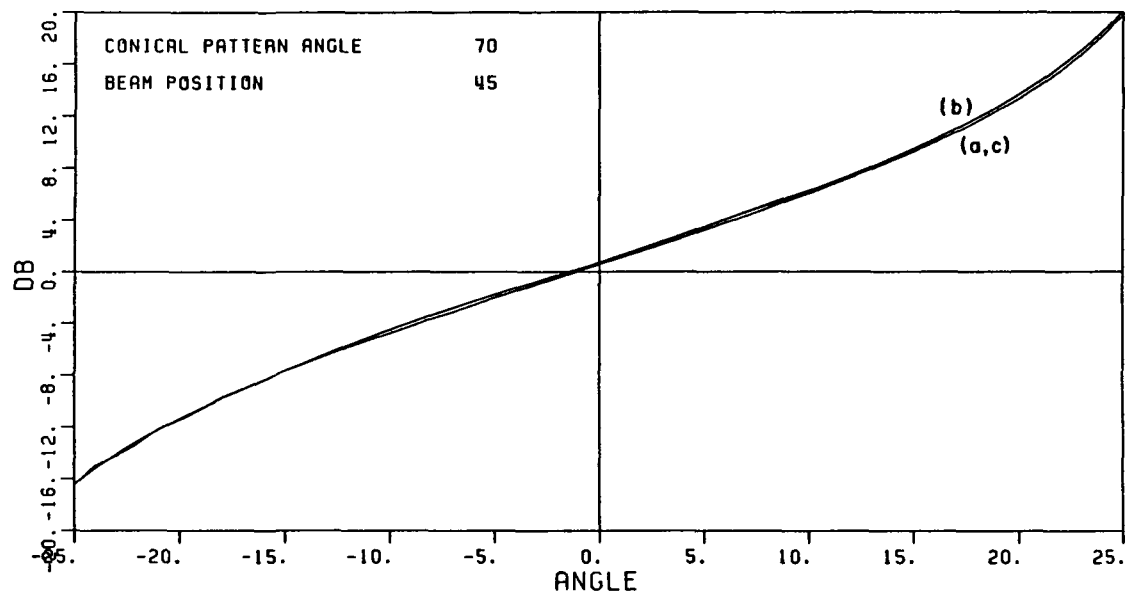


Figure 5.28. Difference patterns of a Boeing 737, a curved ground plane and the fuselage of a Boeing 737.

Frequency = 1.06 GHz



- (a) Boeing 737
- (b) 2-foot radius curved disc
with a curvature of 6-feet
- (c) Fuselage of a Boeing 737

Figure 5.29. The corresponding monopulse curves.

Frequency = 1.06 GHz

(SCALE: EACH DIVISION=100dB)

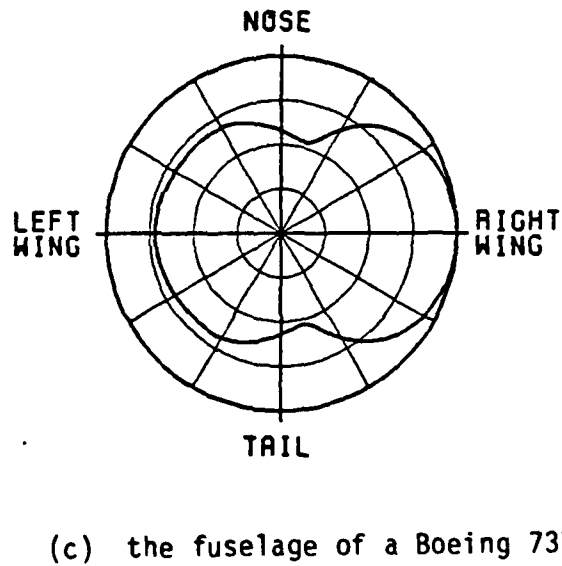
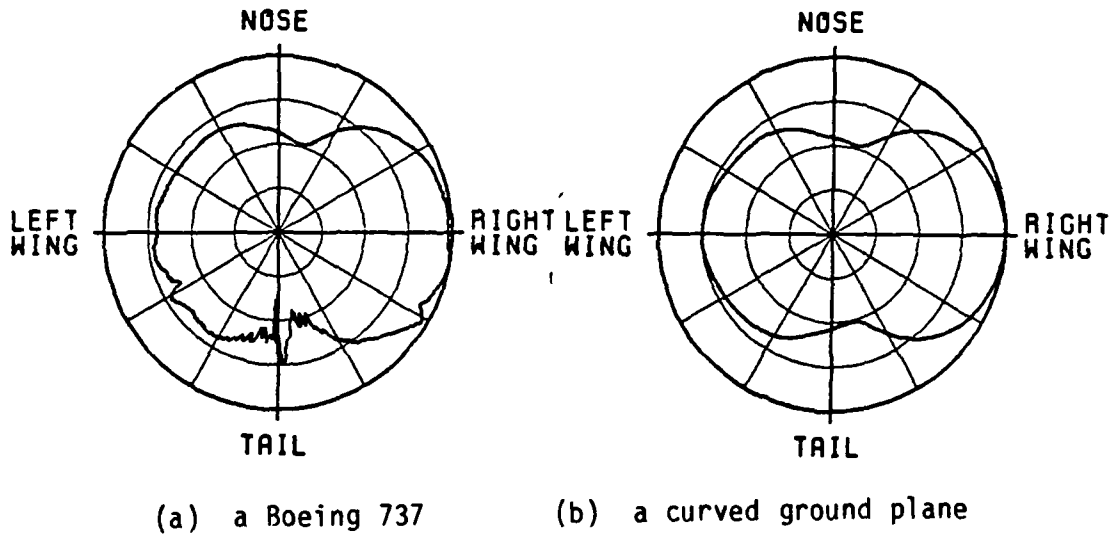
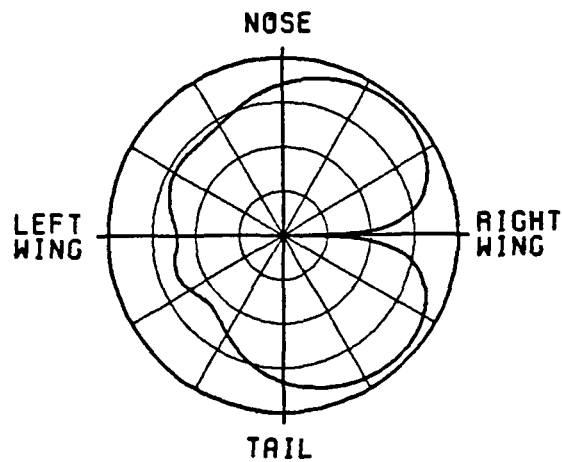
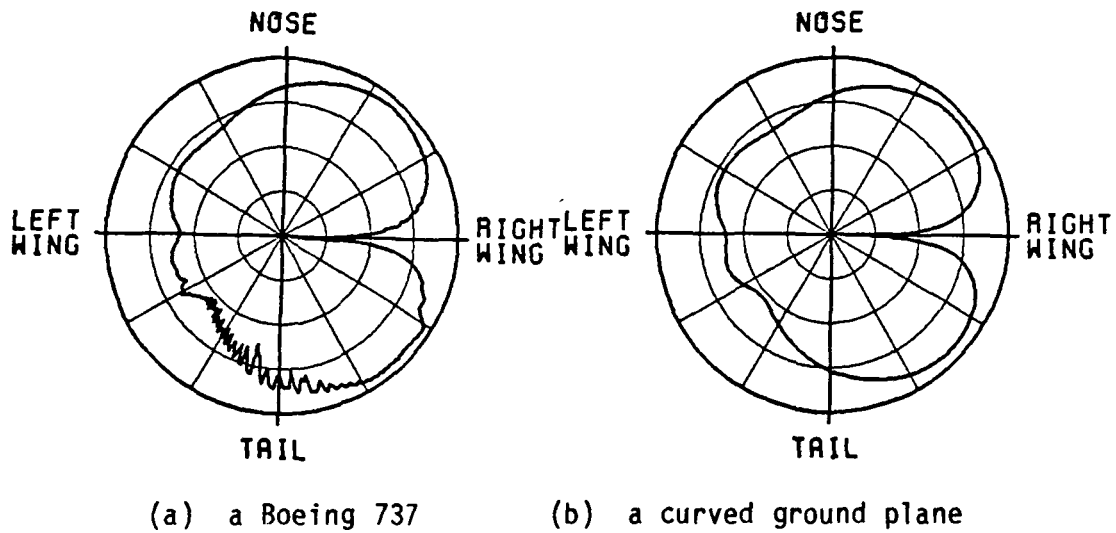


Figure 5.30. Sum patterns of a Boeing 737, a curved ground plane and the fuselage of a Boeing 737.

Frequency = 1.06 GHz

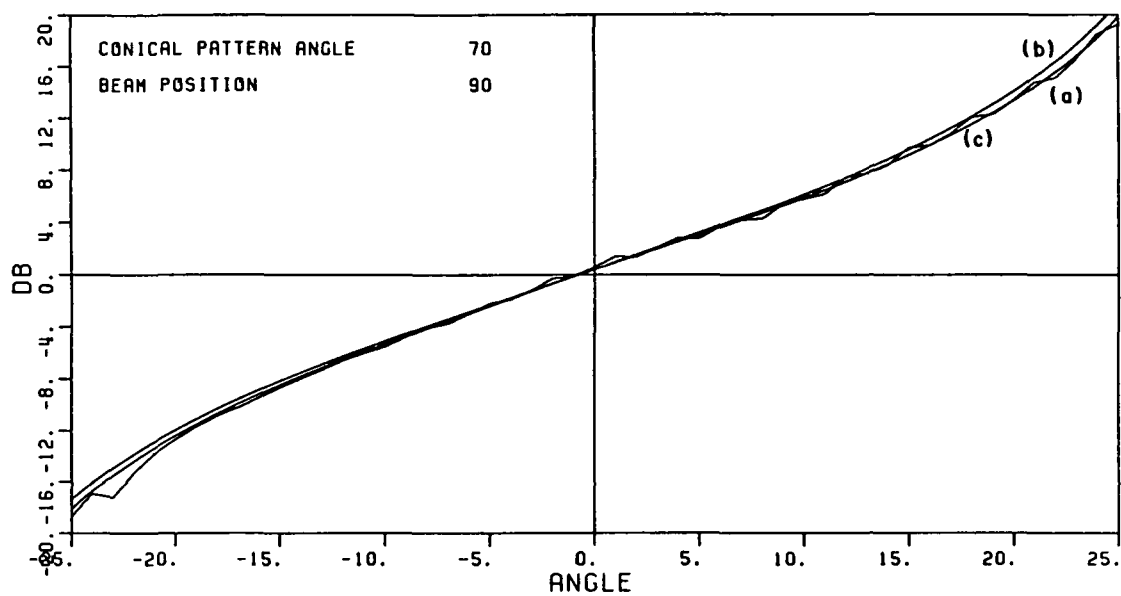
(SCALE: EACH DIVISION=100B)



(c) the fuselage of a Boeing 737

Figure 5.31. Difference patterns of a Boeing 737, a curved ground plane and the fuselage of a Boeing 737.

Frequency = 1.06 GHz

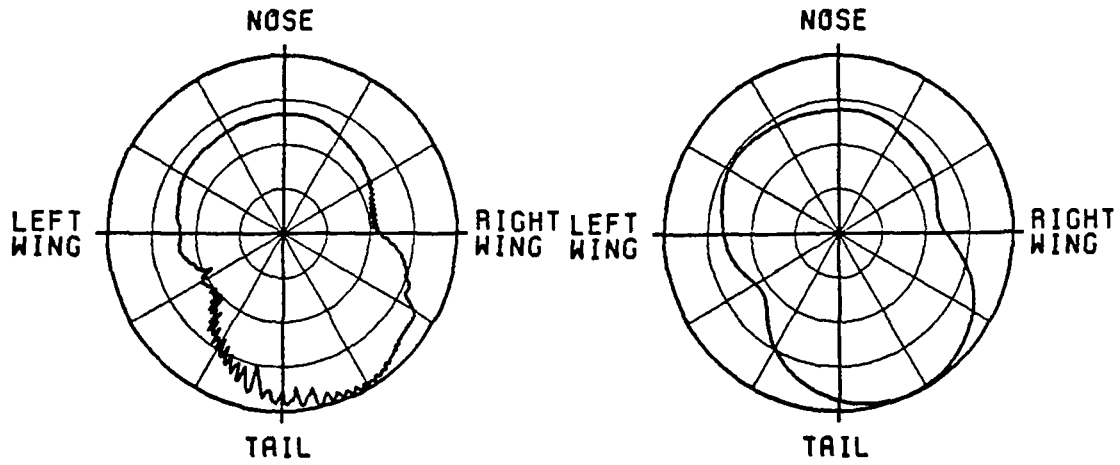


- (a) Boeing 737
- (b) 2-foot radius curved disc
with a curvature of 6-feet
- (c) Fuselage of a Boeing 737

Figure 5.32. The corresponding monopulse curves.

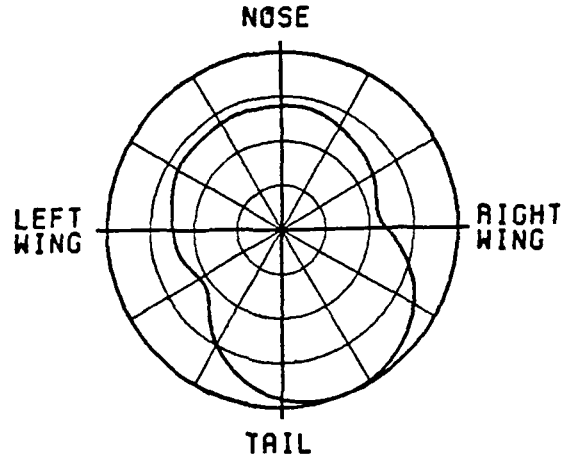
Frequency = 1.06 GHz

(SCALE: EACH DIVISION=10DB)



(a) a Boeing 737

(b) a curved ground plane

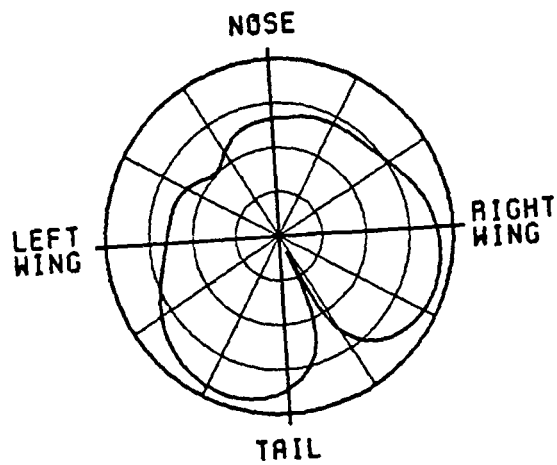
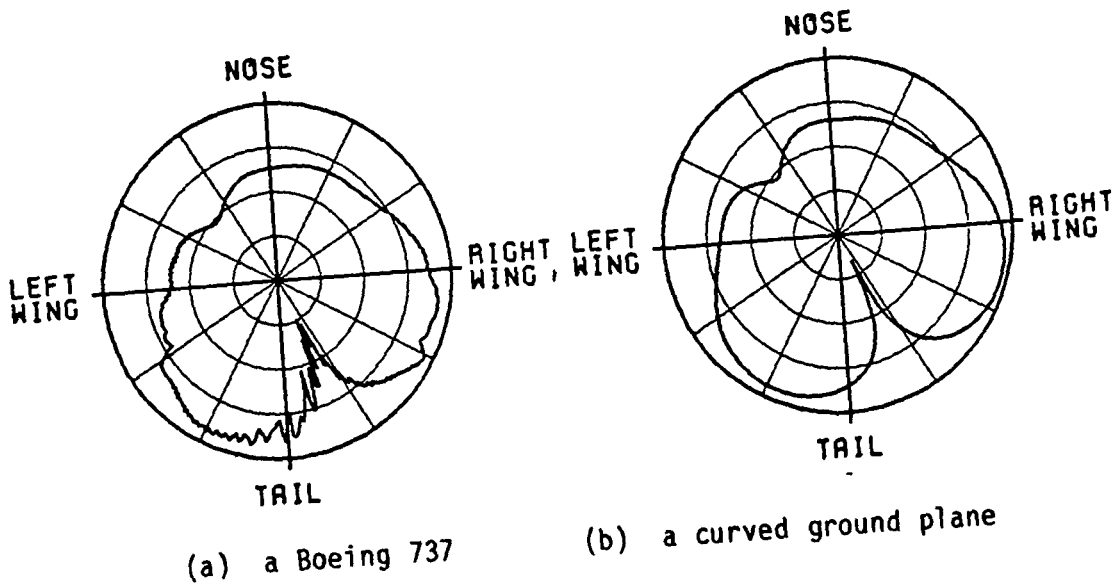


(c) the fuselage of a Boeing 737

Figure 5.33. Sum patterns of a Boeing 737, a curved ground plane and the fuselage of a Boeing 737.

Frequency = 1.06 GHz

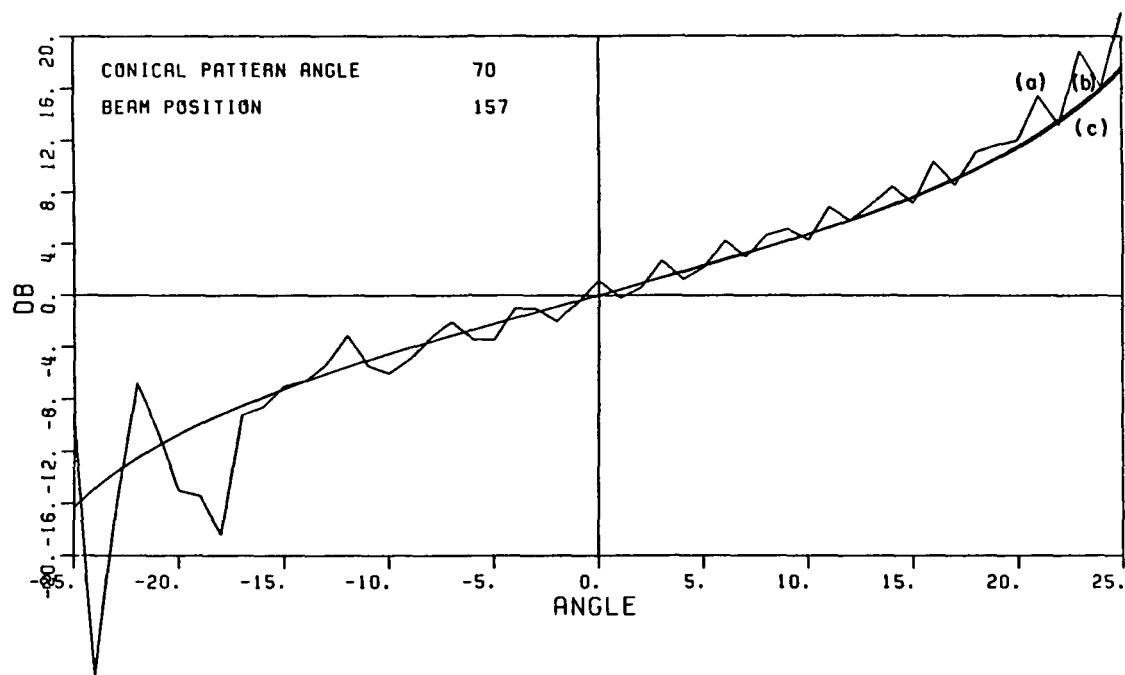
(SCALE: EACH DIVISION=100dB)



(c) the fuselage of a Boeing 737

Figure 5.34. Difference patterns of a Boeing 737, a curved ground plane and the fuselage of a Boeing 737.

Frequency = 1.06 GHz



- (a) A Boeing 737
- (b) 2-foot radius curved disc
with a curvature of 6-feet
- (c) Fuselage of a Boeing 737

Figure 5.35. The corresponding monopulse curves.

Frequency = 1.06 GHz

(SCALE: EACH DIVISION=10DB)

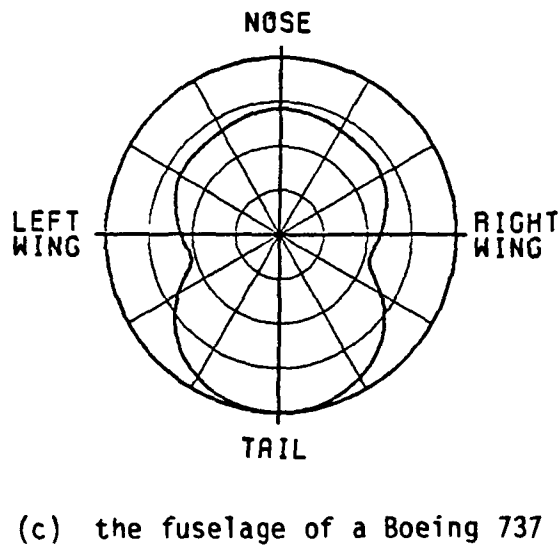
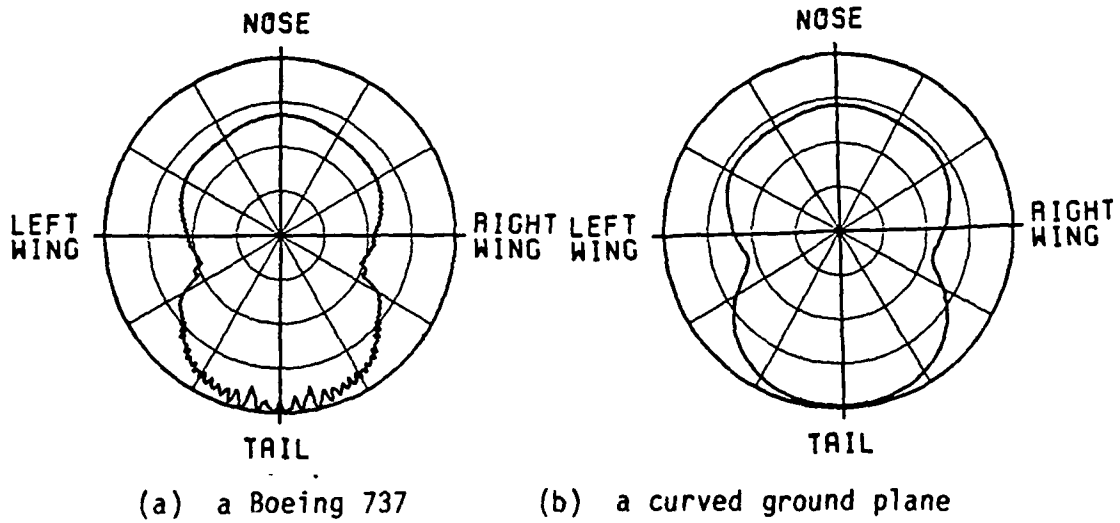
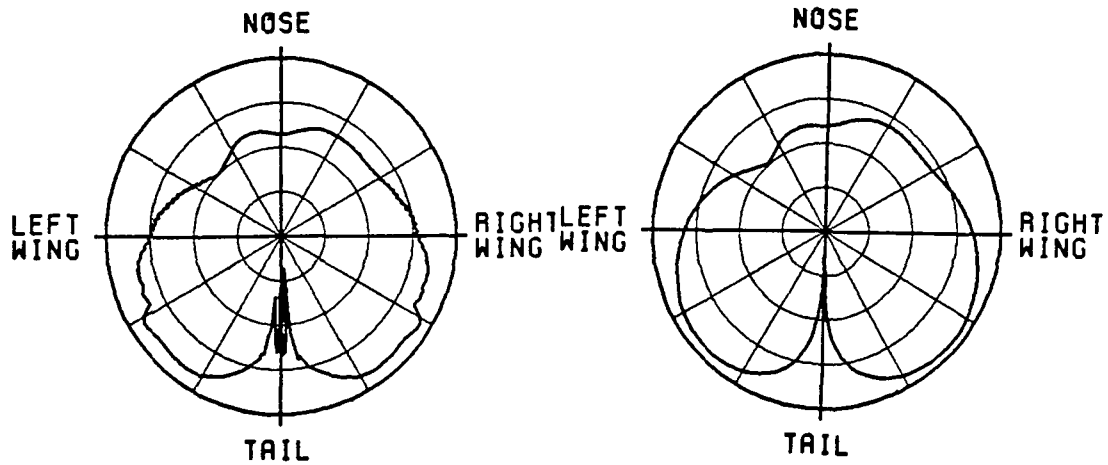


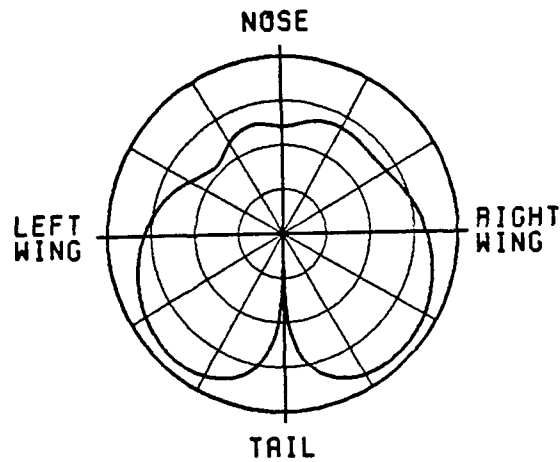
Figure 5.36. Sum patterns of a Boeing 737, a curved ground plane and the fuselage of a Boeing 737.

Frequency = 1.06 GHz



(a) a Boeing 737

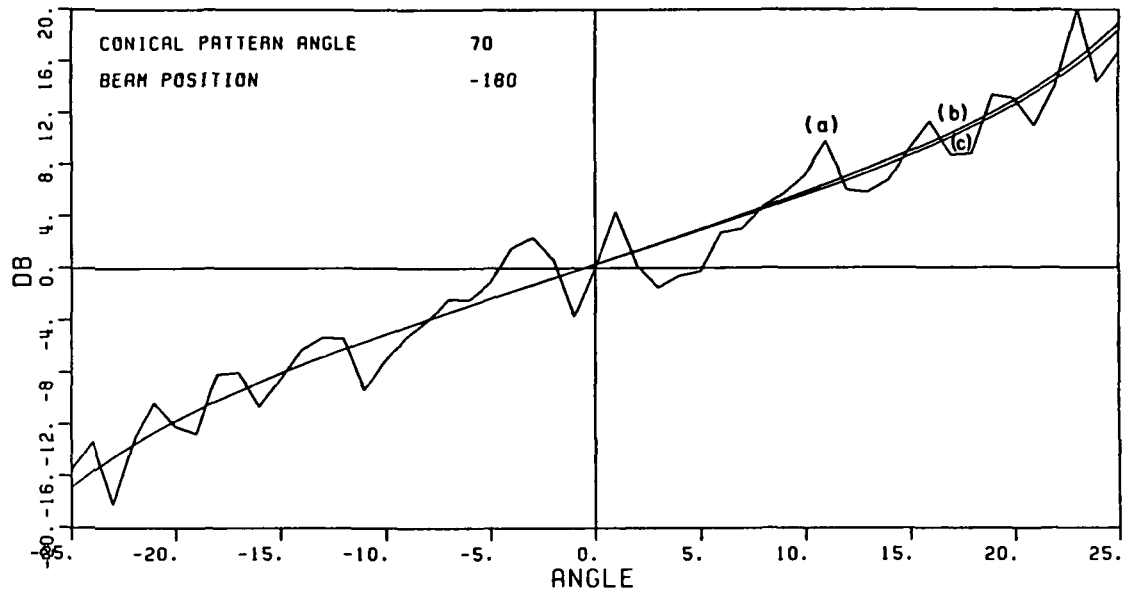
(b) a curved ground plane



(c) the fuselage of a Boeing 737

Figure 5.37. Difference patterns of a Boeing 737, a curved ground plane and the fuselage of a Boeing 737.

Frequency = 1.06 GHz



- (a) Boeing 737
- (b) 2-foot radius curved disc
with a curvature of 6-feet
- (c) Fuselage of a Boeing 737

Figure 5.38. The corresponding monopulse curves.

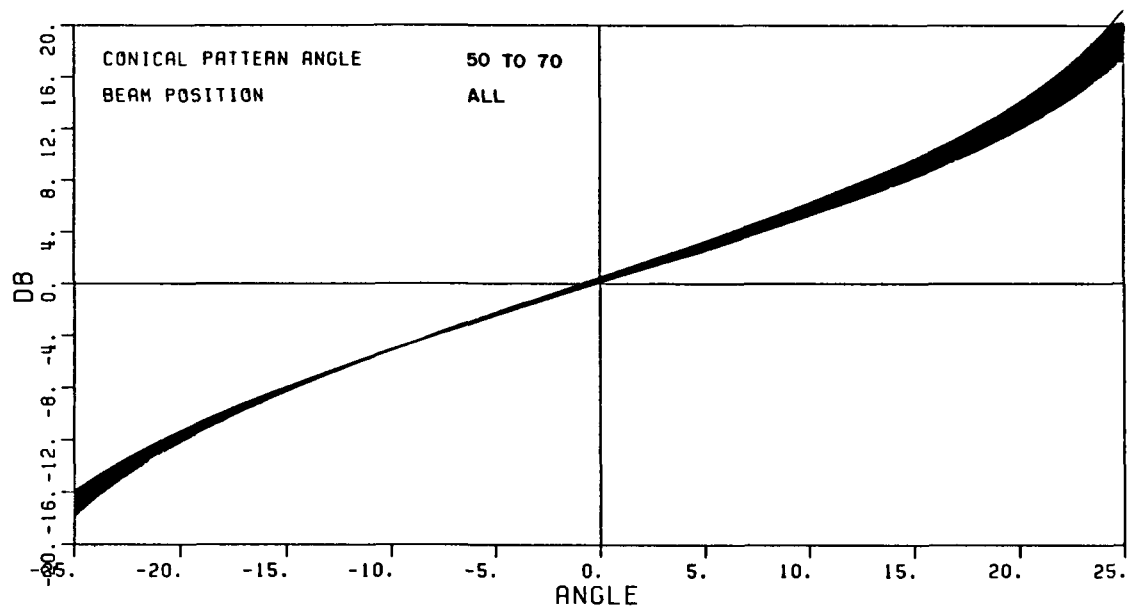


Figure 5.39. All the monopulse curves of a flat ground plane when the elevation angle varies from 20° to 40° and the beam position changes.

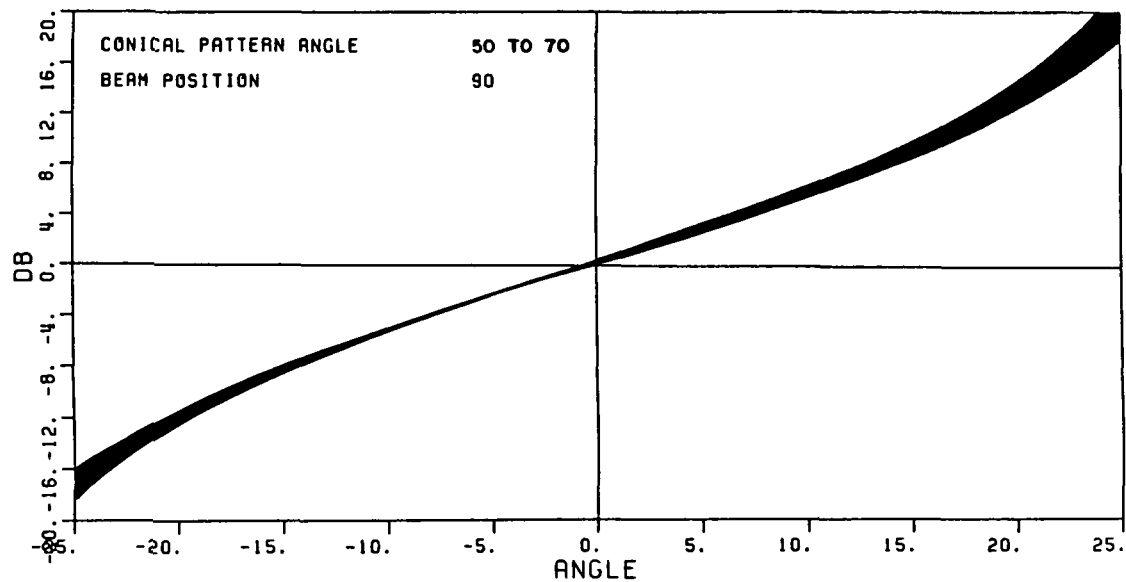


Figure 5.40. The monopulse curves of a curved ground plane with a curvature of 6-feet when the beam position is 90° and the elevation angle varies from 20° to 40° .

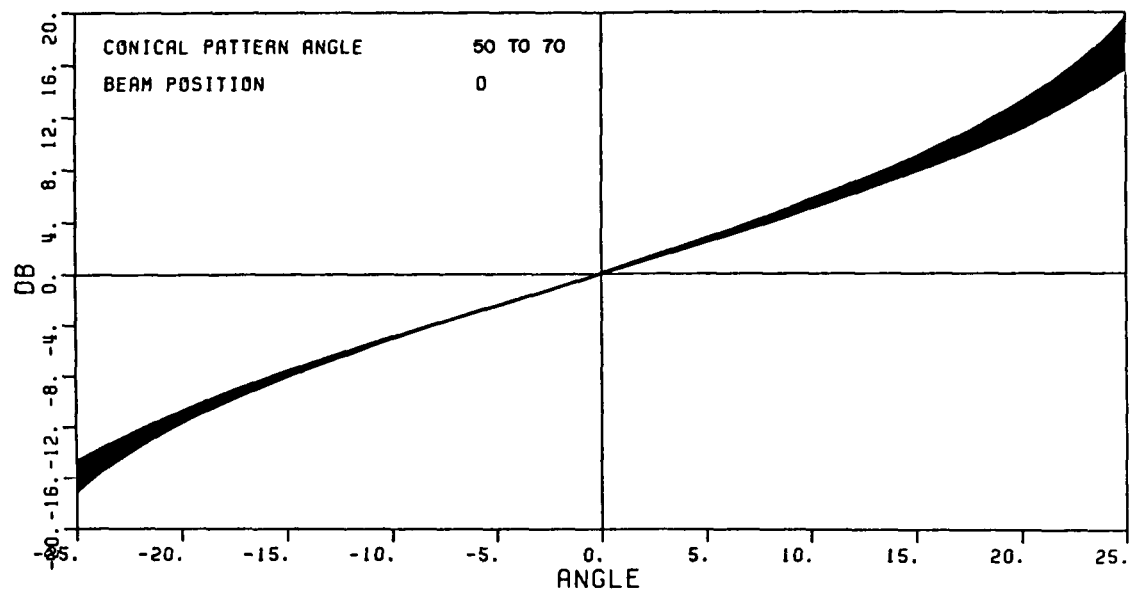


Figure 5.41. The monopulse curves of a curved ground plane with a curvature of 6-feet when the beam position is 0° and the elevation angle varies from 20° to 40° .

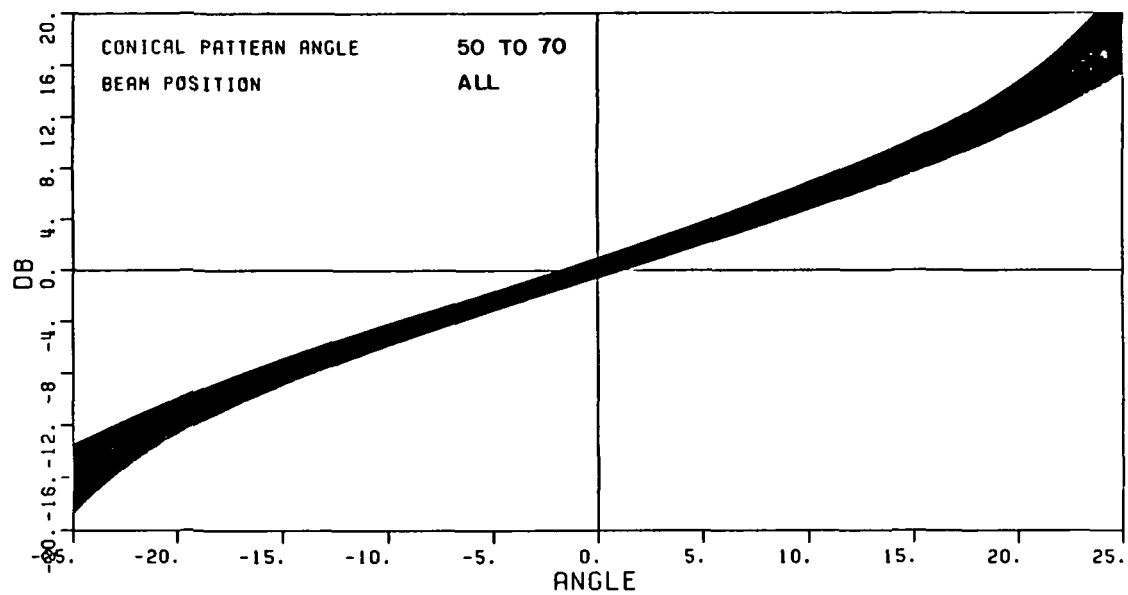


Figure 5.42. The monopulse curves of a curved ground plane with a curvature of 6-feet when the elevation angle varies from 20° to 40° and the beam position changes.

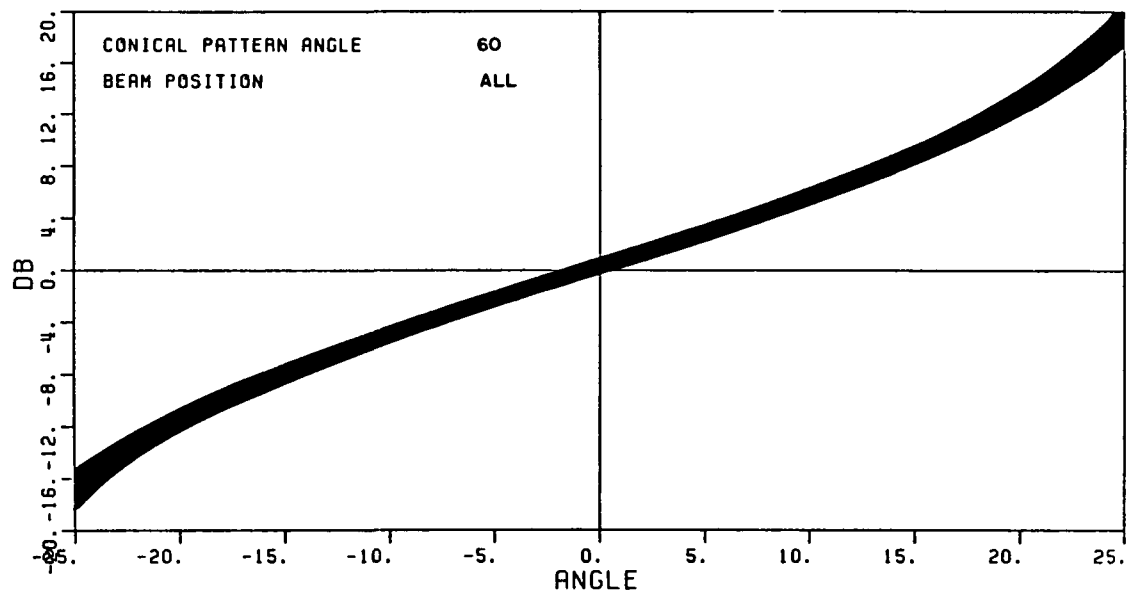


Figure 5.43. The monopulse curves of a curved ground plane with a curvature of 6-feet when the elevation angle is 30° and the beam position changes.

CHAPTER VI

CONCLUSIONS

A curved ground plane can be used to model the fuselage of an aircraft with a slight error in the monopulse characteristic curves. This error is small compared to the error caused by the appendages found on an aircraft. This is particularly true when the beam position is near the tail of an aircraft where the monopulse characteristic results are severely distorted by the vertical stabilizer. To reduce such an undesirable scattering effect, Reference [20] points out that one solution is to move the TCAS II location as far from the vertical stabilizer as possible.

Some other observations made in the previous chapter include the followings:

- (a) For a flat ground plane, the monopulse characteristic curves do not depend on beam positions due to the symmetry of the structure.
- (b) For a curved ground plane, the surface curvature affects the monopulse characteristic curves such that they vary significantly with beam position. This verifies the need for a lookup table for each azimuth beam position.
- (c) For a fixed beam position, the monopulse characteristic curves do not change significantly with elevation angle provided that the azimuth look angle for each beam is kept small; i.e., less than $\pm 25^\circ$.

Based on the above observations, it can be concluded that no matter where the TCAS II is placed on the fuselage, variations in the monopulse characteristic curves due to elevation angle changes are rather weak in terms of the fuselage curvature, but they can be dependent on the aircraft structure such as the vertical stabilizer. The choice of a flatter surface does not seem to improve the above condition. However, since major errors come from the scattering of the tail, the best location of the TCAS II is still to move it as far from the vertical stabilizer as possible as suggested by Grandchamp [20].

As a last remark, the curved ground plane can be considered as a good simulation model for the fuselage of an aircraft but may not be good enough to model a whole aircraft. Finally, it should be noted that all the conclusions made above are only valid when the elevation angles are within the range of the curved ground plane solution. Thus, measured results are needed to verify these conclusions.

REFERENCES

- [1] K. Julian, "Preventing Midair Collisions", High Technology, July, 1985, pp. 48-53.
- [2] D.E.N. Davies, "Circular Arrays", The Handbook of Antenna Design, Vol.2, A.W. Rudge, K. Milne, Ed., London, Peter Peregrinus Ltd., pp. 298-329, 1983.
- [3] A.I. Sinsky, "Circular Array Design Equations", Special Technical Report 119, Advanced Development Group, Bendix Communications Division, January 1985.
- [4] W.R. Lepage, C.S. Roys, and S. Sealy, "Radiation from Circular Current Sheets", Proc. IRE, vol. 38, pp. 1069-1072, September 1950.
- [5] R.S. Elliot, "An Approximation to Chebyshev Distributions," IEEE Trans. Antennas Propagat., AP-11(1963), pp. 707-9.
- [6] J.B. Keller, "Geometrical Theory of Diffraction", J. Opt. Soc. Am., Vol. 52, No. 2, pp. 116-130, 1962.
- [7] Short Course Notes on "The Modern Geometrical Theory of Diffraction", Vols. 1, 2 and 3, The Ohio State University, Department of Electrical Engineering, 1985.
- [8] R.C. Hansen, ed., Geometrical Theory of Diffraction, IEEE Press, 1981.
- [9] J.J. Kim, "Simulation and Analysis of Airborne Antenna Radiation Patterns", Ph.D. Dissertation, The Ohio State University, Department of Electrical Engineering, 1984.
- [10] P.H. Pathak, N. Wang, W.D. Burnside, and R.G. Kouyoumjian, "A Uniform GTD Solution for the Radiation from Sources on a Convex Surface", IEEE Trans. on Antennas and Prop., Vol. AP-29, No. 4, pp. 609-622, July 1981.
- [11] W.D. Burnside, N. Wang, and E.L. Pelton, "Near-Field Pattern Computations for Airborne Antenna", June 1978, Report 784685-4, prepared under Contract N00019-77-C-0299, department of Navy, Naval Air Systems Command.

- [12] N. Wang, "Near-Field Solutions for Antennas on Elliptic Cyclinder", Report 784685-1, July 1977, The Ohio State University, Department of Electrical Engineering, prepared under Contract N00019-77-C-0299 for Naval Air Systems Command.
- [13] W.D. Burnside, J.J. Kim, B. Grandchamp, R.G. Rojas, and P. Law, "Airborne Antenna Radiation Pattern Code User's Manual", Report 716199-4, The Ohio State University, Department of Electrical Engineering; prepared under Contract No. NSG-1498 for NASA, September 1985.
- [14] R.G. Rojas, Private Communication, ElectroScience Lab, Ohio State University, July, 1985.
- [15] P.H. Pathak and N.N. Wang, "Ray Analysis of Mutual Coupling Between Antenna on a Convex Surface", Selected Reprints for the Short Course on the Modern Geometrical Theory of Diffraction, The Ohio State University, 1983.
- [16] R.G. Kouyoumjian and P.H. Pathak, "A Uniform Geometrical Theory of Diffraction for an Edge in a Perfectly-Conducting Surface", Proc. IEEE, Vol. 62, November 1974, pp. 1448-1461.
- [17] A.I. Sinsky, J.E. Reed and J. Fee, "Enhanced TCAS II Tracking Accuracy", AIAA/IEEE Digital Avionics Systems Conference Paper 84-2738-CP, 1984.
- [18] A.I. Sinsky and J. Acoraci, "Technical Notes on TCAS II", unpublished correspondence with The Ohio State University, ElectroScience Lab, 1985.
- [19] R.G. Rojas, W.D. Burnside, P. Law and B. Grandchamp, "Simulation of the Enhanced Traffic Alert and Collision Avoidance System(TCAS II)", Report 716199-3, The Ohio State University, Department of Electrical Engineering, September 1985.
- [20] B.J. Grandchamp, "A Study of the TCAS II Collision Avoidance System Mounted on a Boeing 737 Aircraft", Master Thesis, The Ohio State University, Department of Electrical Engineering, 1985.